

**FRAUKE KLINGELHÖFER**

**MODEL CALCULATIONS  
ON THE SPREADING OF  
SUBMARINE LAVA FLOWS**

**54**

**GEOMAR REPORT**

---



**FRAUKE KLINGELHÖFER**

**MODEL CALCULATIONS  
ON THE SPREADING OF  
SUBMARINE LAVA FLOWS**

**GEOMAR**  
Forschungszentrum  
für marine Geowissenschaften  
der Christian-Albrechts-Universität  
zu Kiel

**Kiel 1996**

**GEOMAR REPORT 54**

**GEOMAR**  
Research Center  
for Marine Geosciences  
Christian Albrechts University  
in Kiel

Dissertation  
zur Erlangung des Doktorgrades  
der mathematisch-naturwissenschaftlichen Fakultät  
der Christian-Albrechts-Universität zu Kiel  
Zum Druck genehmigt am 18.12.1995

Redaktion der Serie: Gerhard Haass  
Umschlag: Kerstin Kreis, Harald Gross,  
GEOMAR Technologie GmbH

Managing Editor: Gerhard Haass  
Cover: Kerstin Kreis, Harald Gross,  
GEOMAR Technologie GmbH

GEOMAR REPORT  
ISSN 0936 - 5788

GEOMAR REPORT  
ISSN 0936 - 5788

**GEOMAR**  
Forschungszentrum  
für marine Geowissenschaften  
D-24148 Kiel  
Wischhofstr. 1-3  
Telefon (0431) 600-2555, 600-2505

**GEOMAR**  
Research Center  
for Marine Geosciences  
D-24148 Kiel / Germany  
Wischhofstr. 1-3  
Telephone (49) 431 / 600-2555, 600-2505



---

**1 Table of contents**

<b>1</b>	<b>Table of contents .....</b>	<b>1</b>
<b>2</b>	<b>Zusammenfassung.....</b>	<b>3</b>
<b>3</b>	<b>Abstract.....</b>	<b>5</b>
<b>4</b>	<b>Definition of terms .....</b>	<b>7</b>
<b>5</b>	<b>Introduction .....</b>	<b>9</b>
	5.1 Previous work.....	9
	5.2 Objectives of this study .....	11
<b>6</b>	<b>Submarine volcanism .....</b>	<b>13</b>
	6.1 Sheet flows and pillows .....	15
	6.2 Lava tubes and channels.....	16
	6.3 Lava lakes.....	16
	6.4 Hyaloclastites and pillow breccias .....	17
<b>7</b>	<b>Morphology of pillow lavas .....</b>	<b>18</b>
	7.1 Direct observations .....	18
	7.2 Lava tube growth .....	19
	7.3 Crystallization of a pillow .....	21
	7.4 Cooling of a pillow.....	24
	7.5 Degassing of a pillow .....	25
	7.6 Internal structures of pillow lavas .....	26
<b>8</b>	<b>Rheological properties of basaltic lava .....</b>	<b>28</b>
	8.1 Viscosity.....	28
	8.2 Density.....	35
<b>9</b>	<b>Description of the finite element model .....</b>	<b>37</b>
	9.1 Equations governing fluid flow .....	38
	9.1.1 The equation of continuity .....	39
	9.1.2 The equation of motion.....	40
	9.1.3 The equation of energy .....	42
	9.2 FLOTRAN and PDE/PROTRAN .....	44
	9.3 Model geometry .....	45
	9.4 Flow- and temperature fields from typical boundary conditions.....	46
<b>10</b>	<b>Analytical solution: Tube flow with constant heat flux at a wall .....</b>	<b>48</b>
<b>11</b>	<b>Numerical solutions: Variation of a single parameter.....</b>	<b>53</b>



## Table of contents

---

11.1	Effects of the viscosity on the flow rate .....	53
11.2	Effect of the slope angle on the flow rate.....	56
11.3	The release of latent heat during solidification.....	57
11.4	The effect of viscous heating .....	58
11.5	Influence of the different density functions .....	62
11.6	Cooling of the pillow .....	63
<b>12</b>	<b>Numerical solutions: Complex models .....</b>	<b>69</b>
12.1	The aspect ratio.....	69
12.2	Time dependent model runs .....	73
12.3	Different input pressure functions.....	79
12.4	The influence of the inflow temperature on time-dependent runs.....	81
12.5	The critical pressure .....	82
<b>13</b>	<b>Conclusions and outlook .....</b>	<b>85</b>
<b>14</b>	<b>Acknowledgments .....</b>	<b>88</b>
<b>15</b>	<b>List of commonly used symbols .....</b>	<b>89</b>
<b>16</b>	<b>References .....</b>	<b>92</b>

## 2 Zusammenfassung

Die Morphologie submariner Lavaflüsse wird durch die Eruptionsrate, die Zusammensetzung der Lava und ihrer temperaturabhängigen Viskosität beeinflusst. Um die Dynamik submariner Lavaflüsse zu simulieren, wurden Modellrechnungen mit der Methode der Finiten Elemente durchgeführt. Die simultane Lösung der Erhaltungsgleichungen für Energie, Masse und Moment war dabei Voraussetzung. Die Geometrie von Kissenlaven (Pillows) legte die Anwendung des Modells einer zylindrischen Röhre mit konstanter Länge und konstantem Durchmesser nahe. Die untere Hälfte der Lavaröhre befindet sich in den darunterliegenden Sedimenten oder älteren Lavaströmen, in welche die Wärme konduktiv abgeführt wird. Die obere Hälfte unterliegt konvektiver Seewasser-Kühlung. Eine einfache, temperaturabhängige Newtonische Viskosität und eine temperaturabhängige Dichte wurden für die Modellrechnungen angenommen, wobei die latente Wärme durch Anpassung der spezifischen Wärmekapazität einbezogen wurde.

Erste Läufe zeigten die Bedeutung verschiedener Parameter für die Ergebnisse der Modellrechnungen. Als fundamental stellten sich Fließraten, Kühlung durch das Seewasser und das Freiwerden von latenter Wärme ebenso heraus, wie die Abhängigkeit der Viskosität von der Zusammensetzung, der Temperatur und dem Kristallgehalt der Lava. Diese wurden in ein endgültiges, komplexes Modell übernommen. Dagegen waren Erwärmung durch viskose Reibung, Dichteänderungen mit der Temperatur und Kühlung durch Strahlung nur von geringem Einfluß, so daß sie bei der endgültigen Formulierung des Modells unberücksichtigt bleiben konnten.

Die Randbedingungen für das Entstehen von Kissenlaven wurden durch verschiedene Modellrechnungen mit den Hauptparametern ermittelt. Niedrige Eruptionsraten und niedrige Viskositäten begünstigen die Entstehung von Pillows, während höhere Eruptionsraten zur Entstehung von Schichtlavaströmen führen. Dies entsprach den Erwartungen, da Schichtlavaströme die großen anfallenden Lavamengen effizienter abführen können und darüberhinaus die hohe Viskosität die Lava daran hindert, in engen Röhren zu fließen.

Durch die Variation der Modell-Geometrie, z. B. des Verhältnisses von Breite zu Höhe der Röhre, ergaben sich Aussagen über Energieflüsse und Fließraten und damit über die Entstehung von Zylindern. Zylindrische Schläuche bieten eine maximale Effi-

zienz des Transportes verbunden mit einem minimalen Wärmeverlust im Gegensatz zu mehr elliptischen Modellen. Abweichungen von der zylindrischen Form ergeben sich durch den Einfluß der Schwerkraft und hohe Fließraten an steilen Hängen.

Zusätzlich wurden einige zeitabhängige, komplexe Modellläufe durchgeführt, um das Zusammenspiel der Parameter zu untersuchen. Der Einlaufdruck der Lava wurde in Abhängigkeit von der Zeit verringert, um die langsame Abnahme des Lavanachschubs zu simulieren. In diesen Läufen bildeten sich durch unterschiedliche Abkühlungsgeschwindigkeiten drei verschiedene Zonen aus, die mit den Bereichen unterschiedlicher Kristallmorphologie in realen Pillows korreliert werden könnten.

Als weiteres Ergebnis zeigte sich, daß die Konkurrenz von advektivem Wärmefluß entlang der Zylinderachse einerseits und konduktivem Wärmeabfluß zu den Rändern andererseits die Lebensdauer einer Röhre bestimmen. Übersteigt der Wärmeverlust durch Außenkühlung den Wärmenachschub von innen, endet das Fließen und die Röhre kristallisiert aus. Erst ein kritischer Mindestdruck erhält den Wärmenachschub in das Innere der Röhre aufrecht.

Dieser kritische Druck konnte für verschiedene Rohrlängen und Durchmesser berechnet werden. Unter vergleichbaren Voraussetzungen und damit Druckrandbedingungen werden Lavaröhren also nicht nur ähnliche Durchmesser ausbilden, sondern auch charakteristische Quotienten aus Länge und Durchmesser.

### 3 Abstract

The morphology of submarine lava flows depends on the eruptive rate, composition, and temperature-dependent viscosity of the lava. Finite element model calculations were carried out to constrain the dynamics of submarine lava flows. The conservation equations for energy, mass and momentum are solved simultaneously using numerical methods. A cylindrical tube of fixed length and constant diameter is used as a simple approximation to the pillow geometry. The lower half of the model pillow is embedded into underlying lithic units where heat transport occurs by conduction whereas the upper half is in contact with seawater, where heat transport is by convection. A simple, temperature dependent, Newtonian viscosity and temperature dependent density are used, and latent heat is accounted for by adjusting the specific heat capacity of the lava.

The importance of different parameters was determined in the initial model runs. The flow rate, the cooling through seawater, the release of latent heat of crystallization, the viscosity dependence on the composition, temperature and crystallinity of the lava, and the slope angle were found to be principal parameters for the modeling, while viscous heating, density variations with temperature and pressure and radiative cooling play only a minor role. The former are then included in a more realistic model.

The boundaries of the "pillow" type lava flow regime are constrained through repeated calculations with the main parameters and boundary conditions. Relatively low eruption rates and low viscosities were assumed for the formation of pillowed lava flows. At higher eruption rates predominantly sheet flows will develop, which are more efficient at rapidly transporting large amounts of lava. High viscosity lavas cannot develop a tube-style flow due to the high frictional drag along the margins of the tube flows.

The model geometry was varied, i.e. length of the tube and width to height ratio of the cross-sectional ellipse, and the consequences on the energy and flow rates were examined. The main reason for the formation of cylindrical tubes is the minimal energy loss and the efficiency of transport in a tube in contrast to more elliptical models. Deviations from the cylindrical form are due to gravity and high flow rates on steep slopes.

Some time dependent complex model runs were performed, to study the interaction of different parameters. Entrance pressure was varied with time, simulating a gradual

cut-off of the lava supply. In these calculations three regions with different cooling rates were distinguished, which can be correlated to textures found in pillows.

As a further result, the longevity of the tube flow was found to be constrained by the competition of advective heat flow along the flow axis and the conduction of heat towards the margins of the flow. Once the amount of thermal energy brought into the tube by advection drops below the amount of thermal energy lost by conduction to the ambient seawater, the tube solidifies and flow stops. A critical driving pressure controlling the flow velocities is needed to keep the tube from freezing shut.

This critical pressure was calculated for different tube geometries. For similar environments leading to similar pressure boundary conditions, tube style lava flow will not only exhibit a narrow range of diameters, but also a characteristic length to diameter ratio.

---

## 4 Definition of terms

**Pillow lavas** are elongate interconnected tubes (3-20 m long and 0.3-1 m in diameter) with a roughly elliptical diameter and which are a characteristic form of underwater lava eruptions. They are surrounded by a glassy crust with a variety of primary surface features, including ropy wrinkles, corrugations, spreading cracks and tensional cracks [McPhie et al, 1993]. Pillows erupted in shallow water contain vesicle sheets parallel to the top margin. The inside of the pillow shows a radial pattern of joint fractures, which forms when the lava cools and the volume decreases.

**Megapillows** are up to ca. 6 m high and ca. 10 m wide with irregular, poorly defined outlines. Exceptionally, dimensions of tens of meters (length and width) are found. They can interdigitate with other megapillows or grade into normal pillow facies. They are interpreted as feeder-tubes for the upward growing bulk of normal pillows of a pillow volcano [Schmincke et al, 1987], and therefore show steep inclinations.

**Sheet flows** are tabular lava flows that have a thickness from a few centimeters up to several meters, strongly dependent on the underlying topography. They are divided into 3 structural zones. The lower colonnade of thick regular columns comprises about 1/3 of the flow and contains several pipe vesicle and diffuse vesicle zones at its chilled base. Overlying this is the hackly jointed middle part with arched vesicles at its top. The breccia at the top of the flow consists mainly of black hyaloclastite several tens of centimeters thick [Schmincke and Bednarz, 1990].

**Hyaloclastites** are fragmental deposits consisting of angular glassy shards. They form when glassy crust spalls off of pillows during cooling contraction or rapid growth or as a result of submarine lava fountaining. They are common in the upper facies of a pillow volcano, where the pillow tubes are not as closely packed as in the central parts. Hyaloclastite deposits of pillow volcanoes are mostly a few centimeters thick and are often found in the interstices between pillows. Pillow rinds may be washed together and form graded layers [Schmincke and Bednarz, 1990]. Hyaloclastites formed by explosive eruptions in shallow water are composed of vesicular glassy shards. They can form deposits hundreds of meters thick.

**Pillow breccias** are composed of partly brecciated pillows where two or more jagged pieces still fit together with little or no matrix. They can grade into unfractured pillow units. They are “in situ” breccias that might form for example when the flank of a seamount becomes oversteepened and partially collapses during the growth of a pillow volcano [Fisher and Schmincke, 1984].

**Pillow fragment breccia** consists of lapilli to block-sized, often pie-slice shaped pillow fragments, often with rounded edges. They occur in crudely bedded tabular units of 2-5 m thickness [Staudigel and Schmincke, 1984]. Whole units consist of up to 20 beds and are typically normally graded, some including ash to lapilli sized matrix.

**Pillow volcanoes** may be up to about 100 meters high and several hundreds to thousands of meters long. In the initial growth stage of a pillow volcano, at high eruption rates, megapillows and sheet flows will form quickly, radiating from the vent. During the main phase at nearly constant eruption rates, pillow tubes with smaller diameters will develop. The pillows grade upward from large to small sizes, as the eruption rate gradually decreases. In the last and regressive stage, the volcano produces mainly mini-pillows, isolated sacks and pillow-breccias, because of the steepened slope and decreasing eruption rates [Schmincke and Bednarz, 1990].

**Lava tubes and channels** are 20-50 m wide and can distribute lava over large distances. Tubes can form from roofing-over of lava channels. After the eruption has stopped, the tubes can drain and collapse [Fornari, 1986].

**Pahoehoe lava** flows are subaerial lava flows that are characterized by smooth, lobate surfaces, that may be folded into ropy patterns. They usually comprise many small flow units that have a glassy crust [McPhie et al, 1993]. Pahoehoe lava forms at low flow rates and flowage in tubes, where heat loss is minimal.

## 5 Introduction

Seventy per cent of the earth's surface consists of oceanic crust, the upper 1-2km being primarily composed of submarine lava flows. These display a wide variation in size and morphology, and comprise mainly pillows, sheet flows and minor volcanoclastic rocks. Since direct observation of submarine eruptions is difficult, lava transport mechanisms have to be reconstructed from the geometry and internal structures observed in outcrops and theoretically modeled flow dynamics.

Some of the main problems concerning the formation of pillow lavas are:

- Why do subaqueous lavas display a tubular shape?
- What are the boundary conditions leading to tube flow?
- Which are the primary parameters controlling flow morphology?
- What are the flow rates and cooling times determining the transition from the pillow to the sheet flow regime?

Different geological and geophysical approaches to solve these problems have been undertaken in the past, including morphological studies in outcrops, direct observation of active or inactive submarine lava flows, and experimental and numerical lava flow modeling.

### 5.1 Previous work

The mechanism of formation of pillow lava has been discussed since the first half of the 19th century. Hypotheses regarding the mode of formation include: spheroidal weathering; spheroidal jointing, with subsequent movement of the columns on each other; concretionary processes; explosive eruption (bombs in agglomerate); flow of lava on land or in the water; viscous flow and fracturing of stiff lava; intrusion into unconsolidated sediments; fracturing and partial remelting of lava crusts; and rapid cooling and parting into separate masses by the action of steam [Lewis, 1914; Snyder and Fraser, 1963; Bryan, 1991 and references therein].

Lewis [1914] first proposed pillow lava to be elongated tubular basaltic lava fingers, resembling subaerial pahoehoe lava. This interpretation was largely forgotten until 1975, when scuba divers observed the formation of pillow lava directly [Moore, 1975; Tribble, 1991] and confirmed Lewis' theory.



Inactive submarine volcanoes have been studied by submersibles [Ballard and Moore, 1977; Fornari et al, 1980; Lonsdale and Batiza, 1980; Batiza et al, 1984] and different morphologies of submarine lava flows, such as sheet flows, pillows, lava tubes, lava channels and feeder tubes have been described. Lava flows have been imaged by sidescan sonar [Batiza and Vanko, 1983; Fornari et al, 1985; Fornari and Ryan, 1984; Holcomb, 1988]. These data allow to estimate the dimensions, relative abundance and areal distributions of the different flow types.

A variety of flow types were reproduced in analog experiments with solidifying wax in water [Griffith and Fink, 1992a,b; Griffith and Fink, 1993]. These experiments show that the surface morphology of a flow is mainly controlled by the ratio of the time taken for the surface to solidify and the time scale for lateral flow [Fink and Griffith, 1990]. The resultant morphologies are pillowed flows over a wide range of eruption rates. The advantages of this approach include the ease of observation, easily controlled initial conditions and well-constrained material parameters. A limitation of this method is the difficulty to quantify the observations.

Another technique in physical volcanology is the mathematical modeling of the dynamics of lava flow emplacement. The primary objective of most lava flow models is the determination of the main factors influencing lava flow dimensions and morphology. Different types of physical processes occur, such as degassing, crystallization, solidification, fracturing and other forms of heat, mass, and momentum transfer. The importance of each type of physical process is still uncertain, although many different models of lava flow emplacement have been proposed.

One of the first hypotheses was the dependence of the flow length on the viscosity of the lava [Nichols, 1939]. Walker [1973] postulated a linear relationship between the logarithm of the mean eruption rate and the logarithm of the final flow length. Malin [1980] found that the flow length depends on the cross-sectional flow area and thus on the erupted volume rather than the eruption rate. The scatter on the plots of eruption rate versus flow length was interpreted by Baloga and Pieri [1986] to result from the combined effects that a time-dependent effusion rate and a spatially varying viscosity have on the thickness profile of a lava flow. On the basis of theoretical models for lava flow heat loss, and correlation of the calculations between the eruption rate and the

flow cross-section, Pieri and Baloga [1986] concluded that basaltic lava flows in Hawaii radiate at an effective temperature much lower than the inner parts of the flowing lava.

Other models of subaerial lava flows also suggest that thermal loss is the main factor controlling lava flow dimensions [Danes, 1972]. These models are based on the assumption that a flow is isothermal in each cross-section perpendicular to the direction of flow advance. Crisp and Baloga [1990] presented a mathematical model for the cooling of a lava flow with two separate thermal components: a crust that cools by radiation and thickens with time and an inner core that is isothermal and partially exposed at the top surface. Lava flows have also been modeled as a Bingham liquid with a temperature dependent viscosity and yield stress by Park and Iverson [1984], Dragoni et al [1986] and Pinkerton and Wilson [1994]. The heat is transferred accross the plug through conduction and lost by radiation to the atmosphere at the top of the flow [Dragoni, 1989]. Hulme [1974] performed laboratory experiments on flows of suspensions of kaolin, which show a nearly Bingham behavior.

Borgia and Linneman [1990] proposed that for a given flux of lava, there is a critical channel length beyond which the flow accelerates, through the force of the weight of the crust in the channel onto the flow front, triggering the separation of the flow from its source near the vent. This indicates a volume control on the flow units.

Most studies focused on one particular facet of lava flow dynamics, e.g. lava flow length, Bingham behavior of lava flows or the influence of the eruption rate. Few studies have encompassed several aspects at once, mainly as a result of the growing complexity of the calculations and the increasing demand for calculation time. Although numerous models of subaerial and subterranean magma emplacement exist, relatively few studies have addressed the subject of submarine flows, due to the difficulties involved in observation and the paucity of in-situ data. Thus, flow of lava under submarine conditions is less well constrained.

## 5.2 Objectives of this study

The present study attempts to offer a plausible mathematical description and a quantitative estimate of the dynamics of submarine lava flows while taking into account several governing aspects at once. The finite element method is used to

simultaneously solve the differential equations for momentum, energy and mass conservation with respect to the flow geometry and reasonable boundary conditions.

One of the main goals of this thesis is the determination of the relative importance of the different thermal, mechanical and chemical parameters governing the flow of basaltic lava and the establishment of the boundaries of the tube-style flow field in terms of these parameters. A further objective is to describe the interplay of these parameters in producing a cylindrical geometry. Lastly, the energy and mass flow budgets in lava tubes are quantified in order to establish the longevity of tube flow.

The next two chapters (6) and (7) introduce the geological setting where pillow basalts commonly form and then briefly describe different submarine lava flow morphologies, outlining current ideas on the mechanisms of pillow formation. Field observations form the basis for the modeling. They define the model geometry, the boundary conditions, and the parameters used in the model calculations.

The chapter (8) contains a description of the most important rheological parameters of basaltic lava, and their application to the numerical modeling. A description of the model geometry, the boundary conditions and the finite element programs follow in chapter (9). Thereafter, an analytical solution and the comparison to a simplified numerical model are given in chapter (10) to estimate the calculation error.

The results of the variation of single parameters to evaluate the importance of the different parameters are described in the chapter (11). The formation of the diverse structures can be constrained through variation of the different parameters and an exhaustive parameter search is a prerequisite for detailed model calculations. The fundamental parameters are included in some more realistic time dependent runs in chapter (12). These help constrain the height to width and diameter to length ratios for typical input pressures and geochemical compositions. A comparison to characteristic aspect ratios and textures of pillows observed in outcrop is made and allows conclusions to be drawn regarding their history of formation. Chapter (13) summarizes the results and conclusions.

## 6 Submarine volcanism

Field studies of ophiolites, oceanic crust which has been obducted onto a continent [Coleman, 1977; deWit and Stern, 1978; Schmincke and Bednarz, 1990; Nicolas, 1995], provide information about the structure of the oceanic crust, which consists of three layers (Figure 1).

Based on studies of the Troodos Ophiolite, Cyprus, three end-member types of submarine volcanic units have been proposed by Schmincke and Rautenschlein [1987] and Schmincke et al [1983]: pillow volcanoes, sheet flow volcanoes and breccia flow volcanoes. Individual pillow volcanoes along the Juan de Fuca Ridge, the Mid-Atlantic Ridge and in the Troodos Ophiolite display similar distinctive morphologies [Schmincke and Bednarz, 1990], with a height of about 100 m and a length of at least 800 m, indicating that the eruptive histories of these volcanoes are similar. The height of

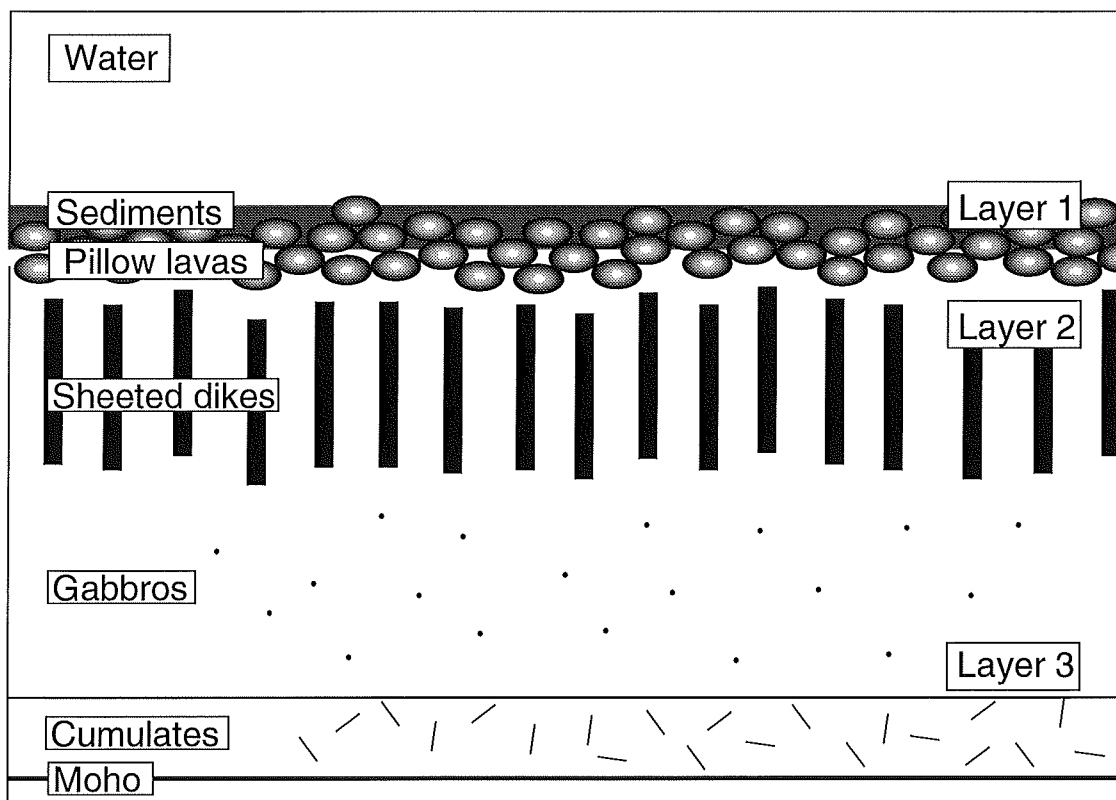


**Fig. 1** Schematic diagram of the structure of the oceanic crust. The oceanic sediments form layer 1. Layer 2 consists of extruded basaltic lavas (mainly pillow lavas, sheet flows), and the sheeted dike complex. Layer 3 is mainly made up of gabbros.

individual seamounts can be related to the depth and size of the magma bodies at Mid Ocean Ridges (MORs) [Smith and Cann, 1992].

The initial growth stage of a pillow volcano begins with high eruption rates leading to the formation of megapillows, and sheet flows radiating from the vent. During the main stage at nearly constant eruption rates pillows show an upward gradation from large to small sizes, as the eruption rate slowly decreases [Dimroth et al, 1978; Schmincke and Bednarz, 1990]. In the last and regressive stage, the volcano produces mainly mini-pillows, isolated sacks and pillow-breccias, because of the steepened slope and decreasing eruption rates [Schmincke and Bednarz, 1990]. Figure 2 shows a schematic model of a pillow volcano from the upper part of the extrusive sequence of the Troodos Ophiolite, Cyprus [Bednarz, 1988]. The following subchapters (6.1) to (6.4) describe the spectrum of products of submarine volcanism.

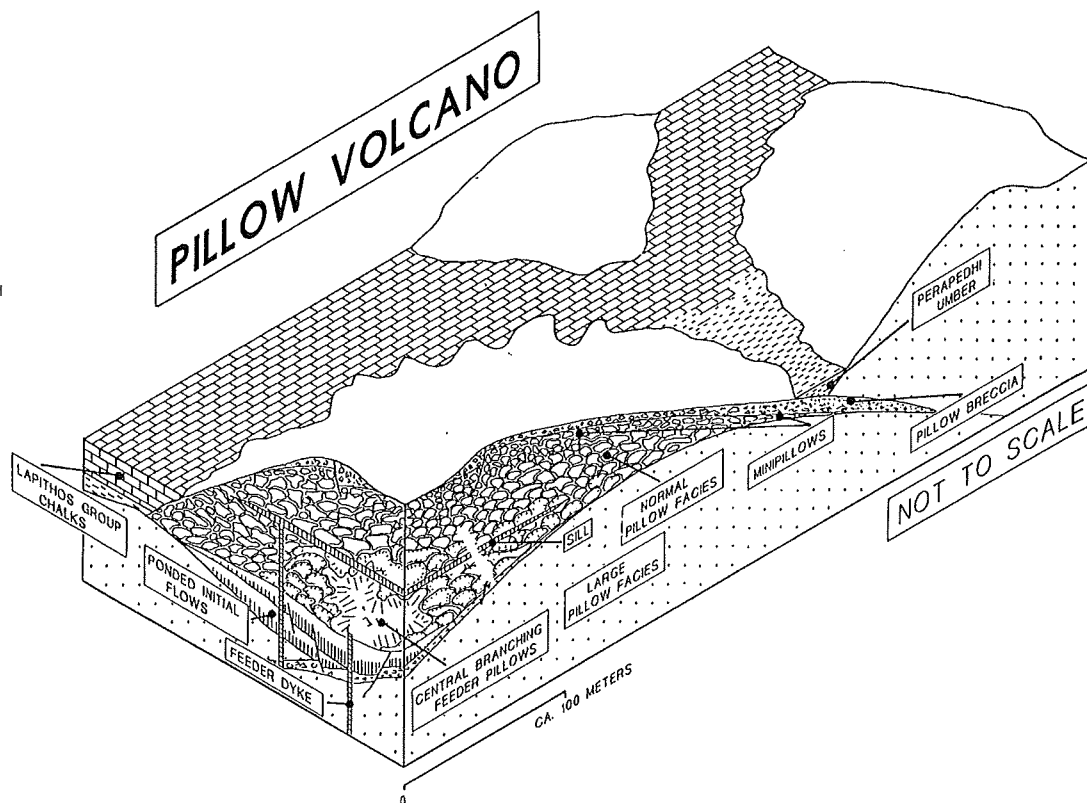


**Fig. 2** Schematic model of a pillow volcano from the upper part of the extrusive sequence of the Troodos ophiolite, Cyprus [Bednarz, 1988].

## 6.1 Sheet flows and pillows

Studies on the Galapagos Rift at 86°W with the deep submersible Alvin have shown that pillows and sheet flows are two dominant features of oceanic volcanism on MORs [Ballard et al, 1979]. Sheet flows represent the subaqueous equivalent of surface fed pahoehoe flows, while pillow lavas are analogous to tube fed pahoehoe [Ballard et al, 1979; Jones, 1968].

Megapillows, up to 3 meters high and several meters wide, occur in the central lower or core facies of pillow volcanoes [Schmincke and Bednarz, 1990]. They interdigitate with other megapillows or grade into normal pillow facies. They serve as feeder-tubes for the upward growing bulk of normal pillows.

Pillow tubes can often form on the front of a broad lava flow and grade into it, and the main sheet flow may overrun the pillow basalt at a later stage [Baragar, 1984] (Figure 3). The resulting morphology depends on the degree of channellization and flow rates, which are in turn a function of the eruption duration and rate. Apparently, pillows dominate on slow spreading ridges, while sheet flows and pillows are more common on fast spreading ridges [Baragar, 1984].

The same sequence of lava flows, megapillows and pillows is found in Archean and Paleozoic lava flows [Dimroth et al, 1978; Hargreaves and Ayres, 1979; Cousineau and Dimroth, 1982; Schmincke and Sunkel, 1987; Schmincke, 1988], suggesting broadly

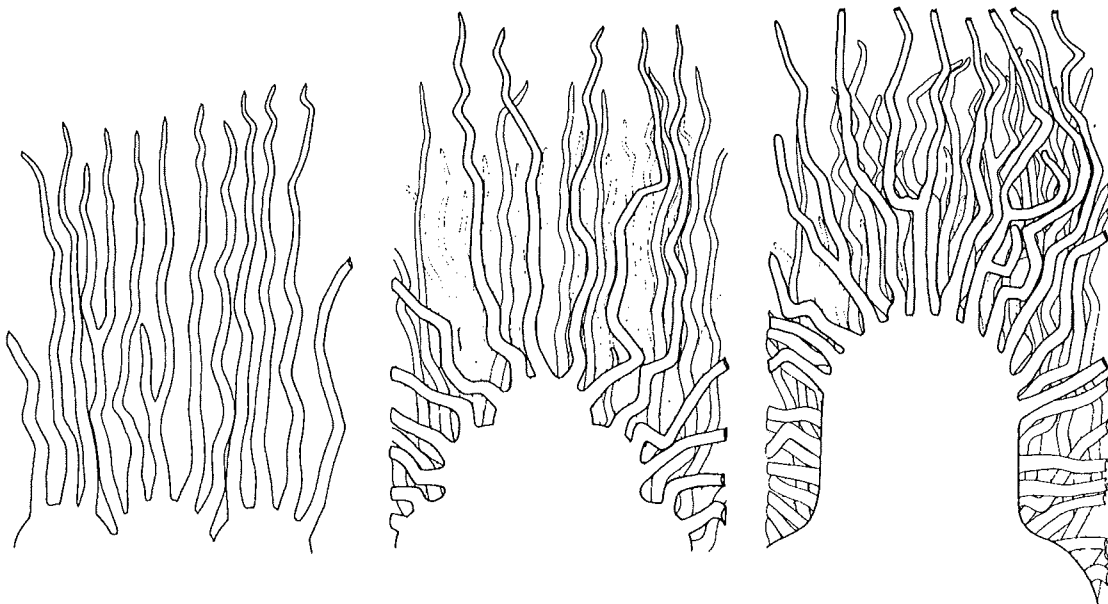


**Fig. 3** Development of lava tubes at the front of a sheet lava flow, which overruns the pillows at a later stage [Baragar, 1984]

similar eruptive histories. The Archean lava sequences seem to have a greater proportion of massive flows while the modern flows contain more pillowed flows, probably due to higher eruption rates in the Archean [Wells et al, 1979].

## 6.2 Lava tubes and channels

20-50 m wide and several 400-800 m long lava tubes and channels were recognized in sonar surveys of the East Pacific Rise, where they form a system for the distribution of the lava [Fornari, 1986]. Eruption rate and volume are probably the most important controlling factors in determining if tubes and channels can form, since the composition of the lava does not change significantly during one eruption [Fornari, 1986]. Lava tubes are more abundant on fast spreading MOR environments, where eruption rates are high. The tubes can develop from roofing over of the lava channels. After collapse portions of them may fill with water or volcanoclastics. After the flow has stopped advancing, inflation of lava tubes can occur by the injection of new lava under the crust of the tube, causing the cooled exterior crust to deform as a brittle solid [Appelgate and Embley, 1991].

## 6.3 Lava lakes

A pause in the eruption, during which the pillows solidify, can lead to the formation of a dam, behind which lava can accumulate as a lava lake (tens of meters to a hundred meters across) and eventually spill over as a sheet flow.

In a lava lake, large lava coils (1-4 m diameter) which probably mark shear zones at the edges of streams of mobile lava have been mapped during a deep tow survey at the Galapagos rift [Lonsdale, 1977].

After draining of a lava flow or lake, collapse can occur, leaving large pits with only some pillars standing near the side walls of the pit. Ballard et al [1979] proposed that the pillars might represent undrained parts of the flow or might be analogous to subaerial spiracles. They form, even under high pressure, when water which is trapped beneath a lava flow rises and quenches a columnar region in the flow. After drainage a solid pillar is left [Waters, 1960].

## 6.4 Hyaloclastites and pillow breccias

Pillow breccias are composed of partly brecciated pillows, whereby two or more sharp edged pieces can still be fitted together. There is no fine grained matrix between the pieces. Often pillow breccias grade into normal pillowed units [Staudigel and Schmincke, 1984]. These breccias can develop when the flanks of a pillow volcano oversteepen, become unstable and partially collapse [Fisher and Schmincke, 1984].

Pillow fragment breccia contains lapilli to block sized, often pie-slice-shaped pillow fragments, sometimes in ash to fine lapilli-sized matrix. Two locations of formation are proposed by Fisher and Schmincke [1984]: on steep slopes of pillow volcanoes and as talus breccia accumulated at the foot of submarine fault scarps.

Isolated pillow breccias commonly occur at the top of a pillow sequence and consist of irregular pillows, lava stingers, isolated mini pillows, lava droplets and broken pillow fragments in a tuffaceous matrix. Because of the teardrop shape of the isolated pillows and droplets, leakage from larger pillows and lava fountaining were proposed as formation mechanisms [Moore, 1975; Schmincke et al, 1983].

Hyaloclastites are breccias of spalled-off, angular, glassy rinds of pillows. They are irregular in thickness, for example in pillow interstices [Schmincke and Bednarz, 1990]. Spalling occurs primarily due to cooling contraction or expansion of growing pillow lavas [Fisher and Schmincke, 1984]. The rinds break off along their vesicular inner portion, allowing the formation of another interior quenched margin [Staudigel and Schmincke, 1984]. Staudigel and Schmincke [1984] describe two distinct types of hyaloclastites : (a) ash-sized hyaloclastites, mainly made of non-vesicular to poorly vesicular shards in the interstices of pillows, or in beds up to 5 m thick. (b) 2-6 m thick beds containing lapilli-sized vesicular shards, often including pillow fragment blocks. Smith and Batiza [1989] proposed that a rapid eruption rate leading to lava fountaining is the dominant control on hyaloclastite formation. The shards and water build a high density slurry, which is transported away from the vent and deposited like a turbidite, forming sheets of hyaloclastites that thin outwards. Also, thermal shock granulation might be responsible for the formation of hyaloclastites in water depths above the critical pressure, where magmatic explosivity is restricted [McBirney, 1963; Lonsdale and Batiza, 1980; Kokelaar, 1986]. Interface instabilities between the water and the lava might lead to superheated water resulting in vapor explosions [Wohletz, 1986].



## 7 Morphology of pillow lavas

Pillow lava develops when lava flows into water. This type of flow characteristically builds elongated tubes (3-20 m long and 0.3-1 m diameter) (Figure 4), with a glassy outer crust. Inside the tube, hot lava can continue to flow, insulated from the seawater. Subchapter (7.1) and (7.2) describe in-situ observations of pillow growth and structures associated with crust formation and rupture, respectively. Petrological and textural aspects of pillow crystallization are given in subchapter (7.3). Structures caused by cooling, degassing, and gradual drainage of lava tubes are presented in the last three subchapters. These observations provide information on geometry, rates of growth and cooling to be used as constraints for the initial boundary conditions and comparison to model calculations.

### 7.1 Direct observations

Divers have observed the flow of basaltic lava into the sea in 1969-1973 at Kilauea, Hawaii [Moore et al, 1973; Moore, 1975] and found that the subaerial pahoehoe flow upon entry into the water developed cylindrical flow lobes about 1 m in diameter

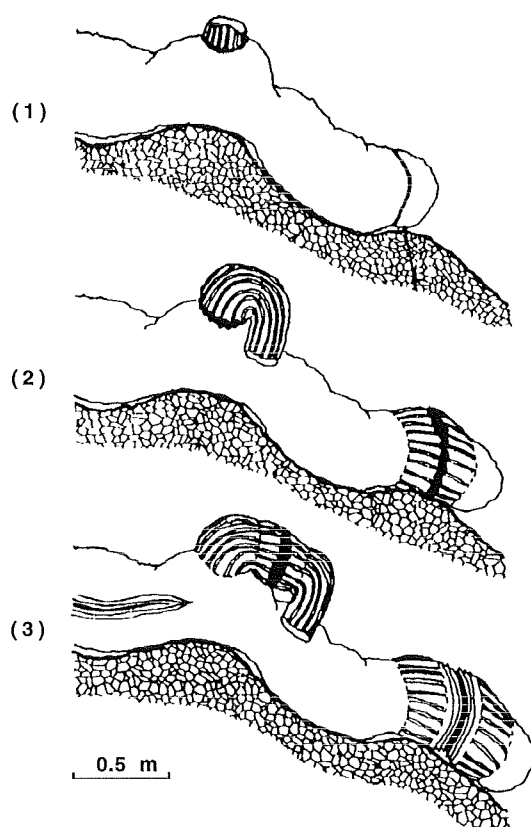


**Fig. 4** Growth of a lava tube through cracking and budding [Moore, 1975]. The tube grows through fracturing of the brittle crust. The front of the pillow lengthens at a ring-shaped crack and the tube diameter locally increases through tube-parallel cracks. A new bud can grow vertically at first and later bend down due to gravity.

(Figure 4). The flow built a lava delta with a subaerial pahoehoe cap and a flow foot breccia, a submarine sequence of steeply dipping, foreset bedded glassy volcanic sand and talus, including conformably dipping cylindrical lava tongues (Figure 5) [Moore et al, 1973; Jones and Nelson, 1970; Peterson, 1976; Schmincke and Staudigel, 1976]. Some of the tongues were broken and proved to be hollow pipes with 2-5 cm thick walls. The inner layer of glass formed when the tube drained and water replaced the lava. Tube growth never occurred through stretching of the crust, but rather through fracturing. Glowing hot lava was visible at cracks where growth took place at spreading rates on the order of  $0.05\text{--}20\text{ cm s}^{-1}$ . These cracks remained active up to several minutes and showed a variety of geometries [Moore and Lockwood, 1978]. Sometimes the tubes imploded, spalling off fragments of solidified glassy crust. These implosions occurred in intervals of 5 s and were probably due to contraction of cooling gases inside the tube. The concussions were painful to the divers' ears within about 3 m [Moore, 1975].

## 7.2 Lava tube growth

Figure 4 shows the growth of a lava tube through cracking and budding [Moore, 1975]. Tube diameter increases by lava addition along tube parallel cracks, whereas ring-shaped cracks lengthen the tubes. The rate of lava transport can increase when additional tubes are formed through bifurcation of active tubes. It is likely that the pressure required to maintain flow in a lengthening tube will eventually exceed the wall strength nearer to the source [Mills, 1984]. Due to the higher pressure inside the tube, new buds can grow vertically (i.e. "trap door" growth) and after further development bend over downwards. In the bends, new cracks and bifurcations often develop [Moore, 1975].

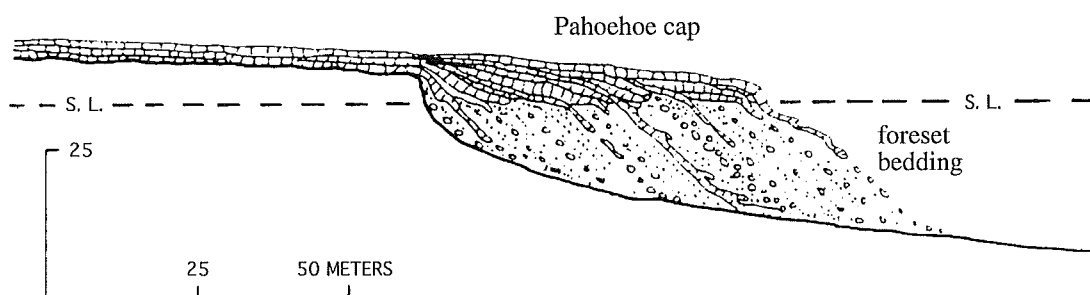


**Fig. 5** Cross section of an advancing lava delta showing the pahoehoe cap that covers the mainly fragmented, poorly sorted, submarine foreset beds [Moore et al, 1973]

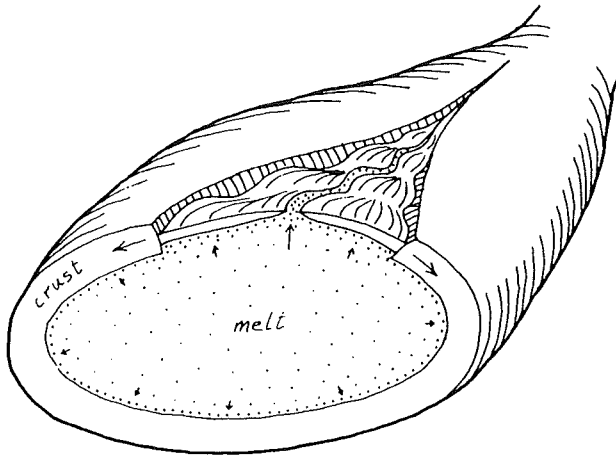


**Fig. 6** Sectioned pillow lobe which has expanded through magma injection producing a spreading crack and new crust. Corrugations and troughs develop at right angles to the crack. The thickness of the crust is exaggerated [Moore and Lockwood, 1978].

When a crack opens, lava solidifies, attaches itself on the trailing edges of the spreading crust and produces some characteristic features on the new crust: scarps, filamented texture and corrugations. Scarps develop parallel to the spreading crack and mark the outer limits of the old crust. Their height ( $\approx 1\text{cm}$ ) is a measure of the age of the crust before cracking, normally less than a few minutes. Smaller scarps develop within the new crust where the old crust is brittle enough, suggesting a slow spreading rate. Filamented texture forms on the solid crust adjacent to the spreading axis, from gently outward dipping fine glass fibers and vesicles elongated perpendicular to the crack [Moore and Lockwood, 1978]. Corrugations, small ridges and troughs on the new crust perpendicular to the spreading crack probably result from secondary convective rolls in the melt, which generate a viscous drag on the outward moving plates of new crust. Figure 6 shows corrugation ridges and troughs developed on a new spreading crack after inflation of the pillow. A picture of the bread-crust like outside of a pillow is shown in Figure 7. Single sack-like pillows are rare. They develop when large individual lava fragments detach during phases of rapid growth and tumble down a steep slope [Moore, 1973; Walker, 1992].

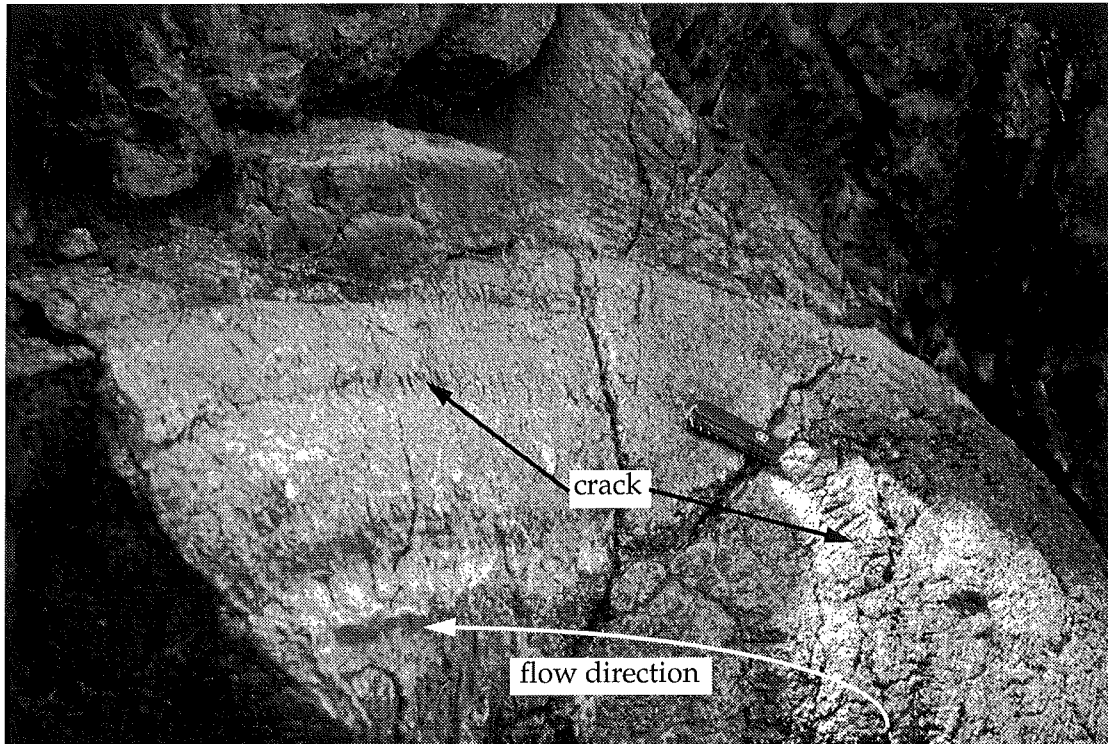


**Fig. 7** Bread-crust like outside of a pillow in Muriwai, New Zealand, with corrugation ridges and troughs. Swiss army knife for scale.

### 7.3 Crystallization of a pillow

Most pillows form by extrusion of mid-ocean ridge basalt (MORB). Although early studies of the geochemical composition of MORBs emphasised their uniformity, since the 1970's significant geochemical variations have been found which appear to correlate with topographic and structural features that characterize particular ridge segments [Wilson, 1989]. MORBs have been classified as normal (N-type, depleted), plume (P-type, enriched) and transitional (T-type). N-type basalts are recovered mostly from the Pacific and from the Atlantic south of 30°N, whereas P-type basalts are found mostly in the Atlantic north of 30°N [Wilson, 1989]. Viereck et al [1989] proposed different degrees of melting of a compositionally homogeneous source as mechanism for the formation of different compositions of N-MORBs (Table 1 shows a typical composition of N1 and N2-MORB).

When the temperature in a silicate melt drops below the liquidus, crystals do not form immediately. A significant degree of undercooling is necessary before crystallization begins [Philpotts, 1990; Kirkpatrick, 1976]. First, minute crystals of the new phase, nuclei, start to appear. Once they reach a critical radius a stable nucleus is formed that can continue growing. With increasing degree of undercooling the nucleation rate first increases but then decreases when the melt cools to a glass. The final crystal size is determined by the concentration of nutrients in the surrounding melt and the proximity of other crystals [Philpotts, 1990; Marsh, 1981].

Therefore, the size and concentration of microlites inside a pillow provide information about its cooling history. Pillow rind textures typically reflect cooling from near liquidus temperatures of ca. 1470 K down to the ambient water temperature. The cooling rate decreases from the border to the core. Therefore, the number of nuclei in a pillow will increase towards the margin until a maximum is reached and then decrease again as higher degrees of supercooling make it more difficult for nuclei to form and the melt cools to a glass [Philpotts, 1990].

Pillows normally consist of three different zones: crust, border and core (see Figure 8) [Dimroth et al, 1978; Bryan, 1972]. The crust, 1-2 centimeters thick and formed at the highest degrees of undercooling, consists of glass and commonly some phenocrysts such as olivine, plagioclase or orthopyroxene. The border zone (2-10 cm thick) is made up of three sub-zones: (a) a spherulitic border zone. (b) a zone containing numerous closely spaced quench microlites of plagioclase bearing a crust of albite spherulites. The size of the microlites and thickness of the spherulite fibers increases across the zone. (c) a transition zone into the microlitic core. At the margin of the core, quench plagioclase bears an overgrowth of albite dendrites [Dimroth et al, 1978; Natland, 1978].

Bryan [1972] suggested that crystal growth in the quenched glass of zone 1 and the border of zone 2 occurs under supercooled conditions in which the viscosity of the melt significantly reduces diffusion rates of the nutrients. Then the most efficient crystal growth occurs by maximising the surface to volume ratio, leading to skeletal, dendritic and spherulitic growth forms.

The core itself is microcrystalline. Olivine crystals in the core show a typical lantern-like form with a low surface to volume ratio, which probably forms, when the temperature is maintained just below the liquidus for relatively long periods [Philpotts, 1990]. Growth is then centered about relatively few, widely spaced nuclei and proceeds at nearly the same rate on all crystal faces.

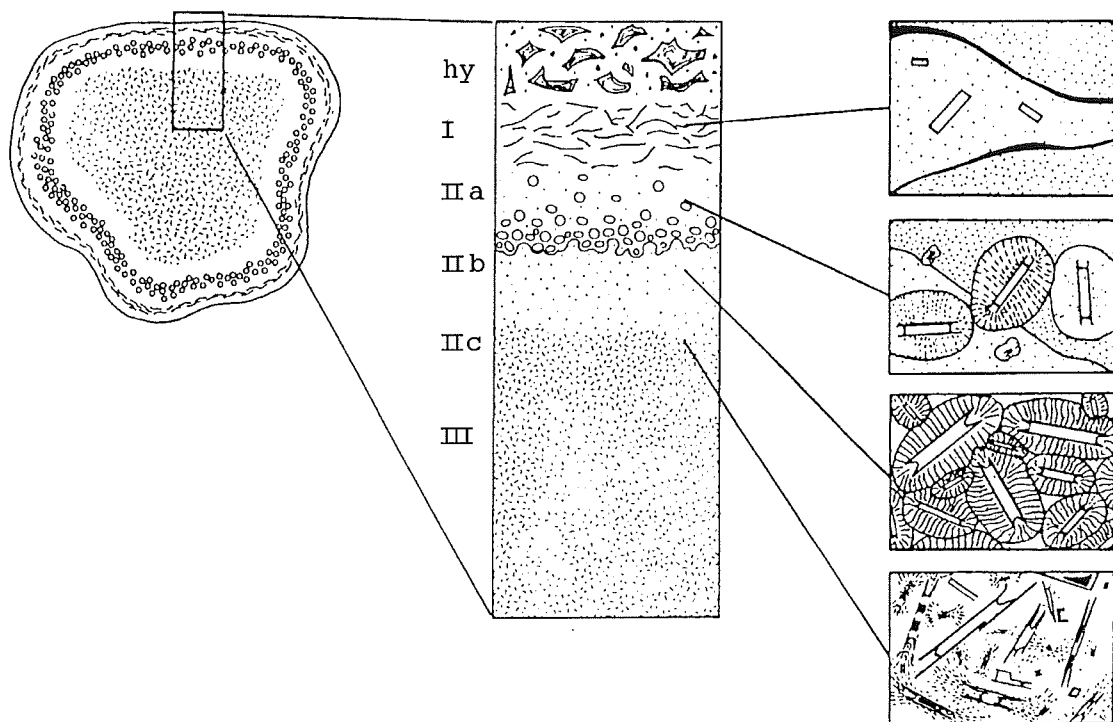


**Fig. 8** Structure and microstructure of a pillow. hy = hyaloclastite, Zone I: Glassy crust. Thermal strain during quenching produced subconcentric cooling cracks. Microphenocrysts of plagioclase may be present, quench microlites are absent. Zone II: Spherulitic border zone. Zone IIa: Quench microlites of plagioclase widely spaced. Plagioclase microphenocrysts have overgrowth of quench morphology, albite spherulites form overgrowth on microlites and microphenocrysts. Spherulites grew across thermal contraction cracks. Zone IIb: Closely spaced quench microlites of plagioclase, overgrown by albite spherulites. Size of quench microlites and thickness of spherulite fibres increases toward Zone IIc: Transition to core. Relatively large quench microlites of plagioclase bear dendritic overgrowth of albite. Zone III: microlitic core zone of the pillow [after Dimroth and Lichtblau, 1979].

#### 7.4 Cooling of a pillow

Theoretically, only a hairline of incandescent material should be visible at spreading cracks of a pillow, due to the rapid cooling through the seawater. Divers typically observe up to 20 cm of glowing lava at growing pillow lavas. The reason for this discrepancy could be insulation of the incandescent material through an insulating sheath of water vapor. The formation of this sheath can be explained by considering the lifetime of a water droplet on a hot stove (Figure 31) [Mills, 1984]. Incandescent lava extruding into the water is insulated by a sheath of vapor. Once the surface temperature drops below the Leidenfrost temperature, the lava is cooled by direct contact with the water. Only fresh cracks can expose incandescent lava.

The inside of a pillow shows a radial pattern of joint fractures, which forms when the lava cools and the volume decreases [Jaeger, 1968]. The pattern is more pronounced in the less vesicular lower half of the pillow, suggesting that cooling progresses more rapidly in the upper, water cooled, hemisphere than in the lower hemisphere, which is still in contact with the underlying lithic units. The contraction cracks are usually represented by radial joints in transverse sections [see Figure 9] and columnar joints in longitudinal sections [Yamagishi et al, 1989]. Conformable joints often divide the pillow into marginal, outer core and central zones, or a horizontal joint may divide it into upper and lower hemispheres [Yamagishi, 1987].

### 7.5 Degassing of a pillow

Vesicularity and vesicle size of pillow lava decrease with water depth because of the increasing pressure of the water column. Therefore, it is possible to estimate the depth of formation even after crystallisation and later uplift, through examination of the vesicle size [Jones, 1969; Moore and Schilling, 1973; Duffield, 1978]. Another important factor controlling the vesicularity of pillows is the amount and composition of volatiles present in the melt at the time of eruption [Dudas, 1983]. In shallow water, pillows commonly contain pipe-vesicles and one or two concentric zones rich in subspherical vesicles, which show a preference for the upper half of the pillow [Wells et al, 1979; Walker, 1987]. The pipe vesicles were trapped when crystallization advanced toward the core during solidification of the fluid lava, often connecting smaller vesicles [Yamagishi et al, 1989; Wilmoth and Walker, 1993]. Transport of lava in a tube may result in a decrease in vesicularity due to bubble rise and loss of larger bubbles [Cashman et al, 1994]. Some of the structures described above like joints and vesicles are shown in Figure 9; a cross-section of a pillow-lobe from an outcrop in Muriwai, New Zealand.

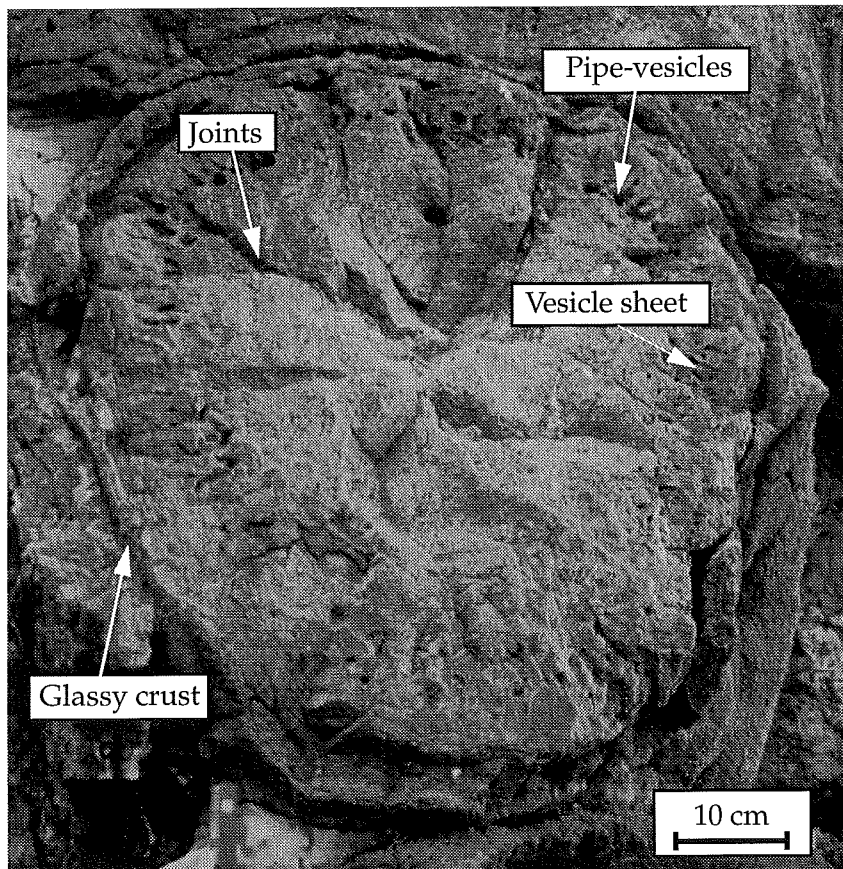
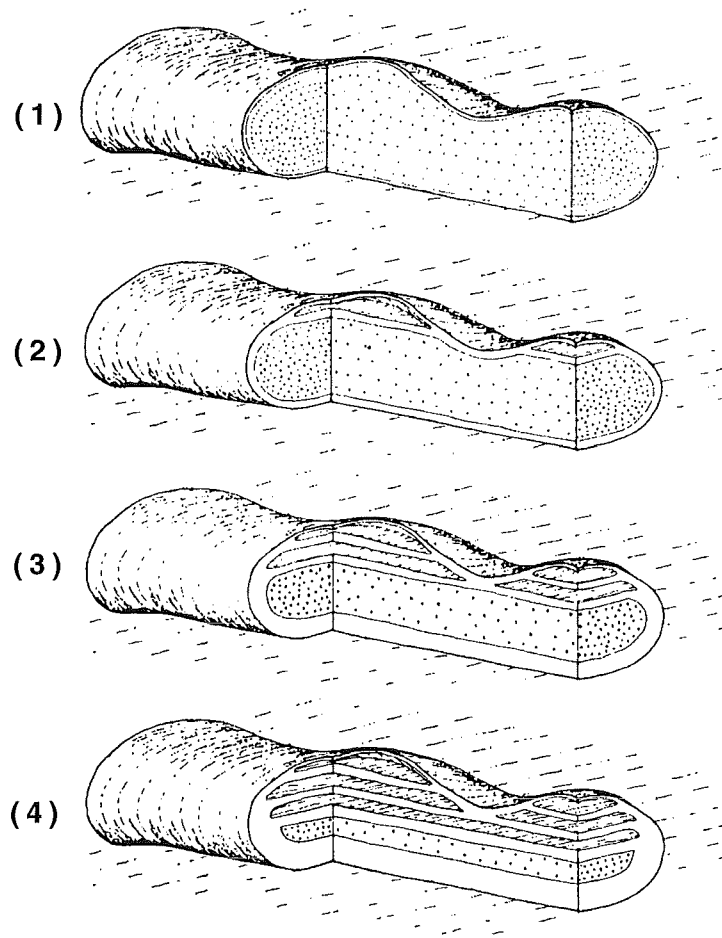


Fig. 9 Cross-section of a lavatube in Muriwai, New Zealand. Elongated pipe-vesicles are pointing towards the outer rim. The outer glassy crust formed through quenching by the seawater. Radial joints develop, when the tube solidifies and the volume decreases.



## 7.6 Internal structures of pillow lavas

Moore and Charlton [1984] found 1-5 cm thick lava layers resembling individual lava flows inside lava tubes at San Obispo Bay, California (Figure 10). These layers seem to form when the lava surface in a tube falls to a lower level as the lava supply ceases and water enters the tube through cracks, chilling a new crust on top of the lava stream [Yamagishi, 1985] as observed in subaerial lava tubes [Peterson and Swanson, 1974]. Through repeated drainage, a series of lava layers can develop, before the lava tube



**Fig. 10** Formation of lava layers within a pillow pipe. Liquid lava is shown by a dotted pattern and surrounded by thin quenched crust.

- 1) Irregular pillow pipe filled with molten lava.
- 2) Lava level has lowered and water enters high parts of the pipe, chilling the top of the lava.
- 3) Second drop of the lava level leads to the formation of the second shelf, while the first remains in place.
- 4) Repetition of process shown in 3 has been reported to lead to up to 18 shelves. Several interconnected lobes may undergo the same history of lava level and therefore display similar shelf assemblages [Moore and Charlton, 1984].

collapses through the weight of subsequent overlying lava flows. The lava layers may show pahoehoe-type wrinkles, which can develop only at greater depth, where the boiling point of water is higher, the cooling through the water is slower and thus the material can be deformed for a longer time. No quenching occurs and the crust can be dragged and folded by the underlying current of molten lava.

In shallow water, pillows with concentric sets of repeating rinds are commonly found. They do not cover the pillow completely and are always accompanied by a rupture in the outer crust. These layers might form when rinds of pillows break off, allowing the formation of a second quenched margin. Often, the spalled-off rinds are separated from the pillow, but sometimes they form up to 5 nearly concentric layers around one pillow [Staudigel and Schmincke, 1984].

Kawachi and Pringle [1988] proposed that these evolve through the implosion of the lava tubes due to the cooling of the vapor inside. The diameter of the pillow decreases and pieces of the newly formed crust are thrust beneath the adjacent crust ( Figure 11).

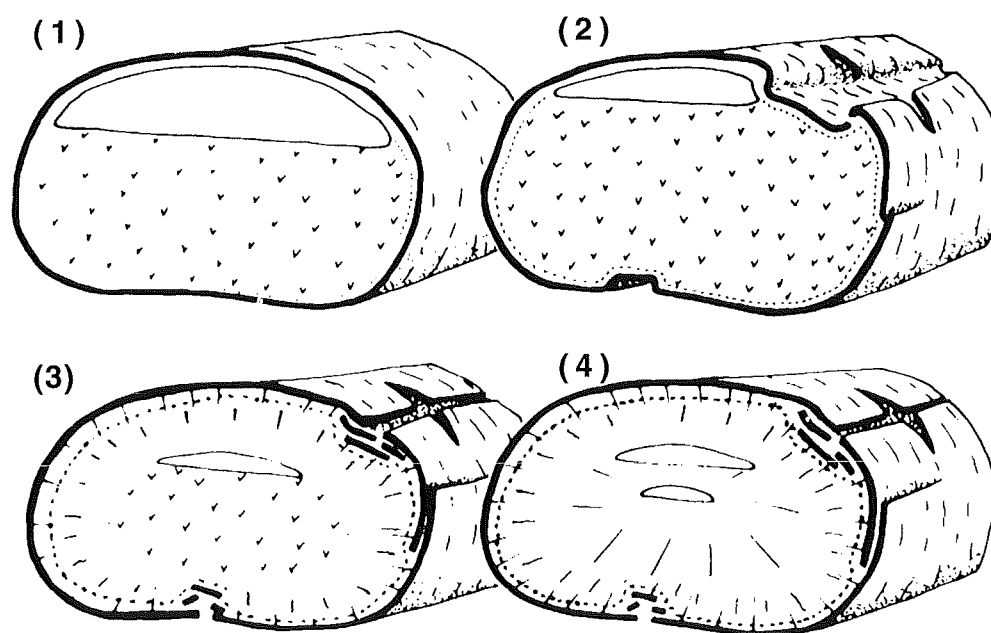


**Fig. 11** Development of multiple-rind structures in a pillow. After formation of the skin, the exsolved gases accumulate at the top of the tube. As the water vapor condenses, implosions cause thrusting of the rind. Inward buckling rind breaks at the weakest points [Kawachi and Pringle, 1988].

## 8 Rheological properties of basaltic lava

Accurate modeling of volcanic or magmatic processes requires data on the rheological properties of magma. Among the most important rheological parameters of lava is the viscosity. In subchapter (8.1) the viscosities for different basaltic compositions are determined for temperatures between the solidus and the liquidus. The relative viscosity resulting from several functions to compensate for the phenocryst content are compared. The effect of different crystal sizes, the vesicle abundance and the H<sub>2</sub>O content on the viscosity are calculated and discussed. The variations of the density with temperature and composition are treated in subchapter (8.2).

### 8.1 Viscosity

Non-vesicular basaltic melts behave like Newtonian fluids at temperatures above their liquidus [Shaw, 1972; Murase and McBirney, 1973; Pinkerton and Stevenson, 1992]. Their viscosities depend on the composition, including volatile concentration and on the temperature of the lava and exhibit a linear relation between stress and spatial variation of the velocity [Dingwell et al, 1993]. The viscosity of lava also depends on the volume percentage of phenocrysts and vesicles. At small fractions (<40%) of suspended material, lavas display Newtonian behavior with an increased viscosity [Kerr and Lister, 1991; Bottinga, 1994]. When the suspended phenocrysts exceed a fraction of ca. 40 vol% [Lejeune and Richet, 1995], lava displays a temperature-dependent yield strength below the liquidus, so that Bingham or pseudoplastic behavior can be assumed [Shaw et al, 1968; Hulme, 1974; Pinkerton and Sparks, 1978; Ryerson et al, 1988]. Then the clustered phenocrysts begin to form an interconnecting network across the suspension and resist shear deformation.

The viscosity of silicate melts displays an Arrhenius type inverse logarithmic variation with temperature  $T$  according to a relation of the form [McBirney and Murase, 1984]

$$\eta = A_{\eta} \exp(E_{\eta}/R_G T) \quad (1)$$

where  $\eta$  = Viscosity of the lava [Pa s],

$A_{\eta}$  = Empirical constant for lava viscosity [Pa],

$E_{\eta}$  = Activation energy of the viscous flow [J mol<sup>-1</sup>],

$R_G$  = Gas constant = 8.31 [J mol<sup>-1</sup> K<sup>-1</sup>].

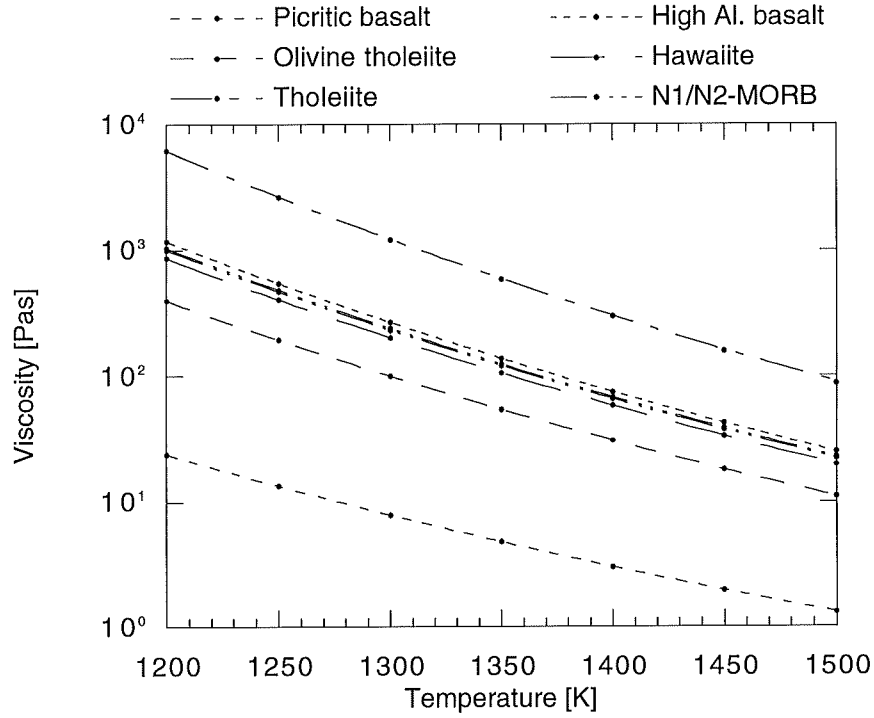


**Fig. 12** Temperature dependence of the viscosity of different basaltic lava-types calculated after the method of Bottinga and Weill [1972], for compositions listed in Table 1. Data points are from model calculations and lines interpolations. Similar notation is used in subsequent diagrams.

The compositional dependence of viscosity in silicate liquids is approximated by a linear equation of the form [Bottinga and Weill, 1972]

$$\ln \eta = \sum_i X_i D_i \quad (2)$$

with  $X_i$  = Mole fraction of oxide component  $i$ ,

$D_i$  = Empirical constant associated with component  $i$ .

Figure 12 shows the viscosity of lavas calculated after the method of Bottinga and Weill [1972] for different basaltic compositions [McBirney, 1994; Viereck et al, 1989] as listed in Table 1. The solidus and liquidus temperatures also noted in Table 1 are calculated using the program MELTS [Ghiorso, 1985] from the given compositions. MELTS calculates the volume percent of crystals as a function of temperature for practically all relevant phases. From these data, viscosities and densities for the modeling have been calculated, and curves fit to these data are included in the model.

Extruded lavas generally have temperatures below their liquidus. Advancing crystallization increases the viscosity. This increase is influenced by the shape and size

of the crystals and by the change in composition of the remaining liquid. Einstein showed that for small concentrations of spheres the viscosity is given by [Einstein, 1906; Einstein, 1911]

$$\eta = \eta_0 (1 + 2.5\phi) \quad (3)$$

where  $\eta_0$  = Viscosity of the crystal free liquid [Pa s],

$\phi$  = Volume fraction of crystals.

By integrating this relationship over a distribution of all sizes of particles, Roscoe [1952] found the following formula, called the Roscoe-Einstein equation

$$\eta = \eta_0 (1 - R\phi)^{-2.5} \quad (4)$$

R is a constant based on the volumetric ratio of solids at closest packing. It is usually taken as 1.0 for crystals with serial sizes, 1.35 for spheres of uniform size. Marsh [1981] found a value of 1.67 more appropriate for crystals in lavas.

There are large differences between the measured viscosities of crystal-rich lava and the theoretical values of the Einstein-Roscoe equation for serial and uniform sizes [McBirney and Murase, 1984]. The size and shape of crystals plays an important role, since the closest packing depends strongly on this factor [Kerr and Lister, 1991].

**TABLE 1.** Typical chemical compositions of some basaltic rocks [wt. %] and solidus and liquidus temperatures in [K] [McBirney, 1994; Viereck et al, 1989]

Type of rock	Picritic basalt	Olivine tholeiite	Tholeiite	High alumina basalt	Hawaiite	N1-MORB	N2-MORB
SiO <sub>2</sub>	46.4	49.2	53.8	49.2	47.9	50.3	50.4
TiO <sub>2</sub>	2.0	2.3	2.0	1.5	3.4	1.1	1.50
Al <sub>2</sub> O <sub>3</sub>	8.5	13.3	13.9	17.7	15.9	15.8	14.9
Fe <sub>2</sub> O <sub>3</sub>	2.5	1.3	2.6	2.8	4.9		
FeO	9.8	9.7	9.3	7.2	7.6	9.4	10.4
MgO	20.8	10.4	4.1	6.9	4.8	7.84	7.46
CaO	7.4	10.9	7.9	9.9	8.0	12.5	11.5
Na <sub>2</sub> O	1.6	2.2	3.0	2.9	4.2	2.13	2.43
K <sub>2</sub> O	0.3	0.5	1.5	0.7	1.5	0.24	0.20
P <sub>2</sub> O <sub>5</sub>	0.2	0.2	0.4	0.3	0.7	0.09	0.14
Solidus	1744	1581	1420	1491	1445	1487	1470
Liquidus	1439	1406	1320	1416	1390	1442	1425

Sherman [1968] found that the relative viscosity of emulsions depends on the mean diameter of the oil drops according to the relation

$$\ln(\eta_R) = \ln(\eta/\eta_0) = \frac{\beta D_m}{\left(\frac{\phi_{max}}{\phi}\right)^{1/3} - 1} - (0.15) \quad (5)$$

with  $D_m$  = Mean diameter of crystals [m],  
 $\beta$  = Constant, that varies with diameter,  
 $\phi_{max}$  = Concentration of solids at closest packing,  
 $\eta_R$  = Relative viscosity.

The relative viscosity is the one that is normalized to the viscosity of the crystal-free magma at the same temperature. Shaw [1969] uses experimental data to determine the temperature dependence of viscosity. The resulting expression becomes

$$\eta(T) = \eta_a e^{a/T} + \eta_0 [e^{b\phi} - 1] \quad T_s < T < T_l \quad (6)$$

Here  $\eta_a$ ,  $\eta_0$ ,  $a$  and  $b$  are empirical parameters from Shaw [1969].

$T_s$  = Solidus temperature,  
 $T_l$  = Liquidus temperature,  
 $\eta_0$  = 4 Pa s,  
 $\eta_a$  =  $4.8 \times 10^{-7}$  Pa s,  
 $a$  = 26500 K,  
 $b$  = 60.

Figure 13 shows the effect of crystal content on the relative viscosity of basalt, calculated using equation (4) for uniform spheres, serial sizes, after Marsh [1981], Shaw [1969] and Sherman [1968].

A comparison of the different functions reveals that the equations based on the Roscoe-Einstein relation, except when the value of Marsh is adapted, predict a relatively small influence of the crystal content on the relative viscosity. They do not account for possible elongation of the crystals, and therefore there is often a large discrepancy between measured viscosities of lava and those predicted by the Roscoe-Einstein equation. The equation of Sherman [1968] was developed for emulsions in which the oil droplets can deform, and is therefore not applicable to melts containing rigid crystals. The equation of Shaw [1969] is derived from experimental data of basaltic

lava and thus offers a good fit for modeling purposes. The constant derived by Marsh is also derived from experiments and thus also applicable.

Equations (4) to (6) assume that the viscosity of the liquid is independent of the degree of crystallization. Obviously, this is not the case in lava, since the composition of the groundmass changes with progressive crystallization.

Figure 14 shows the dependence of the relative viscosity on the mean diameter of the crystals calculated after McBirney and Murase [1984], including the change in viscosity of the liquid due to changes in the composition through crystallization. In the program, the composition of the crystals that would form in a liquid having the bulk composition of the magma is estimated and then subtracted to obtain the composition of the remaining liquid. Plagioclase is assumed to have perfect zoning, with a core in equilibrium with the initial liquid and subsequent growth reflecting the changing composition of the liquid. All other minerals are assumed to be unzoned, with compositions in equilibrium with the original (bulk) composition. The viscosity of the remaining (groundmass) liquid is calculated using Shaw's equation (6) and then corrected for the effect of suspended solids. Although this is a clearly defined algorithm

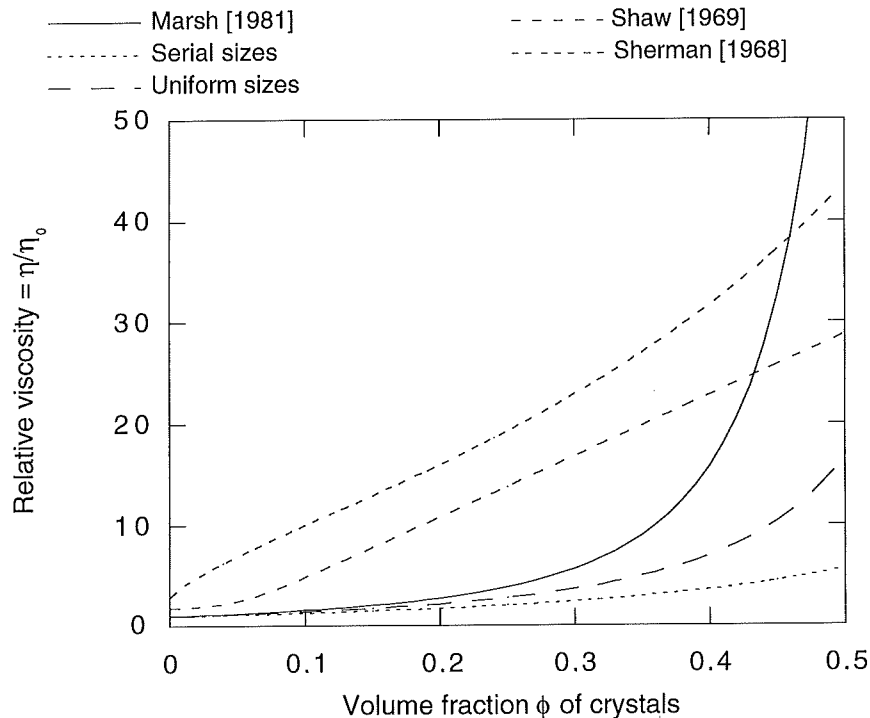


**Fig. 13** Effects of crystal content on the relative viscosity of basalt for uniform crystal size, serial crystal size, after Marsh [1981], and as calculated after Shaw [1969] and Sherman [1968].

to calculate the relative viscosity of the lava it was not incorporated into the modeling, since it would have meant a large increase in calculation time.

As a first approximation, the degree of crystallization (volume fraction of solid) is related to the temperature through the linear relationship [Dragoni and Tallarico, 1994]

$$\phi = \frac{T_l - T}{T_l - T_s} \phi_{sol} \quad (7)$$

where  $\phi_{sol}$  = Crystallization degree reached at the solidus.

Small amounts (<50%) of vesicles also raise the apparent viscosity of the lava [Sparks, 1978]. Nucleation and growth of bubbles start during the ascent of the magma in the conduit. A volume fraction of over 60% of spherical bubbles can impose a yield strength proportional to the surface tension of lava, when the bubbles form an interconnecting network. High stresses deform and stretch the bubbles, and since the viscosity of the gas is much less than that of the fluid, the bubbles lubricate the flow and the apparent viscosity decreases for even greater amounts of vesicles [Kerr and Lister, 1991].

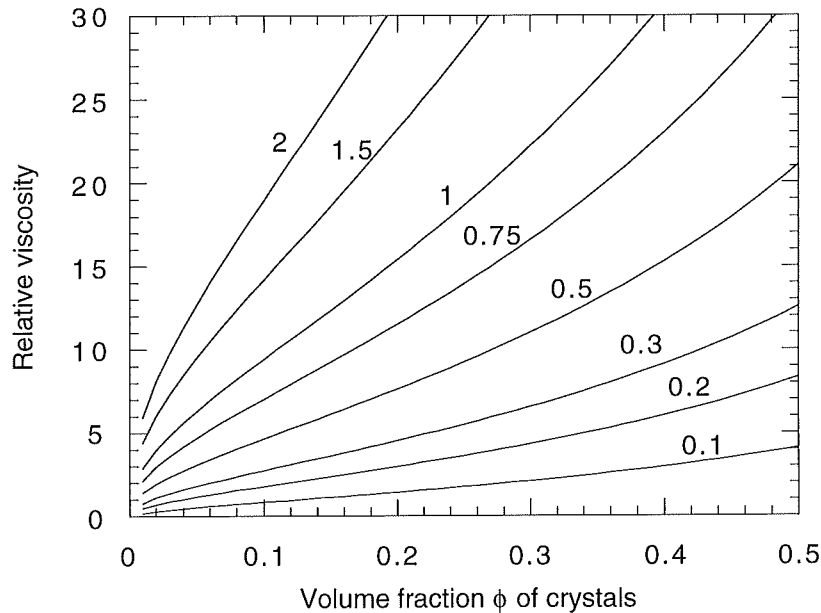


**Fig. 14** Effect of the mean crystal size [mm] of olivine crystals on the relative viscosity of basaltic lava. The change in composition through crystallization of olivine crystals is included.



For low stresses and small volume fractions of vesicles, surface tension prevents deformation of the bubbles and the viscosity of the lava is

$$\eta(\phi) = (1 + \phi) \eta_0 \quad (8)$$

Degassing of magma leads to undercooling of the lava through different processes [Sparks and Pinkerton, 1978]: initially, decompression and expansion of the gas phase cools the total magma system adiabatically. Second, the exsolution of gases raises the liquidus and alters the order of appearance of mineral phases. Sudden gas loss will upset the equilibrium and the melt becomes undercooled with respect to its anhydrous liquidus [Sparks and Pinkerton, 1978; Lipman et al, 1985].

Mid-ocean ridge tholeiitic lava is substantially undersaturated in H<sub>2</sub>O [Moore, 1970; Macpherson, 1984]. H<sub>2</sub>O will not enter the volatile phase as an important constituent at depths greater than ca. 500 m. Over 95 % of the gas in the vesicles is CO<sub>2</sub> [Moore et al, 1977; Marais and Moore, 1984]. Moore [1979] analyzed the vesicularity and gas content of tholeiitic basalt from different spreading ridges and found that vesicles and CO<sub>2</sub> are enriched in deep sea basalts that are also enriched in light rare earth and incompatible elements. Samples from the Mid-Atlantic Ridge showed a higher vesicularity (0.5-3%) than samples from the Pacific (0.1-0.5%), which may be due to different sizes and depths of the magma chambers or differences in the volatile content of the magma fed into the bottom of the magma chamber. The percentage of vesicles in Atlantic and Pacific samples was not high enough to have formed an interconnecting network of bubbles leading to a considerable decrease in the apparent viscosity, so eq. (8) can be applied.

It is possible to determine the depth of extrusion of basaltic lava from the volume percent of vesicles [Moore, 1965; Moore and Schilling, 1973].

Finally, the water content in submarine basalts influences its viscosity. Figure 15 shows an Arrhenius plot of the dependency of the viscosity on the H<sub>2</sub>O content. Analyses of deep sea tholeiites showed that it was undersaturated in H<sub>2</sub>O (0.06 to 0.42 wg%) [Moore, 1970]. Although, the effect of decrease of the viscosity due to the H<sub>2</sub>O content is only minor, it has been incorporated into the modeling.

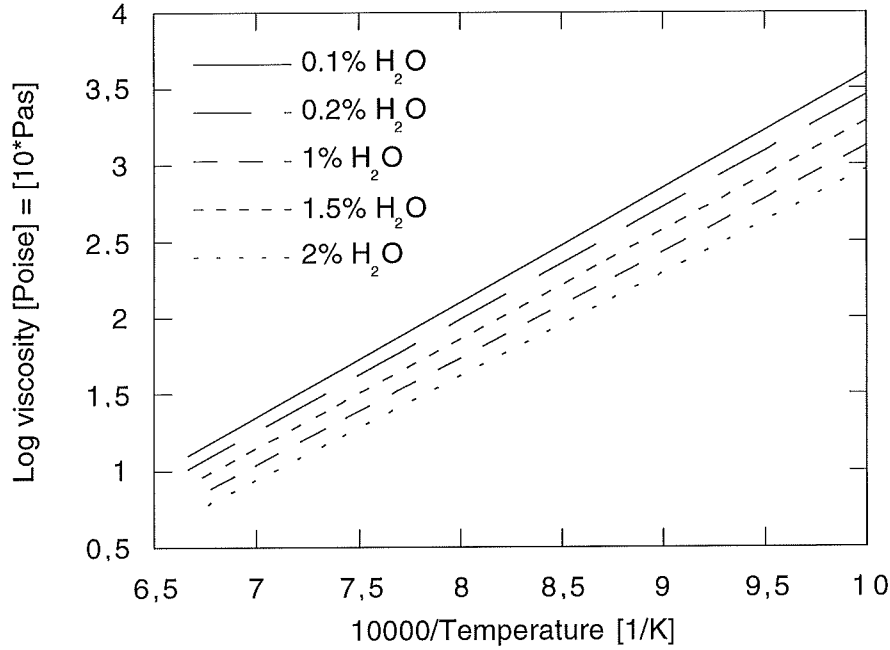


**Fig. 15** Arrhenius plot of the dependency of viscosity of basaltic silicate liquids on the  $\text{H}_2\text{O}$  content in weight percent.

## 8.2 Density

The density of basaltic lava can be calculated from its composition and temperature [Bottinga and Weill, 1972; Bottinga et al, 1982]. The mean molar volume at a reference temperature  $T_r$  is

$$T_r = \sum X_i \bar{V}_i^0 + X_A \bar{V}_A^0 \quad (9)$$

where  $\bar{V}_i^0$  = Constants derived from analysis of volume-composition relation in alumina-free silicate liquids,

$\bar{V}_A^0$  = Composition dependent apparent partial molar volume of  $\text{Al}_2\text{O}_3$ ,

$X_i$  = Mole fraction of component  $i$ ,

$X_A$  = Mole fraction of  $\text{Al}_2\text{O}_3$ .

The summation is taken over all oxide components except  $\text{Al}_2\text{O}_3$ , because of its potential dual role in the structure. The thermal expansion coefficient  $\alpha$  is given by

$$\alpha = \sum X_i \bar{\alpha}_i^0 + X_A \bar{\alpha}_A^0 \quad (10)$$

with  $\bar{\alpha}_i^0 =$  Constants independent of temperature and composition,  
 $\bar{\alpha}_A^0 =$  Composition-dependent term representing the effect of  $\text{Al}_2\text{O}_3$  on the thermal expansion.

The volume of lava at any temperature can then be calculated according to

$$V(T) = V_r \exp [\alpha (T - T_r)] \quad (11)$$

where  $V_r =$  Reference volume [ $\text{m}^3$ ],  
 $T_r =$  Reference temperature [K].

Densities for different basaltic compositions have been calculated after eqs. (9), (10) and (11). The results are shown in Figure 16. Only the density dependence on the composition and density changes due to thermal expansion are taken into account. The effects of crystallization of different phases on the density have been neglected.

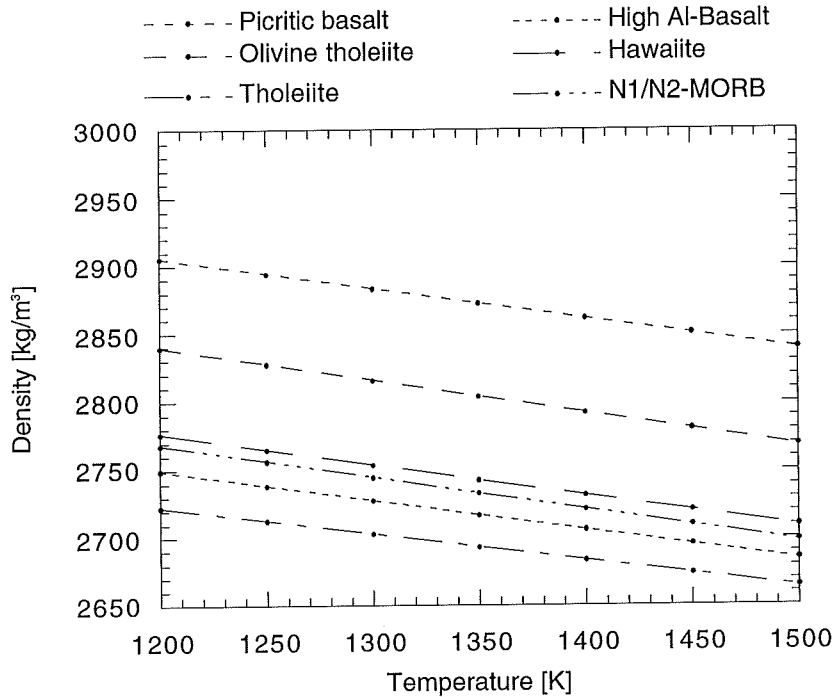


Fig. 16 Temperature dependency of the density of different basaltic lavas.

## 9 Description of the finite element model

In this study a 2-dimensional [Anonymous, 1986] and a 3-dimensional finite element program [Anonymous, 1992] are used to solve the conservation equations of momentum, energy, and mass conservation for varying rheological parameters of the fluid, the flow geometry, and boundary conditions.

The standard tubular model consists of 1080 brick shaped elements with smaller sizes in regions of presumably higher gradients. Figure 17 illustrates the boundary conditions for fluid flow and heat transfer, body forces and grid elements of the standard model tube.

A fixed temperature is assumed at the inlet of the tube. The surface of the upper half of the tube cools convectively whereas the surface of the lower half cools conductively because it is assumed to be buried in sediments. Flow velocities depend on the pressure gradient in the tube defined by the inlet and outlet pressures and by the gravity force. The flow velocities on the tube mantle are defined to be zero (no slip boundary condition) leading to a nearly parabolic velocity profile. The water depth determines the pressure boundary condition.

Viscosity and density of the lava are calculated from the magma composition. These relations were parameterized and included in the model. Both density and viscosity are modeled to be temperature dependent. The thermal conductivity is constant since the changes are very small in the temperature interval studied [Robertson, 1988]. The inlet pressure of the tube decreases with time as the lava supply from outside the tube decreases when the flow advances. Cooling becomes dominant over convection of hot material through the center of the tube at lower flow rates and solidification sets in. The release of latent heat is accounted for by appropriately adjusting the specific heat of the magma.

The equations governing laminar incompressible fluid flow are derived in the following subchapters (9.1.1) - (9.1.3). They are solved numerically in order to determine the fluid dynamic and thermodynamic behavior in a model pillow, using the finite element programs introduced in chapter (9.2). The subchapters (9.3) and (9.4) describe the standard model geometry, and flow and temperature fields for typical boundary conditions.

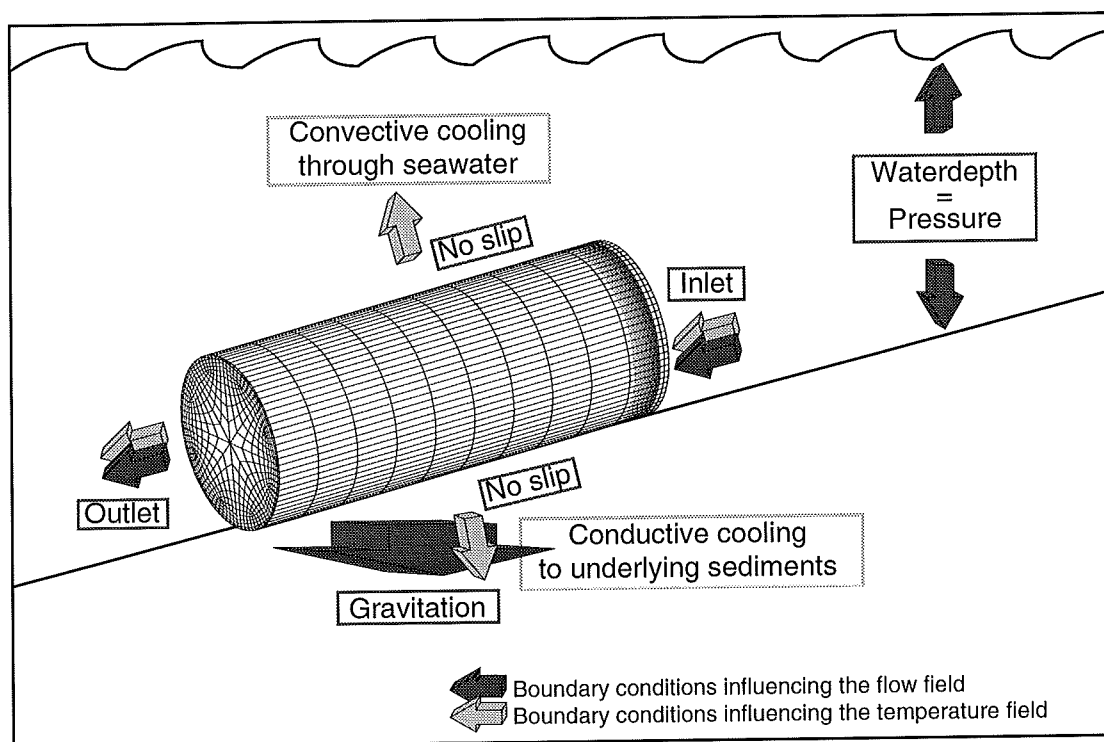


Fig. 17 Boundary conditions, body forces and grid elements of the model tube. At the inlet a fixed temperature is assumed. The upper half of the tube cools convectively whereas the lower half cools conductively because it is assumed to be buried in sediments. The flow velocity on the tube mantle is zero (no slip condition).

### 9.1 Equations governing fluid flow

It is important to determine whether the flow in the tube is laminar or turbulent, because the physical laws governing both types of flow are very different. Basaltic lava has a density of about  $2800 \text{ kg/m}^3$ , and at temperatures close to the liquidus a viscosity around 100 Pas. The velocity inside the pillow will not exceed 1 m/s, otherwise shearing of individual sacks would occur [Moore, 1975]. The Reynolds number of such a flow in a tube of 1 m diameter is about 28. Only at Reynolds numbers  $>2100$  would the flow become turbulent [Anderson et al, 1984]. Lava flows at Hawaii flow in laminar fashion even at steep slopes, leading to high flow velocities [Moore, 1987]. Laminar flow through a tube exhibits a simple parabolic velocity profile [Lydersen, 1979]. The velocity reaches the highest values in the center of the tube and is zero at the boundary due to friction at the inner wall, as described by the law of Hagen-Poiseuille [Gerthsen

et al, 1974]. The partial differential equations governing the laminar flow of an incompressible Newtonian fluid are the continuity equation, the equation of motion (Navier-Stokes equation), and the energy equation. The thermal effect of viscous dissipation can be included by solving the energy equation for total temperature.

### 9.1.1 The equation of continuity

The equation of continuity can be developed by writing a mass balance over a stationary volume element  $\Delta x \Delta y \Delta z$  through which a fluid is flowing (Figure 18)

$$\begin{bmatrix} \text{rate of} \\ \text{mass} \\ \text{accumulation} \end{bmatrix} = \begin{bmatrix} \text{rate of} \\ \text{mass} \\ \text{in} \end{bmatrix} - \begin{bmatrix} \text{rate of} \\ \text{mass} \\ \text{out} \end{bmatrix} \quad (12)$$

The rate of mass accumulation within the volume element is  $(\Delta x \Delta y \Delta z) (\partial \rho / \partial t)$ . The mass balance then becomes

$$\Delta x \Delta y \Delta z \frac{\partial \rho}{\partial t} = \Delta y \Delta z [\langle \rho v_x \rangle|_x - \langle \rho v_x \rangle|_{x+\Delta x}] + \Delta x \Delta z [\langle \rho v_y \rangle|_y - \langle \rho v_y \rangle|_{y+\Delta y}] + \Delta x \Delta y [\langle \rho v_z \rangle|_z - \langle \rho v_z \rangle|_{z+\Delta z}] \quad (13)$$

where  $\rho$  = Density of the fluid [ $\text{kgm}^{-3}$ ]  
 $v_x, v_y, v_z$  = Velocity in x,y,z-direction [ $\text{ms}^{-1}$ ].

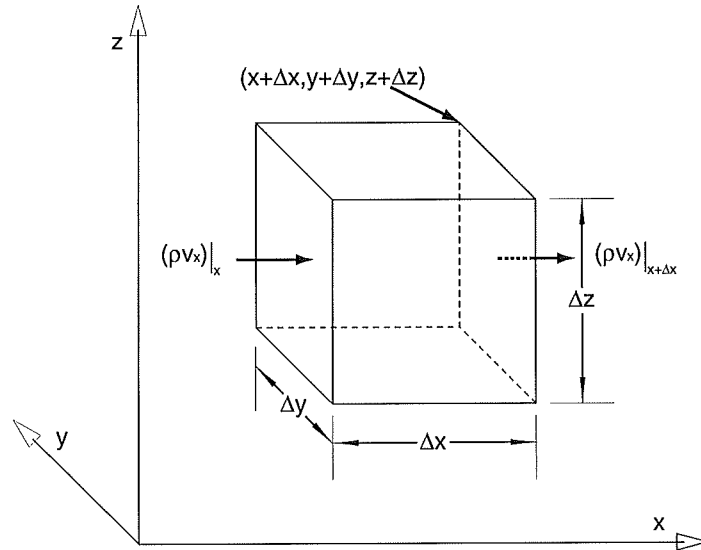


**Fig. 18** Region of volume  $\Delta x \Delta y \Delta z$  fixed in space through which a fluid is moving [after Bird et al, 1960].

Dividing the entire equation by  $(\Delta x \Delta y \Delta z)$  and taking the limit as these dimensions approach zero leads to the equation of continuity, which describes the change of density at a fixed point resulting from changes in the mass velocity.

$$\frac{\partial \rho}{\partial t} = -\left(\frac{\partial}{\partial x} \rho v_x + \frac{\partial}{\partial y} \rho v_y + \frac{\partial}{\partial z} \rho v_z\right) \quad (14)$$

Eq. (14) can be expressed as a vector equation

$$\frac{\partial \rho}{\partial t} = -(\nabla \cdot \rho \mathbf{v}) \quad (15)$$

For a fluid of constant density eq. (15) simplifies to

$$(\nabla \cdot \mathbf{v}) = 0 \quad (16)$$

### 9.1.2 The equation of motion

For a volume element  $\Delta x \Delta y \Delta z$  a momentum balance can be written [Bird et al, 1960]

$$\left[ \begin{array}{c} \text{rate of} \\ \text{momentum} \\ \text{accumulation} \end{array} \right] = \left[ \begin{array}{c} \text{rate of} \\ \text{momentum} \\ \text{in} \end{array} \right] - \left[ \begin{array}{c} \text{rate of} \\ \text{momentum} \\ \text{out} \end{array} \right] + \left[ \begin{array}{c} \text{sum of forces} \\ \text{acting on} \\ \text{system} \end{array} \right] \quad (17)$$

The net convective flow of x-momentum in the volume element expressed in Cartesian coordinates is

$$\begin{aligned} \Delta y \Delta z (\rho v_x v_x|_x - \rho v_x v_x|_{x+\Delta x}) + \Delta x \Delta z (\rho v_y v_x|_y - \rho v_y v_x|_{y+\Delta y}) \\ + \Delta x \Delta y (\rho v_z v_x|_z - \rho v_z v_x|_{z+\Delta z}) \end{aligned} \quad (18)$$

The net rate at which the x-component of momentum enters the face at x by molecular transport is

$$\Delta y \Delta z (\tau_{xx}|_x - \tau_{xx}|_{x+\Delta x}) + \Delta x \Delta z (\tau_{yx}|_y - \tau_{yx}|_{y+\Delta y}) + \Delta x \Delta y (\tau_{zx}|_z - \tau_{zx}|_{z+\Delta z}) \quad (19)$$

with  $\tau$  being the viscous stress tensor [Pa].

Here, the most important forces are those resulting from the fluid pressure  $p$  and the gravitational force per unit mass  $\mathbf{g}$ . The resulting force in the x-direction is

$$\Delta y \Delta z (p|_x - p|_{x+\Delta x}) + \rho g_x \Delta x \Delta y \Delta z \quad (20)$$

Finally, the rate of accumulation of x-momentum within the element is

$$\Delta x \Delta y \Delta z (\partial \rho v_x / \partial t) \quad (21)$$

where  $t$  is the time [s].

By substituting these expressions into eq. (17), dividing by  $\Delta x \Delta y \Delta z$  and taking the limits  $\Delta x \rightarrow 0, \Delta y \rightarrow 0, \Delta z \rightarrow 0$ , we obtain

$$\frac{\partial}{\partial t} \rho v_x = - \left( \frac{\partial}{\partial x} \rho v_x v_x + \frac{\partial}{\partial y} \rho v_y v_x + \frac{\partial}{\partial z} \rho v_z v_x \right) - \left( \frac{\partial}{\partial x} \tau_{xx} + \frac{\partial}{\partial y} \tau_{yx} + \frac{\partial}{\partial z} \tau_{zx} \right) - \frac{\partial p}{\partial x} + \rho g_x \quad (22)$$

Similar expressions can be obtained for the y- and z-components. It is convenient to sum them up as a single vector equation

$$\begin{array}{ccccc} \frac{\partial}{\partial t} \rho \mathbf{v} & = & -\nabla \cdot \rho \mathbf{v} \mathbf{v} & -\nabla p & -[\nabla \cdot \boldsymbol{\tau}] & + \rho \mathbf{g} \\ \text{rate of increase} & & \text{rate of momentum} & \text{pressure force} & \text{rate of momentum} & \text{gravitational} \\ \text{of momentum per} & & \text{gain by convection} & \text{on element per} & \text{gain by viscous} & \text{force on element} \\ \text{unit. volume} & & \text{per unit volume} & \text{unit volume} & \text{transfer per unit} & \text{per unit} \\ & & & & \text{volume} & \text{volume} \end{array} \quad (23)$$

With the help of the equation of continuity and for constant  $\rho$  and constant  $\eta$  eq (23) can be simplified to the Navier-Stokes equation

$$\rho \frac{D\mathbf{v}}{Dt} = -\nabla p + \rho \mathbf{g} \quad (24)$$

For Newtonian fluids the various stresses can be expressed in terms of velocity gradients and fluid properties

$$\begin{aligned} \tau_{xx} &= -2\eta \frac{\partial v_x}{\partial x} + \frac{2}{3}\eta (\nabla \cdot \mathbf{v}) \\ \tau_{yy} &= -2\eta \frac{\partial v_y}{\partial y} + \frac{2}{3}\eta (\nabla \cdot \mathbf{v}) \\ \tau_{zz} &= -2\eta \frac{\partial v_z}{\partial z} + \frac{2}{3}\eta (\nabla \cdot \mathbf{v}) \\ \tau_{xy} = \tau_{yx} &= -\eta \left( \frac{\partial v_x}{\partial y} + \frac{\partial v_y}{\partial x} \right) \\ \tau_{yz} = \tau_{zy} &= -\eta \left( \frac{\partial v_y}{\partial z} + \frac{\partial v_z}{\partial y} \right) \\ \tau_{zx} = \tau_{xz} &= -\eta \left( \frac{\partial v_z}{\partial x} + \frac{\partial v_x}{\partial z} \right) \end{aligned} \quad (25)$$

where  $\eta$  is the viscosity of the fluid [Pa s].



### 9.1.3 The equation of energy

In a stationary volume element through which a pure fluid is moving, the law of conservation of energy at any given time is [Bird et al, 1960]

$$\begin{aligned}
 \left[ \begin{array}{c} \text{rate of} \\ \text{accumulation} \\ \text{of internal} \\ \text{and kinetic} \\ \text{energy} \end{array} \right] &= \left[ \begin{array}{c} \text{rate of} \\ \text{internal and} \\ \text{kinetic energy} \\ \text{in} \\ \text{by convection} \end{array} \right] - \left[ \begin{array}{c} \text{rate of} \\ \text{internal and} \\ \text{kinetic energy} \\ \text{out} \\ \text{by convection} \end{array} \right] \\
 &+ \left[ \begin{array}{c} \text{net rate} \\ \text{of heat} \\ \text{addition} \\ \text{by} \\ \text{conduction} \end{array} \right] - \left[ \begin{array}{c} \text{net rate} \\ \text{of work} \\ \text{done by} \\ \text{system on} \\ \text{surroundings} \end{array} \right]
 \end{aligned} \tag{26}$$

For a fixed volume element  $\Delta x \Delta y \Delta z$  the rate of accumulation of internal and kinetic energy is

$$\Delta x \Delta y \Delta z \frac{\partial}{\partial t} \left( \rho \hat{U} + \frac{1}{2} \rho v^2 \right) \tag{27}$$

where  $\hat{U}$  is the internal energy [J].

The net rate of convection of internal and kinetic energy into the element is

$$\begin{aligned}
 &\Delta y \Delta z \{ v_x (\rho \hat{U} + 1/2 \rho v^2) \big|_x - v_x (\rho \hat{U} + 1/2 \rho v^2) \big|_{x+\Delta x} \} \\
 &+ \Delta x \Delta z \{ v_y (\rho \hat{U} + 1/2 \rho v^2) \big|_y - v_y (\rho \hat{U} + 1/2 \rho v^2) \big|_{y+\Delta y} \} \\
 &+ \Delta x \Delta y \{ v_z (\rho \hat{U} + 1/2 \rho v^2) \big|_z - v_z (\rho \hat{U} + 1/2 \rho v^2) \big|_{z+\Delta z} \}
 \end{aligned} \tag{28}$$

The net rate of energy input by conduction is

$$\Delta y \Delta z \{ q_x \big|_x - q_x \big|_{x+\Delta x} \} + \Delta x \Delta z \{ q_y \big|_y - q_y \big|_{y+\Delta y} \} + \Delta x \Delta y \{ q_z \big|_z - q_z \big|_{z+\Delta z} \} \tag{29}$$

where  $q$  equals the energy flux relative to mass average velocity [ $\text{Jm}^{-3}$ ].

The rate of work done against the three components of the gravitational force per unit mass is

$$-\rho \Delta x \Delta y \Delta z (v_x g_x + v_y g_y + v_z g_z) \tag{30}$$

The rate of work done against the static pressure  $p$  at the six faces of  $\Delta x \Delta y \Delta z$  is

$$\Delta y \Delta z \{ (pv_x)|_{x+\Delta x} - (pv_x)|_x \} + \Delta x \Delta z \{ (pv_y)|_{y+\Delta y} - (pv_y)|_y \} + \Delta x \Delta y \{ (pv_z)|_{z+\Delta z} - (pv_z)|_z \} \quad (31)$$

and the rate of work done against the viscous forces is

$$\begin{aligned} & \Delta y \Delta z \{ (\tau_{xx}v_x + \tau_{xy}v_y + \tau_{xz}v_z)|_{x+\Delta x} - (\tau_{xx}v_x + \tau_{xy}v_y + \tau_{xz}v_z)|_x \} \\ & + \Delta x \Delta z \{ (\tau_{yx}v_x + \tau_{yy}v_y + \tau_{yz}v_z)|_{y+\Delta y} - (\tau_{yx}v_x + \tau_{yy}v_y + \tau_{yz}v_z)|_y \} \\ & + \Delta x \Delta y \{ (\tau_{zx}v_x + \tau_{zy}v_y + \tau_{zz}v_z)|_{z+\Delta z} - (\tau_{zx}v_x + \tau_{zy}v_y + \tau_{zz}v_z)|_z \} \end{aligned} \quad (32)$$

Substitution of these expressions into equation (26) and taking the limits as  $\Delta x$ ,  $\Delta y$  and  $\Delta z$  approach zero leads to

$$\begin{aligned} \frac{\partial}{\partial t}(\rho \hat{U} + \frac{1}{2}\rho v^2) = & -(\frac{\partial}{\partial x}v_x(\rho \hat{U} + \frac{1}{2}\rho v^2) + \frac{\partial}{\partial y}v_y(\rho \hat{U} + \frac{1}{2}\rho v^2) + \frac{\partial}{\partial z}v_z(\rho \hat{U} + \frac{1}{2}\rho v^2)) \\ & -(\frac{\partial q_x}{\partial x} + \frac{\partial q_y}{\partial y} + \frac{\partial q_z}{\partial z}) + \rho(v_x g_x + v_y g_y + v_z g_z) \\ & -(\frac{\partial}{\partial x}pv_x + \frac{\partial}{\partial y}pv_y + \frac{\partial}{\partial z}pv_z) \\ & -(\frac{\partial}{\partial x}(\tau_{xx}v_x + \tau_{xy}v_y + \tau_{xz}v_z) + \frac{\partial}{\partial y}(\tau_{yx}v_x + \tau_{yy}v_y + \tau_{yz}v_z) \\ & + \frac{\partial}{\partial z}(\tau_{zx}v_x + \tau_{zy}v_y + \tau_{zz}v_z)) \end{aligned} \quad (33)$$

or in vector notation

$$\begin{aligned} \frac{\partial}{\partial t}(\rho \hat{U} + \frac{1}{2}\rho v^2) = & -(\nabla \cdot \rho v^2(\hat{U} + \frac{1}{2}v^2)) - (\nabla \cdot q) \\ & + \rho(v \cdot g) - (\nabla \cdot p v) \\ & - (\nabla \cdot [\tau \cdot v]) \end{aligned} \quad (34)$$

*rate of gain of energy per unit volume*      *rate of energy input per unit volume by convection*      *rate of energy input per unit volume by conduction*  
*rate of work done on fluid per unit volume by gravitational forces*      *rate of work done on fluid per unit volume by pressure forces*  
*rate of work done on fluid per unit volume by viscous forces*

After rearranging the equation of energy with the aid of the equations of continuity and motion, one finds for Newtonian fluids with constant thermal conductivity

$$\rho c_v \frac{DT}{Dt} = \lambda \nabla^2 T - T \left( \frac{\partial p}{\partial T} \right) (\nabla \cdot \mathbf{v}) + \eta \Phi \quad (35)$$

where  $c_v$  = Heat capacity at constant volume, per unit mass [ $\text{J kg}^{-1} \text{K}^{-1}$ ],

$T$  = Temperature [K],

$\lambda$  = Thermal conductivity [ $\text{J s}^{-1} \text{m}^{-1} \text{K}^{-1}$ ],

$\eta$  = Viscosity [ $\text{Pa s}$ ],

and where  $\Phi$  is the dissipation function

$$\Phi = 2 \left[ \left( \frac{\partial v_x}{\partial x} \right)^2 + \left( \frac{\partial v_y}{\partial y} \right)^2 + \left( \frac{\partial v_z}{\partial z} \right)^2 \right] + \left( \frac{\partial v_y}{\partial x} + \frac{\partial v_x}{\partial y} \right)^2 + \left( \frac{\partial v_z}{\partial y} + \frac{\partial v_y}{\partial z} \right)^2 + \left( \frac{\partial v_x}{\partial z} + \frac{\partial v_z}{\partial x} \right)^2 - \frac{2}{3} \left( \frac{\partial v_x}{\partial x} + \frac{\partial v_y}{\partial y} + \frac{\partial v_z}{\partial z} \right)^2 \quad (36)$$

## 9.2 FLOTRAN and PDE/PROTRAN

FLOTRAN is a finite element fluid flow analysis software package for the treatment of two- and three-dimensional viscous flow including a steady state and a transient solution algorithm [Anonymous, 1992]. It supports ANSYS as a pre- and post processing package and was used on a SUN Sparc 10 workstation. It includes the following boundary condition types: prescribed nodal values, symmetry, adiabatic, prescribed heat flux, heat source, film coefficient, periodic boundary and moving boundary/stationary mesh. It solves the Navier-Stokes equations, a pressure equation (derived by substituting the momentum equations into the continuity equation), the energy equation and two equations of a turbulence model. FLOTRAN uses the compressible formulation of the equation of continuity to solve incompressible problems with varying density. The Navier-Stokes equations are simplified, which is the most numerically efficient and accurate way to solve non-isothermal problems, particularly those involving natural convection. The output of FLOTRAN includes: temperature, velocity, density, and viscosity distributions as well as energy and fluid flow rates, minimum and maximum values of every variable and convergence parameters. The finite element program ANSYS was used for the postprocessing to display the different variables.

PDE/PROTRAN solves quite general time-dependent, steady-state, and eigenvalue systems of partial differential equations in two dimensions [Anonymous, 1986]. Quadratic, cubic or quartic isoparametric triangular elements and different solver capabilities are offered [Sewell, 1985]. Automatic refinement and grading of the mesh and graphical output capabilities are included. At the beginning of the model calculations PDE/PROTRAN was used for the modeling of the flow rates in pillows and sheet flows with different viscosities and slope angles. As work progressed further, it became necessary to incorporate 3-dimensional features into the models and FLOTRAN proved to be more efficient for the calculation of fluid flow problems, since it is designed to solve these.

### 9.3 Model geometry

The standard model consists of 1080 brick elements with 1397 nodes, defined by 24 lines and 17 areas (Figure 19). In some models, the number of elements was slightly higher to prevent the generation of highly elongated elements. Only one half of the tube is modeled with a symmetry boundary condition in the center plane. A Cartesian coordinate system is used instead of a cylindrical, because the problem is not cylindrically symmetric once the gravitational force is included. The standard model tube is 2.5 m long and has a diameter of 0.5 m. Other lengths and shapes were also examined. The elements are distributed symmetrically with respect to the x-y central plane. The smaller elements lie on the outer boundary of the model where the largest temperature

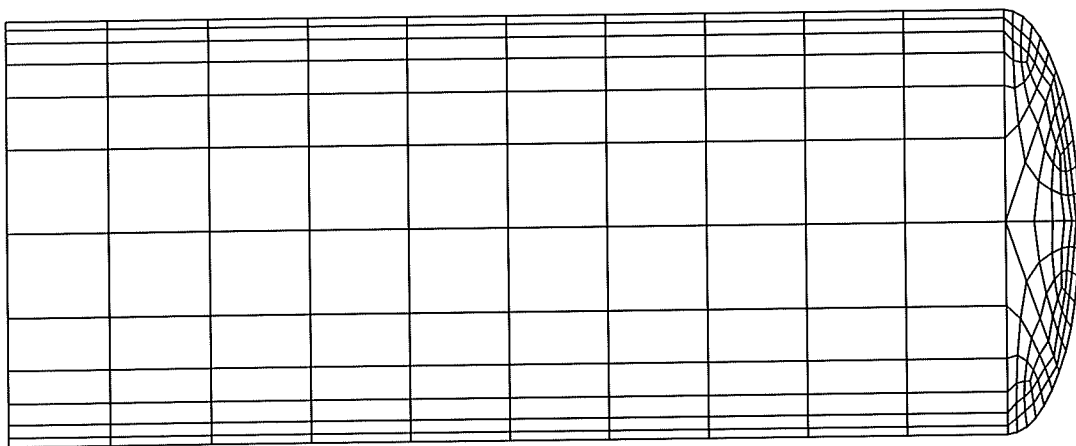


**Fig. 19** Element distribution of the model. The smaller elements lie on the outer boundary of the model where the largest temperature and velocity gradients are expected.

and velocity gradients are expected. The most extreme aspect ratio of an element is 1:17.8. The number of nodes is limited by the computer capacity and calculation time.

#### 9.4 Flow- and temperature fields from typical boundary conditions

The standard model consists of a tube cooled from the outside by convection and conduction. The resulting temperature and velocity fields show a high gradient region in the outer parts of the tube (Figure 20).

Convective cooling is efficient at cooling the outer part of the tube down to the temperature of seawater. The highest temperature gradients are encountered along the cooled boundaries, while inside the tube the temperature is homogeneous. The boundary region widens in later time steps and at lower velocities. Thermal energy is predominantly transported convectively within the flowing lava, and through conduction to the outer boundaries.

Also shown in Figure 20 is a typical flow field at the beginning of a model run and the distribution of the already solidified outer shell in the same step. Liquid elements are light white while solid elements are black. The hot fluid is flowing at a velocity dependent on the pressure gradient inside the tube, the viscosity of the fluid and the gravitational acceleration along the slope. The highest velocities occur in the middle of the tube. Near the periphery, the flow is significantly retarded due to frictional drag at the tube walls. The flow velocity profile is nearly parabolic (Poiseuille profile) at the beginning, but changes as solidification progresses, in particular at the boundaries further downstream. The viscosity depends exponentially on the temperature and contributes to the small flow velocities at the outer parts of the tube. At low flow velocities, where the cooling effect is larger, sinking of some cooler, denser material can occur.

Only the outermost and a few neighboring elements near the end of the tube are cooled below the solidus and have been changed to solid elements. They form an insulating sheath around the hot, flowing lava. A no-slip boundary condition is applied to them automatically. In later time steps or at lower flow velocities, the whole tube can solidify when flow stops.

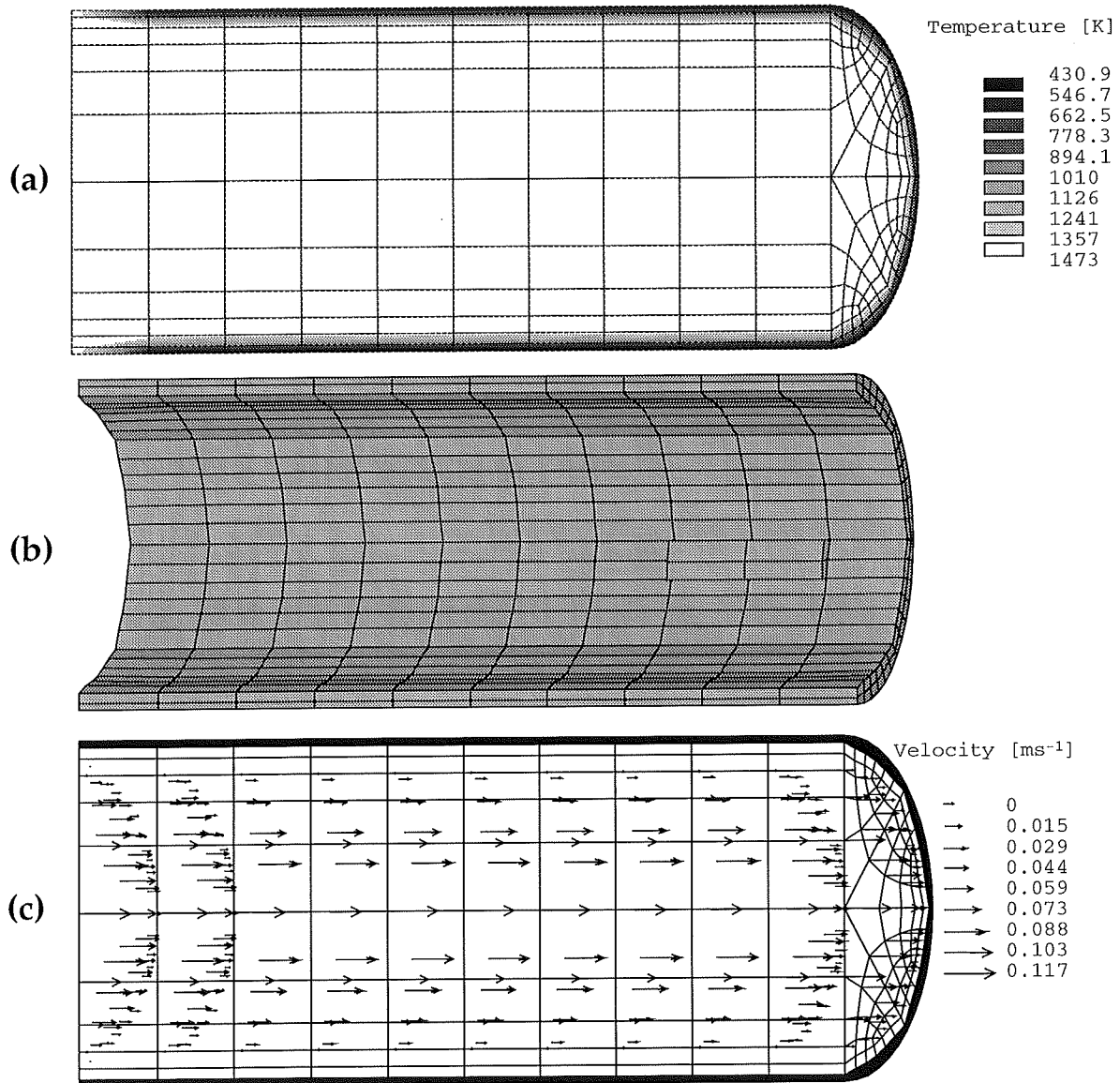


**Fig. 20** Resulting temperature, element type and velocity distribution in the model.  
 (a) Temperature field: the lower half overlying the substrate cools conductively, while the upper half cools more rapidly due to convection of seawater. This is however, counteracted by the sinking of cooler, denser material.  
 (b) Element type: peripheral elements, which have solidified and have been reassigned a lower heat capacity and infinite viscosity. They form an insulating sheath around the hot, flowing magma. Note the four additional elements in the right central part of the tube which have solidified.  
 (c) Flow field: flow velocities are governed by the pressure gradient and the component of the gravitational force along the slope. The highest velocities occur in the middle of the tube. Near the periphery the flow is significantly retarded due to frictional drag at the tube walls. Liquid elements are white while solid elements are black.

## 10 Analytical solution: Tube flow with constant heat flux at a wall

One model calculation for constant density and viscosity and no solidification has been carried out in order to compare it to the results of the Poiseuille equation for laminar flow in a tube [Gerthsen et al, 1974], namely,

$$v_z = \frac{\Delta P}{4L_T\eta} (R^2 - r^2) \quad (37)$$

where  $L_T$  = Length of the tube [m],  
 $R$  = Radius of the tube [m],  
 $r$  = Radial distance [m],  
 $\Delta P$  = Pressure drop along the tube [Pa m<sup>-1</sup>],  
 $v_z$  = Velocity in z-direction [m s<sup>-1</sup>].

The highest velocity, which occurs in the middle of the tube (at  $r = 0$ ) is 0.1593 m s<sup>-1</sup> for a 5 m long tube with 0.5 m radius and a fluid viscosity of 15.69 Pa s. The highest velocity in the model calculation at the end of the tube was 0.1492 m s<sup>-1</sup> which results in an error of 6.5%. For nodes at other radii see Table 2. One reason for the differences

**TABLE 2.** Difference between the flow-velocities of the Poiseuille equation and the model calculation.

r [m]	$v_{\text{theo}}$ [m/s]	$v_z$ [m/s]	Discrepancy [%]
0.5	0	0	0
0.48	1.23E-02	1.35E-02	9.02
0.44	3.08E-02	3.14E-02	1.96
0.39	5.75E-02	5.75E-02	0
0.32	9.35E-02	9.24E-02	1.17
0.19	1.34E-01	1.29E-01	3.96
0	1.59E-01	1.51E-01	5.03

might be deviations from the parabolic velocity profile at the tube inlet. The mechanical entrance length of the tube is

$$\frac{S_L}{2R} = 0.06 Re \quad (38)$$

$S_L$  = Mechanical entry length of the tube,  
 $Re$  = Reynolds number.

In this problem, the Reynolds number is 27.06 which produces an entry length of 0.812 m. At this length the flow velocity is within 5% of the Poiseuille value. Another reason for the misfit is the coarser grid in the middle of the tube. It has been chosen to minimize calculation time.

The solution for the temperature profile of a tube with constant heat flux at the wall cannot be solved completely analytically. A sketch of the problem and the notation are shown in Figure 21. A convective heat flux at the wall further complicates the problem. An analytical solution for steady state conditions can be found when the curvature effects are neglected and the problem is treated as if the wall were flat. Then, the velocity profile may be regarded as linear, with a slope given by the true slope at the wall [Bird et al, 1960]

$$v_z(s) = v_0 s/R \quad v_0 = (p_0 - p_L) R^2 / 2\eta L_T \quad (39)$$

where  $p_0$  = pressure at  $z = 0$  [Pa],  
 $p_L$  = pressure at  $z = L_T$  [Pa],

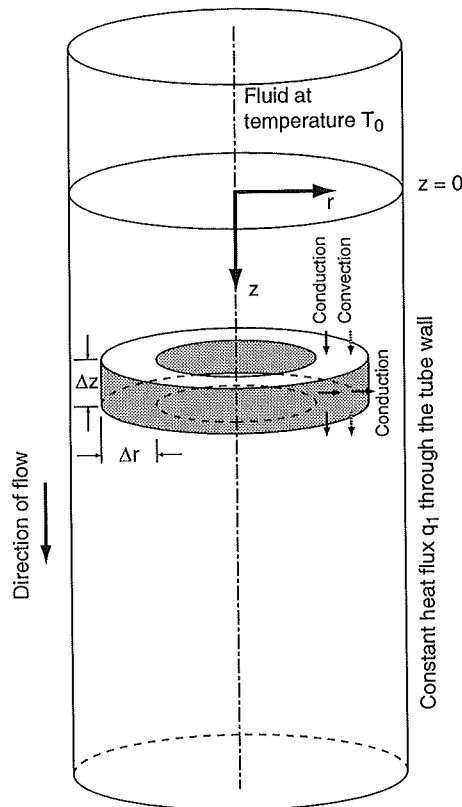


**Fig. 21** Tube flow with constant heat flux over the wall [after Bird et al, 1960].



and  $s = R-r$ . The energy equation for this model is

$$v_0 \left( \frac{s}{R} \right) \frac{\partial T}{\partial z} = \kappa \frac{\partial^2 T}{\partial s^2} \quad (40)$$

Dividing this equation by  $s$  and differentiating with respect to  $s$  yields

$$v_0 \left( \frac{1}{R} \right) \frac{\partial q_s}{\partial z} = \kappa \frac{\partial}{\partial s} \left( \frac{1}{s} \frac{\partial q_s}{\partial s} \right) \quad (41)$$

Introducing the dimensionless variables

$$\Psi = \frac{q_s}{q_1} \quad \eta = \frac{s}{R} \quad \lambda = \frac{z\kappa}{v_0 R^2} \quad (42)$$

equation (41) becomes

$$\frac{\partial \Psi}{\partial \lambda} = \frac{\partial}{\partial \eta} \left( \frac{1}{\eta} \frac{\partial \Psi}{\partial \eta} \right) \quad (43)$$

The boundary conditions are

$$\begin{aligned} \Psi &= 0 & \text{at} & \lambda = 0 & , \\ \Psi &= 1 & \text{at} & \eta = 0 & , \\ \Psi &= 0 & \text{at} & \eta = \infty & , \end{aligned} \quad (44)$$

A solution can be achieved with the method of combination of variables and using the new independent variable

$$\chi = \frac{\eta}{\sqrt[3]{9\lambda}} \quad (45)$$

This leads to the heat flux equation

$$\chi \Psi + (3\chi^3 - 1) \Psi' = 0 \quad (46)$$

where the accent means differentiation with respect to  $\chi$ . The solution is

$$\Psi = \frac{\int_0^\infty \chi e^{-\chi^3} d\chi}{\int_0^\infty \chi e^{-\chi^3} d\chi} = \frac{3}{\Gamma(\frac{2}{3})} \int_0^\infty \chi e^{-\chi^3} d\chi \quad (47)$$

To obtain the temperature profile, the following equation has to be integrated

$$\int_T^{T_0} dT = -\frac{1}{k} \int_s^\infty q_s ds \quad (48)$$

or, expressed in dimensionless quantities,

$$\Theta = \frac{T - T_0}{q_1 R / k} = \sqrt[3]{9\lambda} \int_\chi^\infty \psi d\chi \quad (49)$$

Insertion of the expression for  $\psi$  into eq. (49) gives

$$\Theta = \sqrt[3]{9\lambda} \left[ \frac{e^{-\chi^3}}{\Gamma(\frac{2}{3})} - \chi \left\{ 1 - \frac{\Gamma(\frac{2}{3}, \chi^3)}{\Gamma(\frac{2}{3})} \right\} \right] \quad (50)$$

Here,  $\Gamma(\frac{2}{3})$  is the complete and  $\Gamma(\frac{2}{3}, \chi^3)$  is the incomplete gamma function. This solution can be compared to the numerical solution with appropriate properties and boundary conditions (see Table 3). Good agreement between the numerical and the analytical solution is found, with an error not larger than 0.34 % on the whole profile. Part of the deviations might be due to neglecting the curvature effect in the analytical solution and due to the grid spacing.

**TABLE 3.** Difference between the analytical solution and the numerical solution for a tube with constant heat flux at the wall.

r [m]	T [K]	T [K]	Discrepancy [%]
0.5	1450.1	1455	0.34
0.48	1471.6	1470.28	0.09
0.44	1473	1473	0
0.39	1473	1473	0
0.32	1473	1473	0
0.19	1473	1473	0
0	1473	1473	0

Some tests with different numbers of nodes have been performed to see, whether higher node densities lead to significantly reduced errors. For longer runs the number cannot be too high because of the resulting long calculation times.

Because of the symmetry of the mesh, the node density can only be increased in steps. For this test the number of nodes in the x- and y-directions of the model have been chosen as 9, 13, 17, and 21. The number of nodes in the z-direction has been chosen appropriately, to avoid extreme aspect ratios of individual elements. The resulting mean error, the CPU-time used and the number of nodes in y-direction of the different models are shown in Figure 22.

For longer model runs, especially the time-dependent runs, the model with 13 nodes in x- and y-directions has been chosen, because the calculation times would be too long for even larger numbers of nodes. Some other models have been calculated with higher node numbers to ensure high precision of the results.

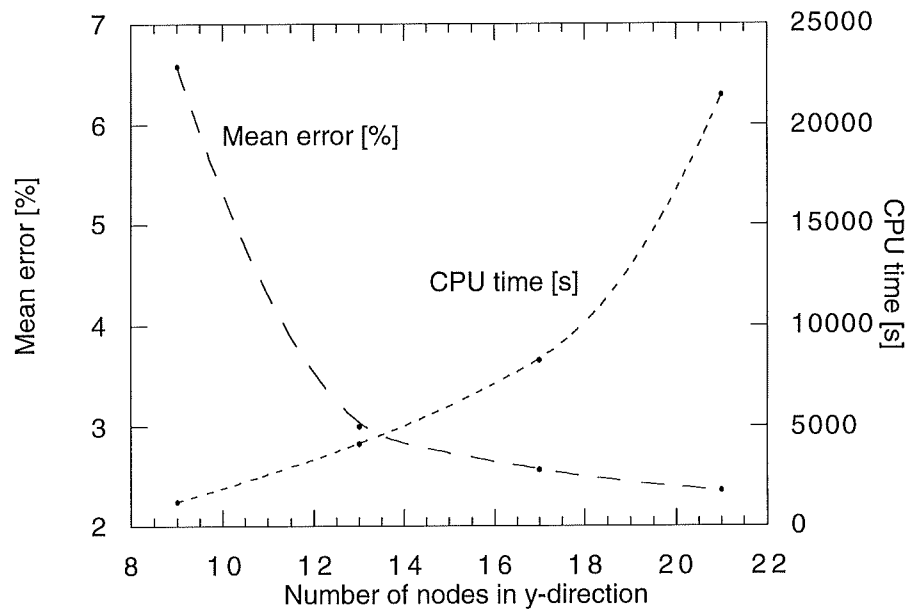


**Fig. 22** Mean calculation error and CPU-time of four different models with increasing node numbers.

## 11 Numerical solutions: Variation of a single parameter

In order to verify the influence of the different parameters on the model calculations, various model runs were made with the variation of only a single parameter at a time. The fundamental parameters are then included into the final models, while insignificant ones are omitted since they unnecessarily use additional CPU-time. In the following subchapters (11.1) and (11.2) the influence of the viscosity and slope angle on the flow rates is calculated. The release of latent heat of crystallization is discussed in subchapter (11.5). The viscous heating, the influence of the temperature dependent density, and different cooling functions are examined in subchapters (11.3), (11.4), and (11.6).

### 11.1 Effects of the viscosity on the flow rate

The viscosity of lava depends on the composition, the temperature and the crystallinity of the lava as described in chapter (8.1). For different basaltic compositions and using the temperature-viscosity dependency, the flow rates in a steady state model run were calculated and compared at different input pressures (Figure 23). This

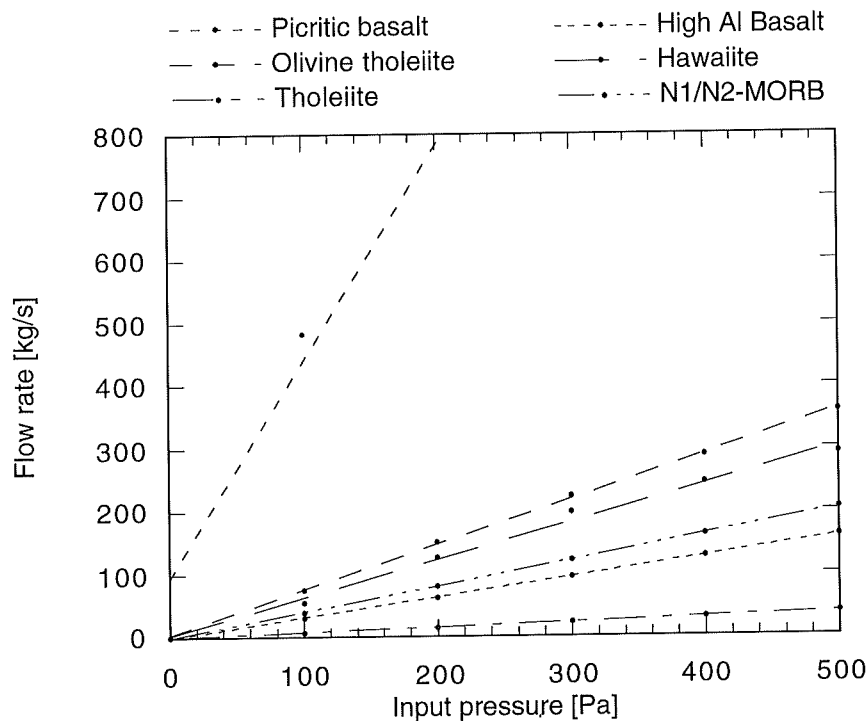
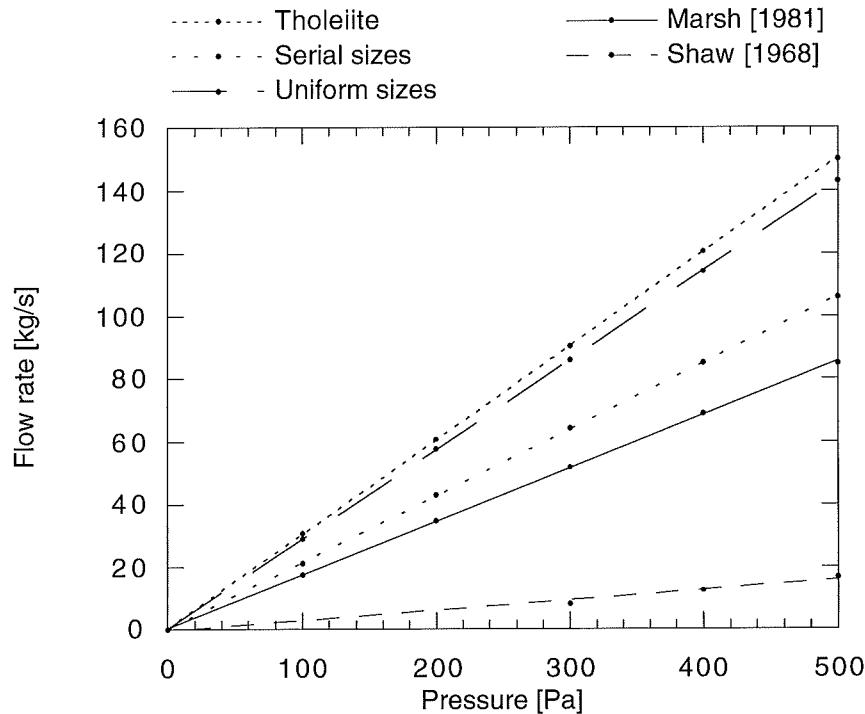


Fig. 23 Flow rates of different compositions of basaltic rocks.

pressure controls the flow velocities inside the tube. The resultant flow rates depend strongly on the chosen viscosity function even for small compositional changes or small changes of the input pressure. The lavas with the lowest viscosity exhibit the highest flow rates, as would be expected.

Different model runs were made to investigate the effect of crystal content on the flow rates. Crystal content within each element is determined from the element temperature using Eq. (7) and the viscosity is calculated with the Einstein-Roscoe equation and the equation of Shaw [1969]. The resulting flow rates are compared to that of crystal free tholeiite in Figure 24. The flow rate reduction calculated after Shaw is larger than the reduction after the Einstein-Roscoe equation.

Figure 25 shows the effects of the viscosity of the lava on the mean flow rate per square meter cross-section of a pillow (2 -dimensional: 1 m diameter) and a sheet flow (2-dimensional: 10 m diameter), both at a slope angle of 30°. The flow rates decrease rapidly at higher viscosities and the flow rate of the sheet flow is higher than that of the pillow, because of the higher velocities reached in the middle of the sheet flow at the



**Fig. 24** Effect of the crystal content on the flow rate calculated with the Einstein-Roscoe equation for serial and uniform sizes, after Marsh [1981] and Shaw [1968]

same viscosity. This is simply due to the much higher frictional drag at the edges of the 1 m diameter pillow compared to a section of equal area in a 10 m thick sheet flow. One reason why tubes generally do not form from intermediate or silicic lava is that even at steep slope angles, only moderate flow rates are possible; at higher yield strengths flow would cease. However, when the viscosity of silicic lavas is reduced by high  $H_2O$  concentrations they are also able to flow in tubes [Bednarz, 1988; Kano et al, 1991]. Highly viscous lavas generally build thicker lava flows, while basaltic lavas are also able to flow in smaller tubes.

For most of the remaining model calculations in this thesis a simple Newtonian temperature dependent viscosity function of tholeiitic lava [McBirney, 1994] was chosen (see Figure 12), since most of the pillows of the oceanic crust show a tholeiitic composition [Moore, 1975].

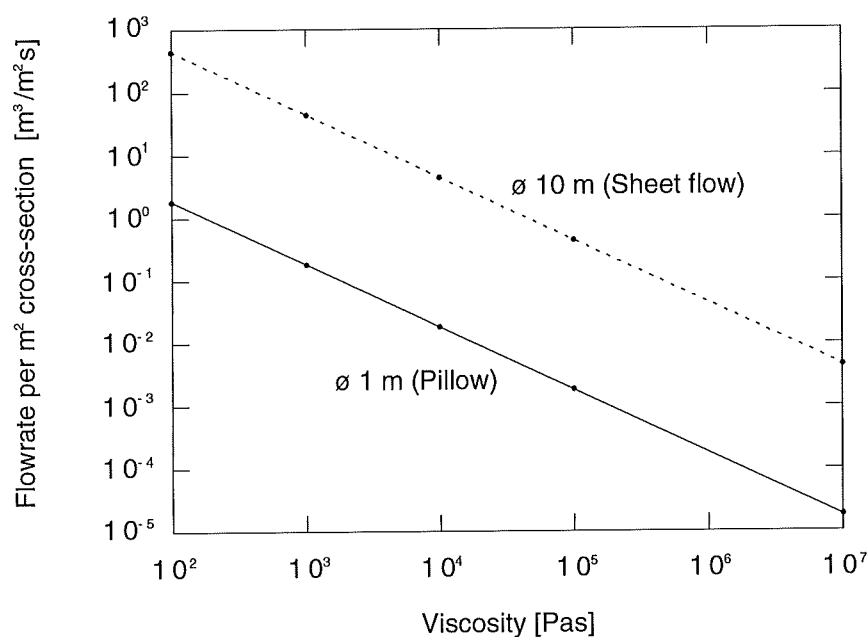


**Fig. 25** Effects of the viscosity of the lava on the mean flow rate per  $m^2$  cross-section of a pillow (1 m diameter) and a sheet flow (10 m diameter).

## 11.2 Effect of the slope angle on the flow rate

The downslope component of the gravitational force is higher for steeper slope angles, resulting in larger flow rates. These often lead to the formation of sheet flows rather than pillows. On slopes steeper than  $30^\circ$ , most pillows have a smooth surface due to the faster flow velocities inside [Moore et al, 1971]. At steep slopes but relatively small flow rates, the lava transport is too high to form pillows, and large fragments detach, tumble down the slope and form single sack-like pillows [Walker, 1992]. In Figure 26 the dependency of the mean flow rate per square meter cross-section of the slope angle is shown for a 10 m thick sheet flow and a 1m diameter pillow at constant 100 and 1000 Pa s viscosities. The average slope of a volcanic island like Hawaii is around  $2^\circ$ , the average slope of MORs is even less. Locally the slope angle can be much steeper. The density in these calculations was reduced to  $1800 \text{ kg m}^{-3}$ , to include the buoyancy effect in water. However, calculations including temperature distributions were made without reducing the density, because this would lead to spurious masses, heat capacities, and thus element temperatures. All calculations depending on the inflow pressure are calculated without the force of gravity (see chapter 12.5), since it would impair the results. The inflow pressure in these models consists of the sum of the overpressure of the eruption and the pressure gradient due to the slope

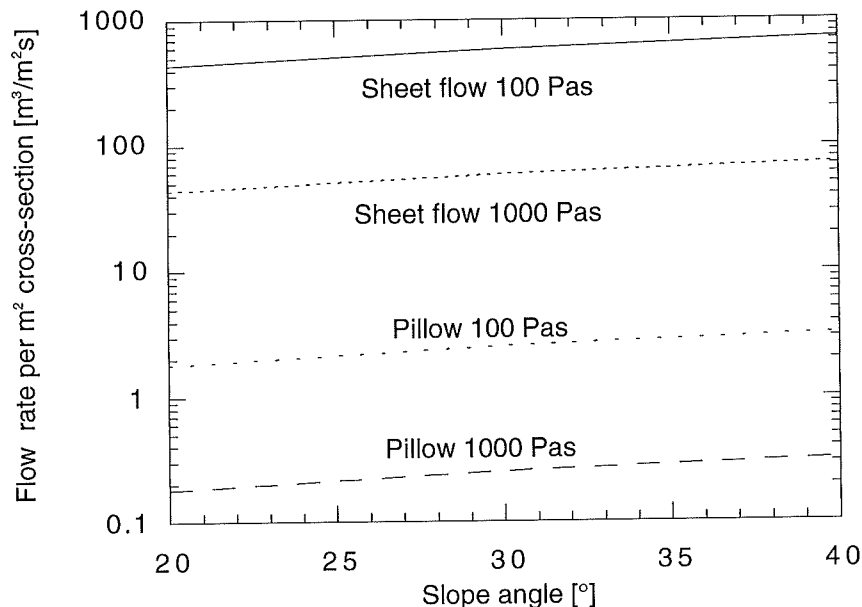


**Fig. 26** Dependency of the mean flow rate per square meter cross-section of the slope angle and the viscosity for a pillow (2D: 1 m diameter) and a sheet flow (2D: 10 m diameter).

### 11.3 The release of latent heat during solidification

Latent heat is released when crystallization takes place. No latent heat is liberated by the formation of glass. As a first approximation the latent heat is released uniformly at temperatures between the solidus and the liquidus so that its effect is equivalent to replacing the specific heat of the lava by [Jaeger, 1968]

$$c' = c + L / (T_l - T_s) \quad (51)$$

where  $c$  = Heat capacity [ $\text{J kg}^{-1} \text{K}^{-1}$ ],  
 $L$  = Latent heat of solidification or melting [ $\text{J kg}^{-1}$ ],  
 $T_l$  = Temperature at the liquidus [K],  
 $T_s$  = Temperature at the solidus [K].

Figure 27 shows the heat loss of a single stationary pillow with a diameter of 1 m over 11 days, with and without release of latent heat. The curve without latent heat displays the theoretical, exponentially decaying relation, whereas the curve including latent heat of crystallization possesses two distinct branches; an upper section where the latent heat of crystallization retards the cooling process and a lower section, where the entire pillow is below the solidus temperature and cooling proceeds in the exponentially decaying fashion. The release of latent heat significantly retards the cooling of a stationary pillow.

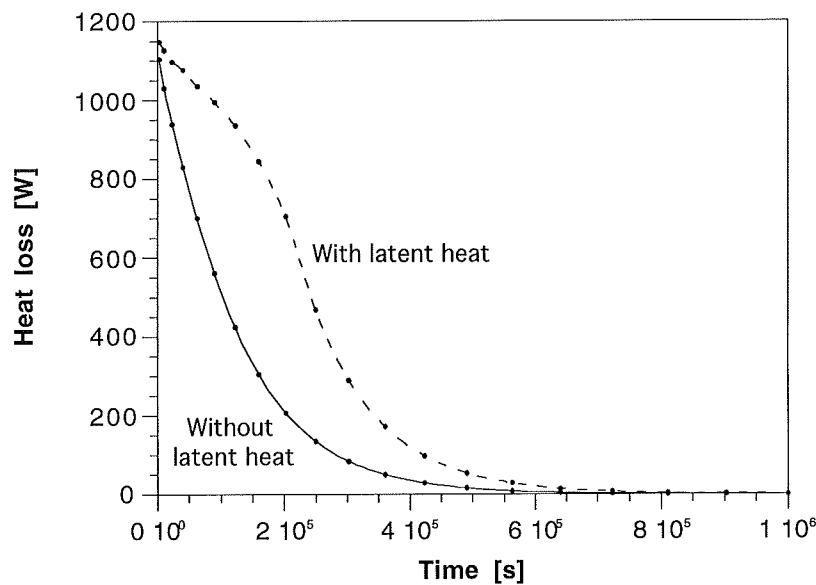


**Fig. 27** Heat loss of a single pillow during 11 days ( $10^6$  s); (a) calculated excluding latent heat of crystallization; (b) including latent heat.



In the model calculations the specific heat is adjusted to account for different rates of crystallization and formation of glass by assigning different specific heat capacities to the supersolidus and subsolidus parts of the flow.

#### 11.4 The effect of viscous heating

Heating by viscous dissipation occurs in all fluids. When the fluid viscosity is strongly temperature dependent, thermal runaway may occur, in which viscous heating reduces fluid viscosity and triggers faster shearing, resulting in still higher rates of heat generation [Fuji and Uyeda, 1974; Hardee and Larson, 1977; Hardee, 1993]. In the following section the question whether thermal runaway can occur in flowing basaltic lava will be analyzed theoretically and a test model including high velocities and therefore high rates of viscous heating will be discussed.

To derive a theoretical expression for the viscous heating for one-dimensional plane, laminar flow, while neglecting inertial terms, the equation for conservation of energy can be written (see eq. (35)) as

$$\rho c (\partial T / \partial t) = \lambda \left( \frac{\partial^2 T}{\partial y^2} \right) + (\tau u) \quad (52)$$

The local dissipation rate  $\Phi$ , which is a measure of the viscous heating, is the product of the shear stress in the direction of the flow  $\tau$  and the velocity gradient  $u$ . These are related by Newton's law

$$\tau = \eta u \quad (53)$$

For Poiseuille flow of an incompressible liquid, the local stress depends on the local radius according to the equation [Turcotte and Schubert, 1982]

$$\tau = (P/2) r \quad (54)$$

where  $P$  is a constant pressure gradient [ $\text{Pam}^{-1}$ ].

In view of the cylindrical symmetry, the heat conduction term can be expressed as

$$(\lambda/r) (\partial T / \partial r) + \lambda \left( \frac{d^2 T}{dr^2} \right) \quad (55)$$

With the temperature dependence

$$\eta = \eta_0 e^{-a(T-T_0)} \quad (56)$$

where  $\eta_0$  is the viscosity at a reference temperature  $T_0$  and  $a$  is an appropriate constant the energy equation can be rewritten

$$(P^2/4\eta_0) r^2 e^{a(T-T_0)} = \rho c (\partial T/\partial t) - \lambda \left( (1/r) (\partial T/\partial r) + \left( \frac{d^2 T}{dr^2} \right) \right) \quad (57)$$

The substitutions

$$\Phi = a(T - T_0) \quad , \quad \xi = r/R \quad , \quad \tau = (\lambda/\rho c R^2) t \quad (58)$$

lead to the single parameter equation [Gruntfest et al, 1964]

$$Br' \xi^2 e^\Phi = (\partial \Phi / \partial \tau) - (1/\xi) \left( \frac{\partial^2 \Phi}{\partial \xi^2} \right) \quad (59)$$

in which  $Br' = aR^4 P^2 / 4\lambda \eta_0$ .

$Br' \xi^2$  is identical with the Gruntfest or Brinkman-number  $Br$  in Gruntfest [1963]. A different definition of the Brinkman number is  $Br = \eta V^2 / \lambda \Delta T$ , which is a measure of the extent to which viscous heating is important relative to the heat flow resulting from the temperature difference. The space variable can be separated now to allow for the radial variation of stress. Gruntfest et al [1964] solve the equation numerically and find that Brinkman numbers  $>8$  lead to a thermally unstable solution, in which thermal runaway occurs. Kearsley [1962] gives analytical solutions for the differential equation.

For olivine tholeiite (see Figure 12):

$$\eta_0 = 11.051 \text{ Pa s},$$

$$a = 0.01419 \text{ J m}^{-3} \text{ K}^{-1}.$$

which leads to a Brinkman number of 0.3 for lava at a temperature of 1473 K and a radius of 0.5 m. The more viscous lavas lead to even lower Brinkman numbers (tholeiite = 0.02). Thermal runaway will not occur at these low Brinkman numbers in tholeiitic lava.

Solving equation (59) for the largest stable radius of a pipe leads to a radius of 2 meters. Olivine tholeiitic lava flowing in a pipe with a radius greater than 2 m at a constant pressure gradient of  $200 \text{ Pa m}^{-1}$  may develop a thermal runaway and produce more heat. The highest flow velocity at this pressure gradient would be  $12 \text{ m s}^{-1}$ , which is unrealistic for lava flows.

To confirm the theoretical analysis, model runs with higher Brinkman numbers were performed. For simplicity, no cooling was included in these runs. The cooling

counteracts the viscous heating in nature, especially the very effective cooling through the seawater. The temperature distribution of a model run with a pressure drop of  $500 \text{ Pa m}^{-1}$  is presented in Figure 28. The rise in temperature occurs in the outer part of the tube where the gradient of the flow velocities is largest. Figure 29 shows the dependency of the highest temperature on the pressure drop in the tube, which determines the flow velocity. Both models with a temperature dependent viscosity and with a constant viscosity were calculated. The viscous heating is increased by the decrease of viscosity and the resulting higher flow velocities. The pressure interval, in which the pillow models are calculated is underlain in gray. In this interval the viscous heating does not exceed one Kelvin. Also shown in Figure 29 is the dependency of the highest occurring temperature on the Brinkman number. It confirms the calculations of Gruntfest et al [1964] who find that at Brinkman numbers larger than 8, viscous heating is not negligible. The Brinkman numbers in the model run presented in this thesis are  $<0.3$  and thus no viscous heating will occur.

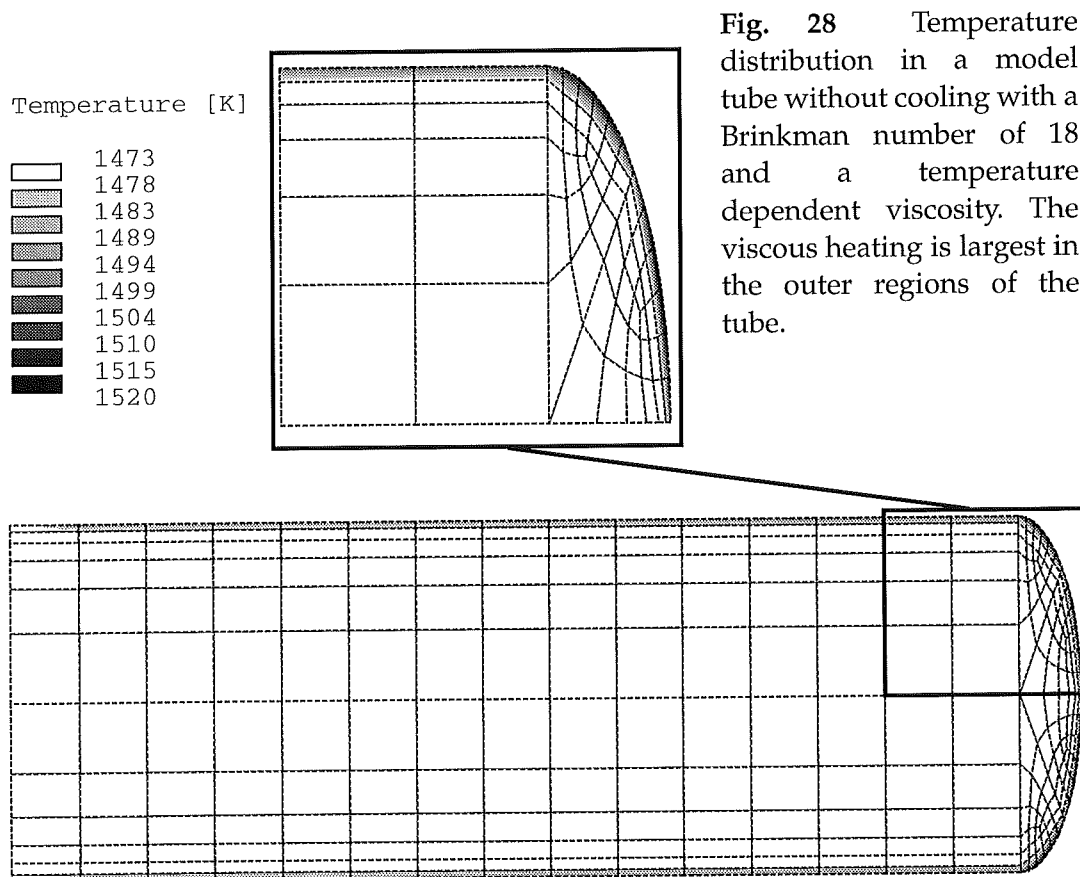


**Fig. 28** Temperature distribution in a model tube without cooling with a Brinkman number of 18 and a temperature dependent viscosity. The viscous heating is largest in the outer regions of the tube.

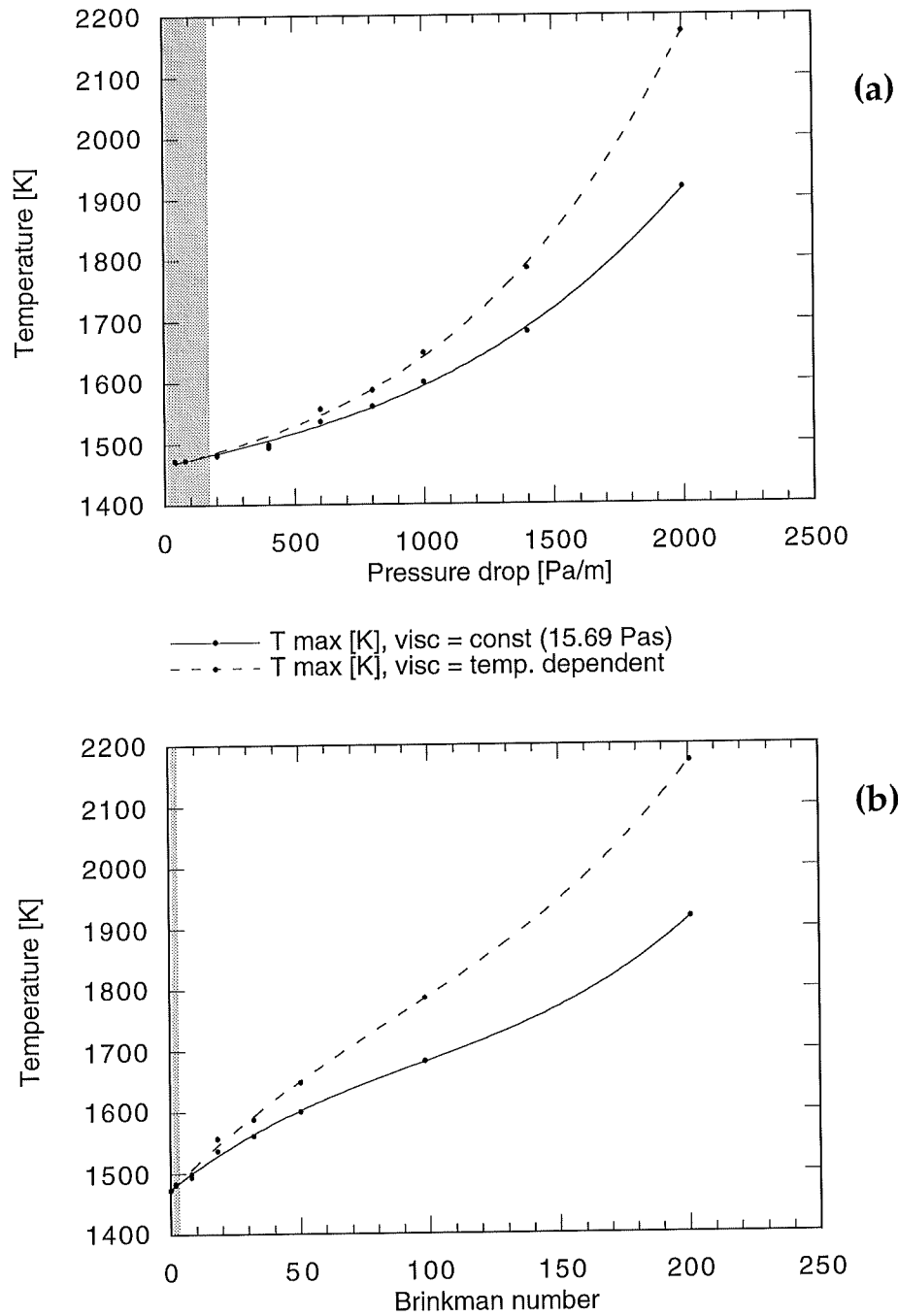


**Fig. 29** (a) Pressure dependency of the highest occurring temperature in the tube in a simple model without cooling. The viscous heating effect is reinforced by the decrease in viscosity and the resulting higher velocities in the model run with a temperature dependent viscosity. The constant viscosity and the viscosity at 1473 K in the temperature dependent model are 15.69 Pas.

(b) Dependency of the highest occurring temperature on the Brinkman number. The range of the model runs of this thesis are shaded in gray. The temperature rise due to viscous heating does not exceed one Kelvin in this interval.

### 11.5 Influence of the different density functions

Some model calculations were performed using the different density functions of Figure 16 as input parameters. The density of lava was calculated for the five different compositions shown in Table 1 with the density changes due to thermal expansion incorporated. The densities in the models range from  $2670 \text{ kg m}^{-3}$  for tholeiite at 1473 K and  $2888 \text{ kg m}^{-3}$  for picritic basalt at 1300 K. The results of the model calculations showed no significant influence of the density on the flow rates and temperature distributions in the model. The cooled lava can sink to the bottom of the tube (Figure 30) only at low flow rates, which may lead to the asymmetric pillow cooling patterns as observed in pillows by Yamagishi et al [1989]. Even though the influence of the temperature dependency of the density is not large, it was incorporated into the modeling to obtain more accurate temperature profiles at low flow rates prior to flow cessation. Changes in density due to the settling of phenocrysts in the melt were not included, since the settling velocities of crystals in the melt are small compared to the flow velocities of the lava, as can be seen from the following assessment:

Stokes law for the settling velocity of a single spherical particle [Cox et al, 1979] can be expressed as

$$V_t = \frac{2gr^2(\Delta\rho)}{9\eta} \quad (60)$$

with  $V_t$  = Terminal velocity [ $\text{ms}^{-1}$ ]  
 $r$  = Particle radius [m]  
 $\Delta\rho$  = Density contrast between particle and fluid medium  
 $g$  = Gravitational acceleration [ $\text{m s}^{-2}$ ].

Using the above equation, the terminal velocity of an olivine crystal with a density of  $3200 \text{ kg m}^{-3}$ , in a fluid of  $2800 \text{ kg m}^{-3}$ , and a radius of 1 mm, will reach  $8.7 \cdot 10^{-6} \text{ m s}^{-1}$ . The flow velocities in the following models are much higher than the settling velocity of the crystals.

The density of glass of albite composition quenched at different pressures has been determined by Kushiro [1980]. It increases with increasing pressure of quenching from  $2380 \text{ kg m}^{-3}$  at  $1.013 \cdot 10^4 \text{ Pa}$  (1 atm) to  $2525 \text{ kg m}^{-3}$  at  $25 \cdot 10^8 \text{ Pa}$ . This effect is also small for and thus not included into the modeling.

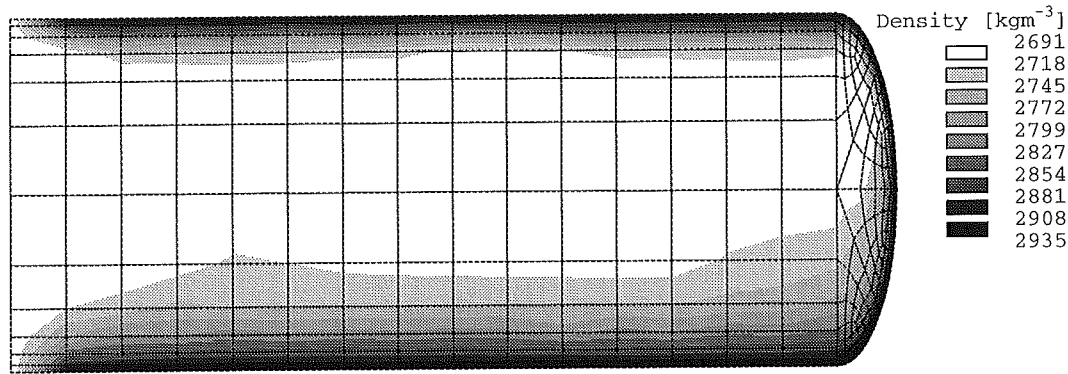


**Fig. 30** Density distribution in a model run with a low flow velocity (max.  $0.04 \text{ ms}^{-1}$ ). The cooler, denser material can sink to the bottom of the tube.

### 11.6 Cooling of the pillow

Convective cooling through the seawater is expected to be the dominant mechanism for heat loss from lavas erupted underwater. The radiative heat flux given by Stefans law is only about 1/30 of the convective heat flux in submarine environments [Griffiths and Fink, 1992b], and is therefore omitted. However, it is the most important mechanism of heat loss in subaerial environments [Dragoni, 1989; Crisp and Baloga, 1990]. First, convective cooling is described mathematically and then a possible exeption pertaining to insulation by vapor is discussed. The different types of thermal energy transport in the models and their implementation in the finite element program are presented. The results of model calculations for a range of cooling functions follow.

The convective cooling is controlled by the dynamics of a thin unstable boundary layer in the water, and by conduction through a boundary layer in the lava [Griffiths and Fink, 1992a]. The convective heat flux  $F_c$  in the water at large Rayleigh numbers, with small temperature differences and no boiling [Griffiths and Fink, 1992a] is

$$F_c = J(T_c - T_a)^{4/3} \quad J = \rho_a c_a \gamma (g \alpha_a \kappa_a^2 / \nu_a)^{1/3} \quad (61)$$

where  $T_c$  = Lava temperature at contact surface,

$T_a$  = Adopted temperature of seawater,

$c_a$  = Heat capacity of seawater,

$\rho_a$  = Density of seawater,

$\gamma$  = Empirical constant close to 0.1,

$\kappa_a$  = Thermal diffusivity of water [ $\text{m}^2 \text{ s}^{-1}$ ],

$\nu_a$  = Kinematic viscosity of seawater [ $\text{m}^2 \text{ s}^{-1}$ ],

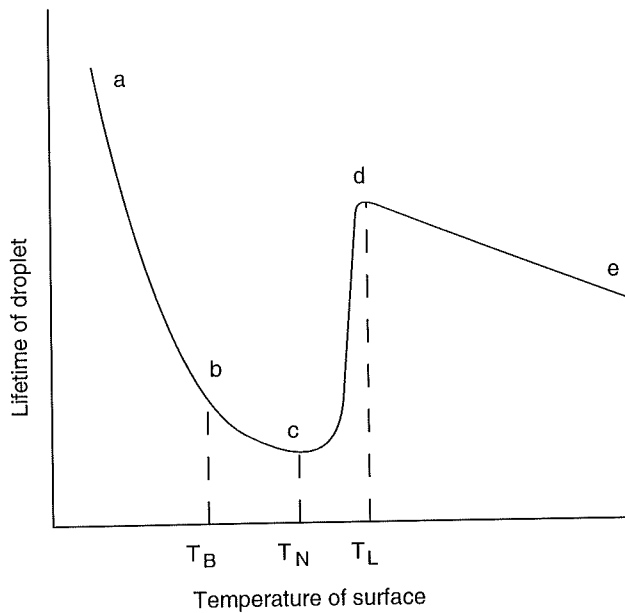


**Fig. 31** The generalized boiling curve. The lifetime of a droplet on a hot stove depends strongly on the temperature of the stove. At point  $T_B$  the boiling point is reached and gas bubbles begin to nucleate. At point  $T_N$  (Nukiyama Temperature) is the shortest lifetime. Beyond this point the Leidenfrost effect sets in and the droplet is supported by a cushion of its own vapor. At the Leidenfrost Temperature  $T_L$  the cushion is fully developed. At even higher temperatures the evaporation increases again [after Mills, 1984].

Film boiling of water around the pillow can produce a thin insulating sheath of vapor, known as the Leidenfrost-effect [Mills, 1984]. This phenomenon explains the paradoxical observations of lava glowing for periods of up to 1.5 s under water and can be explained by considering the lifetime of a water droplet on a hot stove. The generalized boiling curve is shown in Figure 31 [Mills, 1984]. Below the boiling point  $T_B$ , the lifetime shortens at increasing temperature of the stove until the boiling point is reached and gas bubbles begin to nucleate. The shortest lifetime corresponds to point  $T_N$  (Nukiyama Temperature  $\approx 450$  K for water). Beyond this point the Leidenfrost effect sets in and the droplet is supported by a cushion of its own vapor. At the Leidenfrost Temperature  $T_L$  ( $\approx 500$  K for water) the cushion is fully developed, and at even higher temperatures evaporation increases again. Incandescent lava flowing into water is insulated by a sheath of vapor above 500 K. Once the lava surface temperature drops below  $T_N$  the lava is cooled by direct contact with the water. Only fresh cracks will expose incandescent lava and therefore in all models with a cooled outer rind, no allowance is made for the Leidenfrost effect.

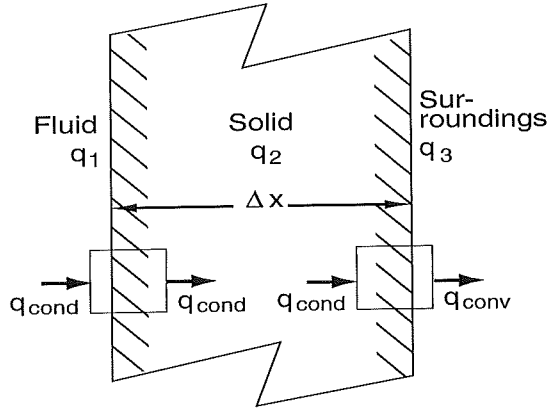


**Fig. 32** Schematic diagram showing conductive heat transfer across a fluid-solid interface ( $q_1$ ), conduction through the solid ( $q_2$ ), and convective heat transfer between the solid and surroundings ( $q_3$ ) as usually applied to conjugate heat transfer problems.

The heat loss of a pillow is controlled by the conductive heat transport through the crust and the convective heat loss through the water (Figure 32). The heat transfer through the three 'thermal resistance' intervals  $q_1$ ,  $q_2$ , and  $q_3$  is, respectively,

$$q_1 = -\lambda_f \left( \frac{dT}{dx} \right)_{w_1} \quad q_2 = -\lambda_w \frac{(T_{w_1} - T_{w_2})}{\Delta x} \quad q_3 = h_a (T_a - T_{w_2}) \quad (62)$$

where  $\lambda_f$  = Thermal conductivity of the fluid [ $\text{W m}^{-1} \text{K}^{-1}$ ],  
 $\lambda_w$  = Thermal conductivity of the wall [ $\text{W m}^{-1} \text{K}^{-1}$ ],  
 $T_{w1}$  = Temperature at the inner wall face [K],  
 $T_{w2}$  = Temperature at the outer wall face [K],  
 $q_1, q_2, q_3$  = Heat fluxes [ $\text{W m}^{-2}$ ],  
 $h_a$  = Film coefficient [ $\text{W m}^{-2} \text{K}^{-1}$ ].

In the model calculations,  $q_1$  and  $q_2$  were calculated by FLOTRAN, so the only boundary condition relates to  $q_3$ , which in turn depends on the film coefficient  $h_a$ . To properly calculate this quantity, the film coefficient and the temperature of the ambient water must be known.

Several model runs with different film coefficients in the upper and lower half of the model were performed to examine the effect of different cooling functions. If the pillow overlies sediments or older pillows and lava flows, the heat flux in the lower half will be mostly conductive and in the upper half convective. The different runs included a film coefficient on the upper half cylinder between 300 and 5000  $\text{W m}^{-2} \text{K}^{-1}$ , spanning the range of convective cooling through water [Anonymous, 1992]. The film coefficient on the lower half was successively 0, 10, 50, and 100% of the upper one. The ambient



temperature was chosen as 300 K since the water in the vicinity of a lava flow entering the sea is not significantly heated as has been documented by divers at Kilauea, Hawaii [Tribble, 1991].

The different thermal energy transport modes are illustrated in Figure 33. Advection of the fluid brings new thermal energy into the system. Most of the energy leaves the system with the fluid at the outlet, while only a small portion is transported conductively to the wall faces. This portion is transported further convectively into the seawater. Figure 34, shows the resulting temperature distributions along the central section and a cross section at the outlet of a 2.5 m long tube, cooled with a film coefficient of 5000 and 300  $\text{W m}^{-2} \text{K}^{-1}$  respectively, on the upper half cylinder. In both cases, the film coefficient on the lower half is 10% of the upper half (500 and 30). There is a notable temperature difference between the upper and lower tube boundaries in model (b), whereas in model (a) the whole outer boundary is cooled to the ambient temperature within the 0.25 m closest to the inlet, while heat loss further down the tube is controlled by the supply of thermal energy through the outermost layer of flowing lava.

Figure 35 shows the resulting energy flow to the wall face and the total energy flow in the model for different film coefficients. Heat transfer to the wall increases linearly with increasing film coefficients, as would be expected. The total energy flow, which includes the advectively transported heat in the fluid and the conductively transported heat flow to the wall face, does not increase at film coefficients above 1000  $\text{W m}^{-2} \text{K}^{-1}$ .

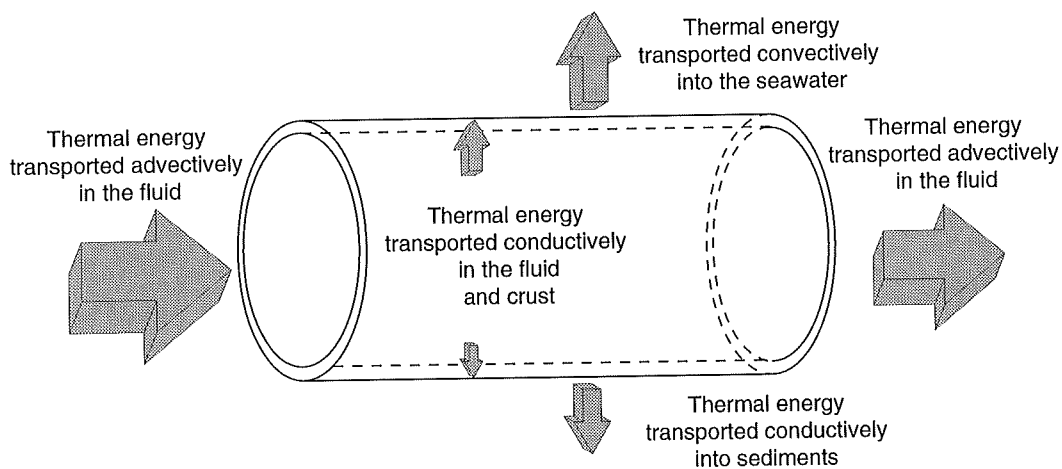
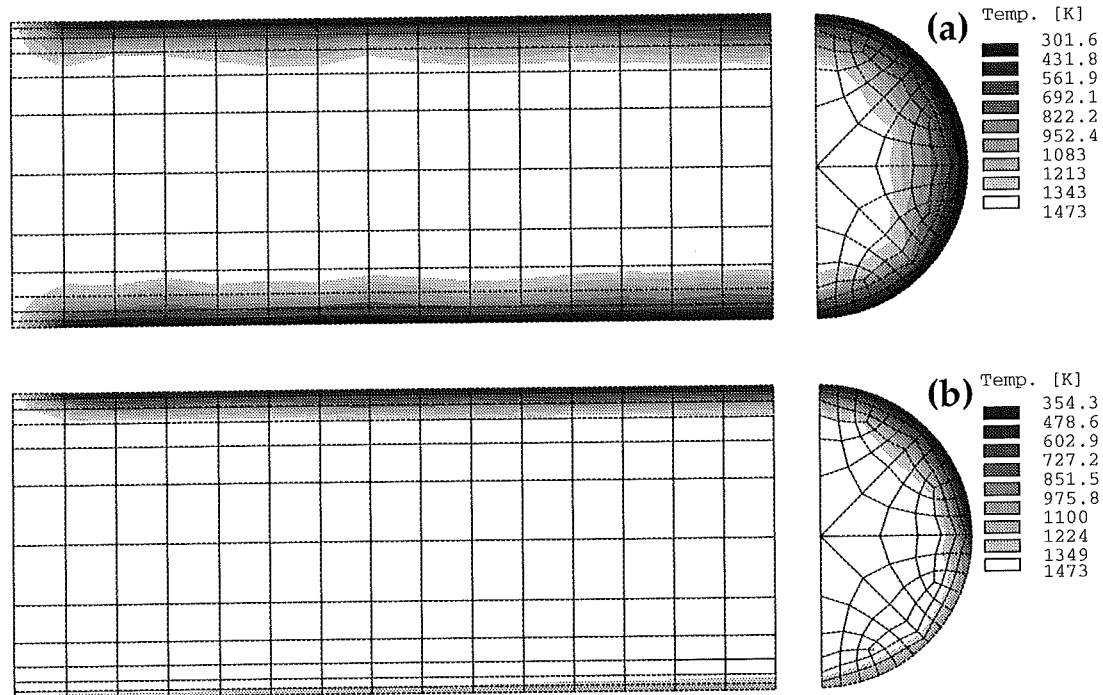


Fig. 33 Schematic diagram of the thermal energy budget in the model.

Since the solidified outer rind is rapidly cooled down to seawater temperature in all cases with film coefficients greater than  $1000 \text{ W m}^{-2} \text{ K}^{-1}$ , the temperature field does not change significantly for even higher film coefficients. Meanwhile, the temperature field controls the viscosity, which in turn governs the flow velocities and thus the advective heat transport. Because the advective contribution is 100 times larger than the conduction at the outer boundary, the total energy flow is influenced almost exclusively by the viscosity.

The lowest temperature in all model runs with a film coefficient above  $300 \text{ W m}^{-2} \text{ K}^{-1}$  is nearly constant, namely 303 K, the ambient temperature. In most of the model calculations, a film coefficient of  $4000 \text{ W m}^{-2} \text{ K}^{-1}$  on the upper half and  $400 \text{ W m}^{-2} \text{ K}^{-1}$  on the lower half cylinder was chosen. These are the mean of the range of values found in literature [Anonymous, 1992].



**Fig. 34** Temperature distribution along the central section and a cross section at the outlet of a 2.5 m long tube, cooled with a film coefficient of 5000 and 300  $\text{W m}^{-2} \text{ K}^{-1}$  respectively, on the upper half cylinder. In both cases, the film coefficient on the lower half is 10% of that of the upper half (500 and 30).

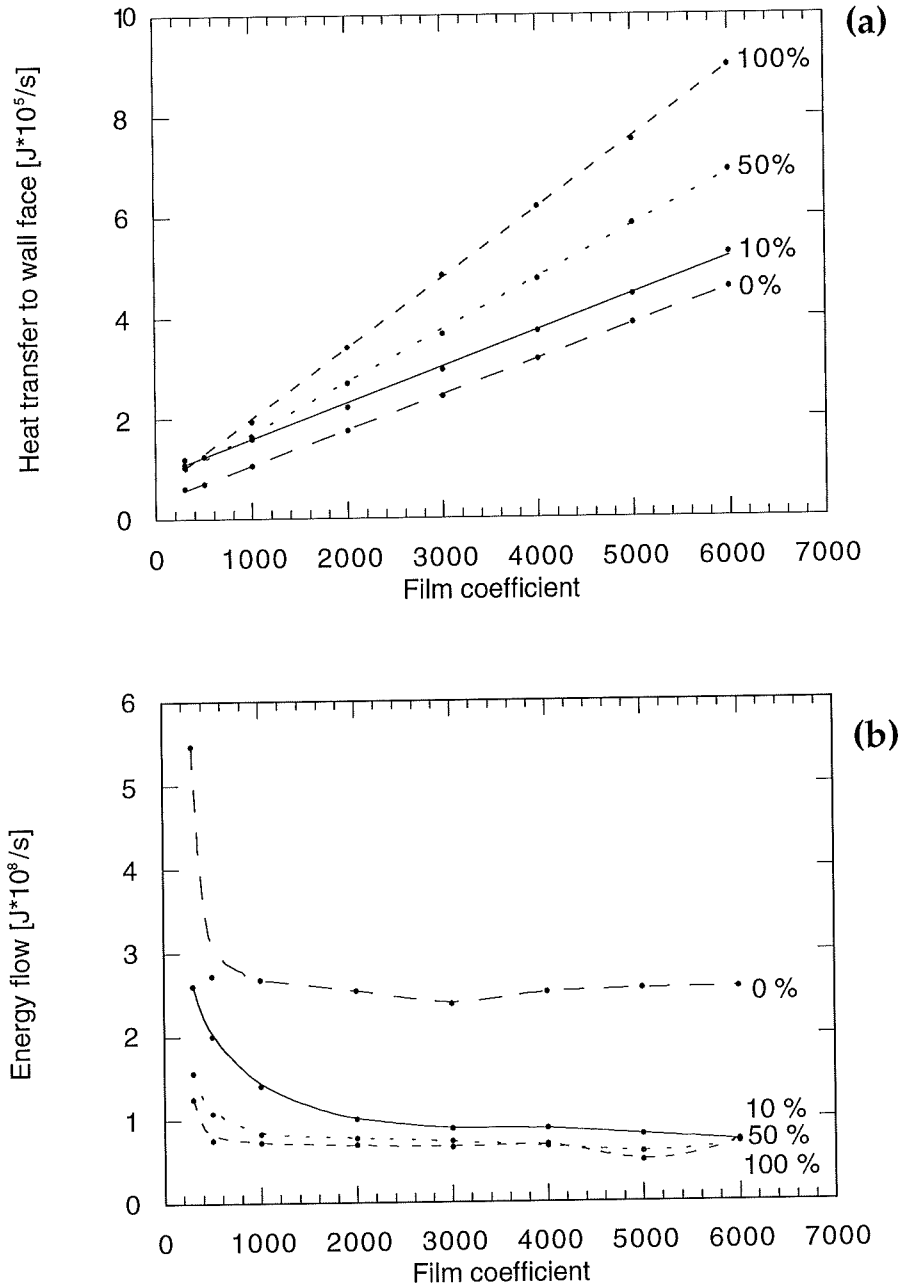


Fig. 35 (a) Heat transfer to the wall face for different film coefficients. The cooling on the lower half of the pillow is 0, 10, 50 and 100% of the cooling on the upper half. (b) Total energy flow in the model for different film coefficients and different ratios of cooling of the upper and lower half of the pillow

## 12 Numerical solutions: Complex models

To investigate the coupling of the different parameters, some complex model runs were performed. To analyze the reasons for deviation from the cylindrical shape of a pillow the aspect ratio was varied in subchapter (12.1), time dependent model runs are treated in subchapter (12.2). The influence of the inflow pressure function and inflow temperature are investigated in subchapters (12.3) and (12.4), and subchapter (12.5) describes the critical pressure, which is needed to keep the tube from freezing shut.

### 12.1 The aspect ratio

Most pillows in outcrops exhibit a characteristic aspect ratio (height to width relation) between 1 and 0.4. The deviation from the tube form is due to body forces (gravity and buoyancy), which act on the broken crust of the pillow. Geological observations of non-cylindrical pillows and speculations as to their cause are listed. Model calculations over a range of aspect ratios are presented to test these hypotheses.

Moore et al [1971] noted that on slopes steeper than  $30^\circ$  pillows are mostly cylindrical and exhibit a smooth surface, due to a reduced component of the gravity normal to the slope, which causes the flattening. Furnes and Fridleifsson [1978] demonstrated that alkaline olivine basalt pillows are more flattened and have a more limited size range than olivine tholeiite pillows. They suggested this effect might be due to higher viscosities in the olivine tholeiite. Axial dimensions, glass thickness and plunges of 822 Icelandic pillows of olivine tholeiitic to andesitic compositions were measured by Fridleifsson et al [1982]. They found that for smaller pillows the aspect ratio is nearly one, while larger pillows display smaller aspect ratios, supporting Moore et al [1971]. Also, the average, the maximum and the minimum diameters varied with the chemical composition. They considered three possible causes: magma viscosity, mineralogy, and degassing during growth.

Pillow volcanoes of the Troodos ophiolite, Cyprus, were investigated by Schmincke and Bednarz [1990]. They proposed the eruption rate as the primary control on the pillow size. The pillows showed highly variable shapes from circular to flat depending on the local topography. Walker [1992] made measurements of the horizontal and vertical dimensions of pillows in 19 locations and found a linear relationship in the

aspect ratio of the pillows and a dependency of the cross-sectional area of a pillow and the viscosity of the lava.

In an attempt to answer the question, why pillows are tubular and which factors control the deviation from the cylindrical shape, model runs with different aspect ratios were performed. Figure 36 shows the element distribution for aspect ratios between 1.1 and 0.4, the range spanning the geometry of most known pillows.

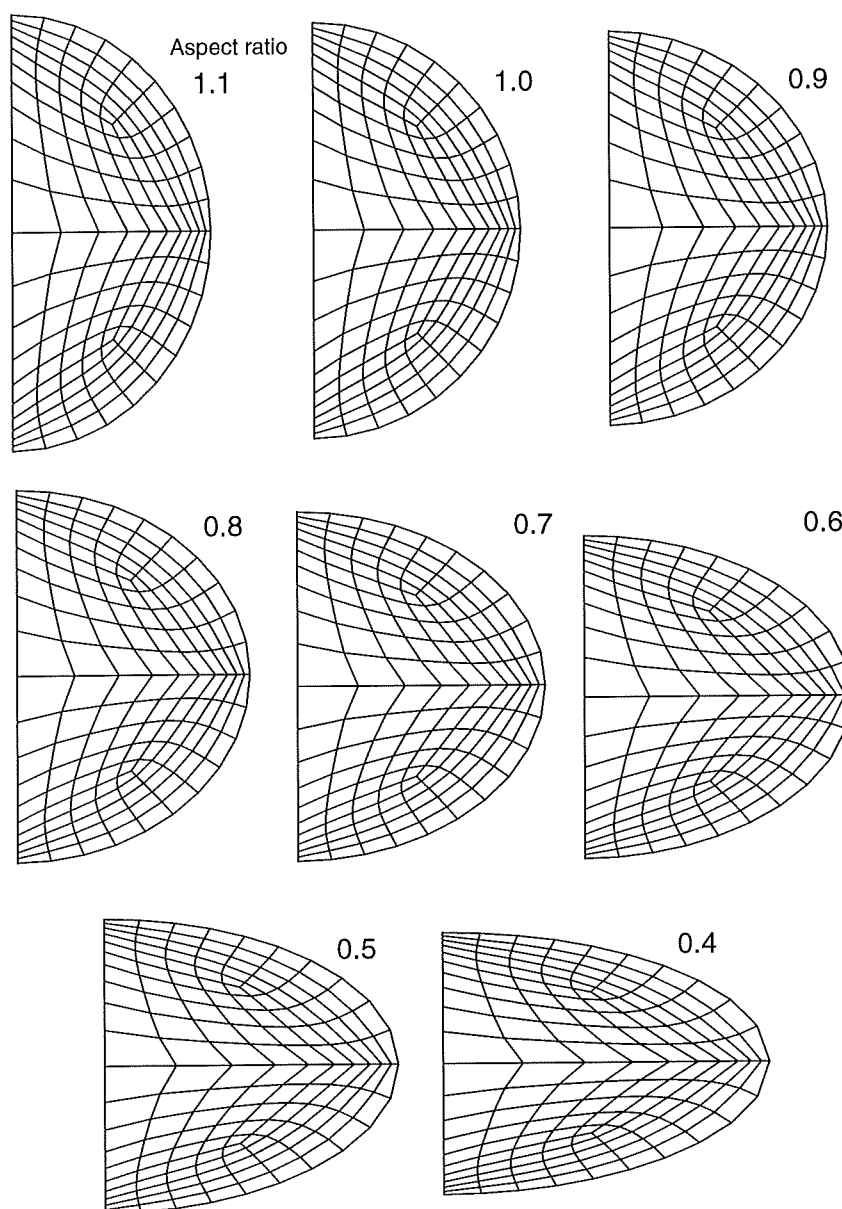


**Fig. 36** Element distributions of models with different aspect ratios. The number of elements is 1500, slightly higher than in the standard model, to prevent the generation of highly elongated elements.

To provide a better fit and to prevent the generation of highly elongated elements, the number of elements was chosen to be 1500, slightly higher than in the standard model. Table 4 shows the aspect ratio and the ratio of the cross-sectional area to the circumference for the different models. The cross-sectional area is constant at  $0.79 \text{ m}^2$ . The cylindrical model (aspect ratio = 1) leads to the largest cross-section to circumference ratio, and since effective cooling depends strongly on that ratio it is the most efficient way to transport lava while minimizing thermal energy loss.

**TABLE 4.** Aspect ratios and the ratios of the cross-sectional area to the circumference for the different models.

Model no.	Aspect ratio	Cross-section/ circumference
1	1.1	0.2499
2	1	0.2500
3	0.9	0.2495
4	0.8	0.2484
5	0.7	0.2464
6	0.6	0.2419
7	0.5	0.2359
8	0.4	0.2258

Figure 37 shows the thermal energy loss and the total energy flow for different aspect ratios. The maximum transported energy and the minimum heat lost through cooling occur at an aspect ratio of 1, the perfectly cylindrical tube. The flow maximum also occurs at the aspect ratio of one, due to the smallest frictional drag at the tube walls and the lowest viscosity inside the tube, because of the less effective cooling. Without the influences of the gravitational force and the local topography, pillows would tend to be cylindrical. The viscosity can only influence the aspect ratio of a pillow if it leads to the formation of pillows with a larger diameter, where the influence of the gravitational force is larger, since they take a longer time to build a sufficiently stable crust for a given volume of lava.

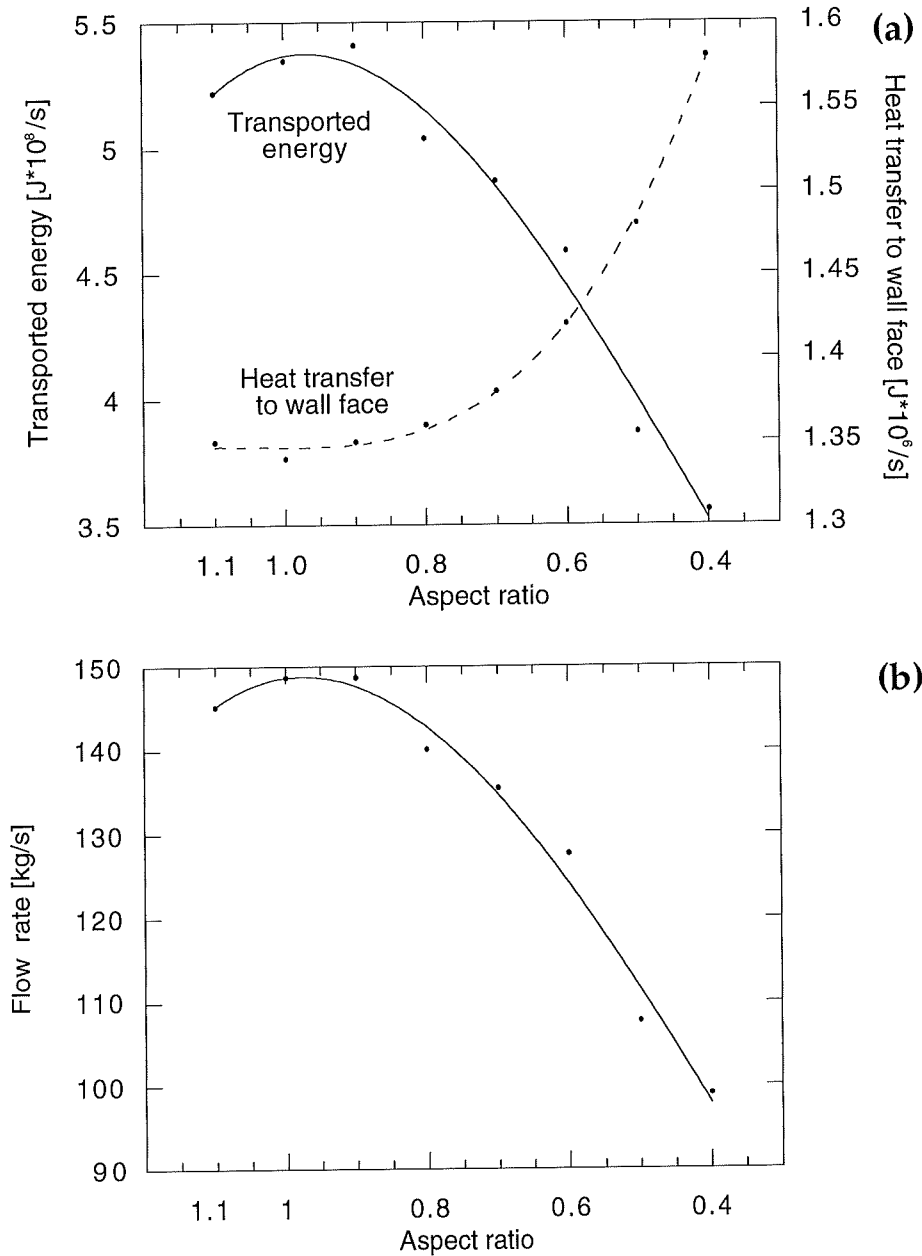


**Fig. 37** (a) Thermal energy loss and total energy flow for different aspect ratios. The maximum transported energy and the minimum heat loss through cooling occur at aspect ratio 1, the perfectly cylindrical tube.

(b) Flow rate for different aspect ratios. The maximum occurs at an aspect ratio 1, due to the smallest frictional drag at the tube walls and the lowest viscosity inside the tube, because of the most effective insulation.

Solid and broken curves are polynomial fits to calculated data points

## 12.2 Time dependent model runs

In order to investigate the interplay of the different parameters of the model, a few longer model runs were made. These included up to 2500 time steps with up to 20 different pressures. The runs were limited by the large calculation times, one pressure step requiring between 3000 and 10000 CPU seconds.

It was assumed that the pressure gradient in a pillow will drop over time, because the main flow often overrides the pillow and most of the material transport occurs in the main flow or in new pillows which build above the older ones [see Figure 3]. The flow rates decrease and cooling sets in, which further restricts the flow rate in the pillow. Based on direct submarine investigations including videos, the typical life span of a pillow is estimated to lie between 1/2 and a full hour. After that time, flow ceases and the pillow cools and solidifies. Magma transport is relocalized in the overlying pillows and sheet flows. For modeling purposes, a decaying exponential function was chosen for the input pressure leading to decreasing pressure gradients inside the tube as shown in Figure 38. A more detailed discussion of the input pressure function is given in chapter 12.3. Most time dependent models included 10-20 input pressure steps. During all model runs, the mean temperature, the bulk outflow temperature, the flow rates, and the density and viscosity distributions were calculated and plotted.

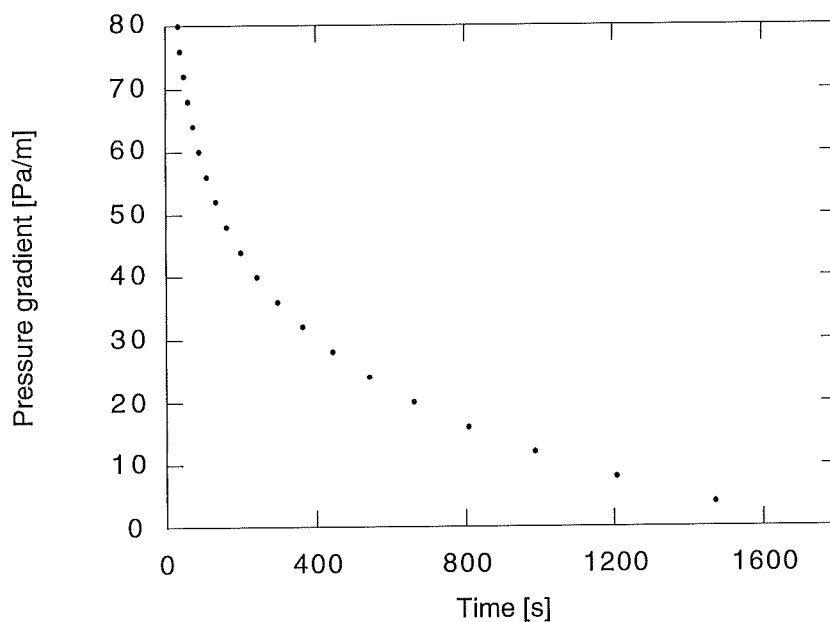


**Fig. 38** Pressure decrease of a time dependent model run. The pressure gradient in the tube drops from 80 Pa/m to 0 Pa/m in 30 min.



The first models were run without the effect of latent heat release, which leads to a faster cooling rate. Figure 39 shows the resulting flow rates and outflow bulk temperature. The flow rates drop as the inlet pressure of the model is reduced. The outflow bulk- or mixing cup-temperature is the average temperature of the fluid leaving the tube. It also drops at lower flow rates, because the fluid remains longer in the tube and can be cooled more. At all step-like input pressure drops, the temperature decreases only very little. After the last pressure drop, when the temperature rapidly sinks, the tube freezes and flow stops. The tube requires a minimum critical pressure gradient to keep from solidifying, otherwise the amount of thermal energy brought in by the influx of hot lava is less than the amount of thermal energy lost at the outer boundaries and the tube solidifies. This phenomenon will be examined further in the following section.

The inflow and outflow rates are identical to within  $>0.7\%$ , indicating a good convergence of the solution. The reason for this difference is, that the temperature dependency of the density is included in the equation of continuity and neglected in the equation of motion.

A second model run included the effect of release of latent heat by changing the heat capacity when an element was cooled below the solidus. An average degree of crystallization 60-80% was assumed according to Moore [1965]. A release of  $5000 \text{ J kg}^{-1}$  over the temperature span between the liquidus and the solidus then leads to a heat capacity of  $2444 \text{ J kg}^{-1} \text{ K}^{-1}$  for the fluid and a heat capacity of  $720 \text{ J kg}^{-1} \text{ K}^{-1}$  for the solid elements. The resulting flow rates, outflow bulk temperature and the average temperature are shown in Figure 40. The bulk outflow temperature does not decrease as rapidly as in calculations without latent heat due to the larger heat capacity, but remains constant to within one degree. The average temperature of the solid drops from 1015 K to 960 K during this run, while the mean liquid temperature decreases from 1460 K to 1435 K. Up to 484 elements were cooled below the liquidus (see Table 5). After the first pressure step, the whole outer boundary is cooled down to seawater temperature, which simulates the rapid quenching of a glassy crust when lava extrudes into seawater. Additional fluid elements are selected at later time steps as cooling and solidification continue, whereby for lower flow velocities the solidification front progresses inward.

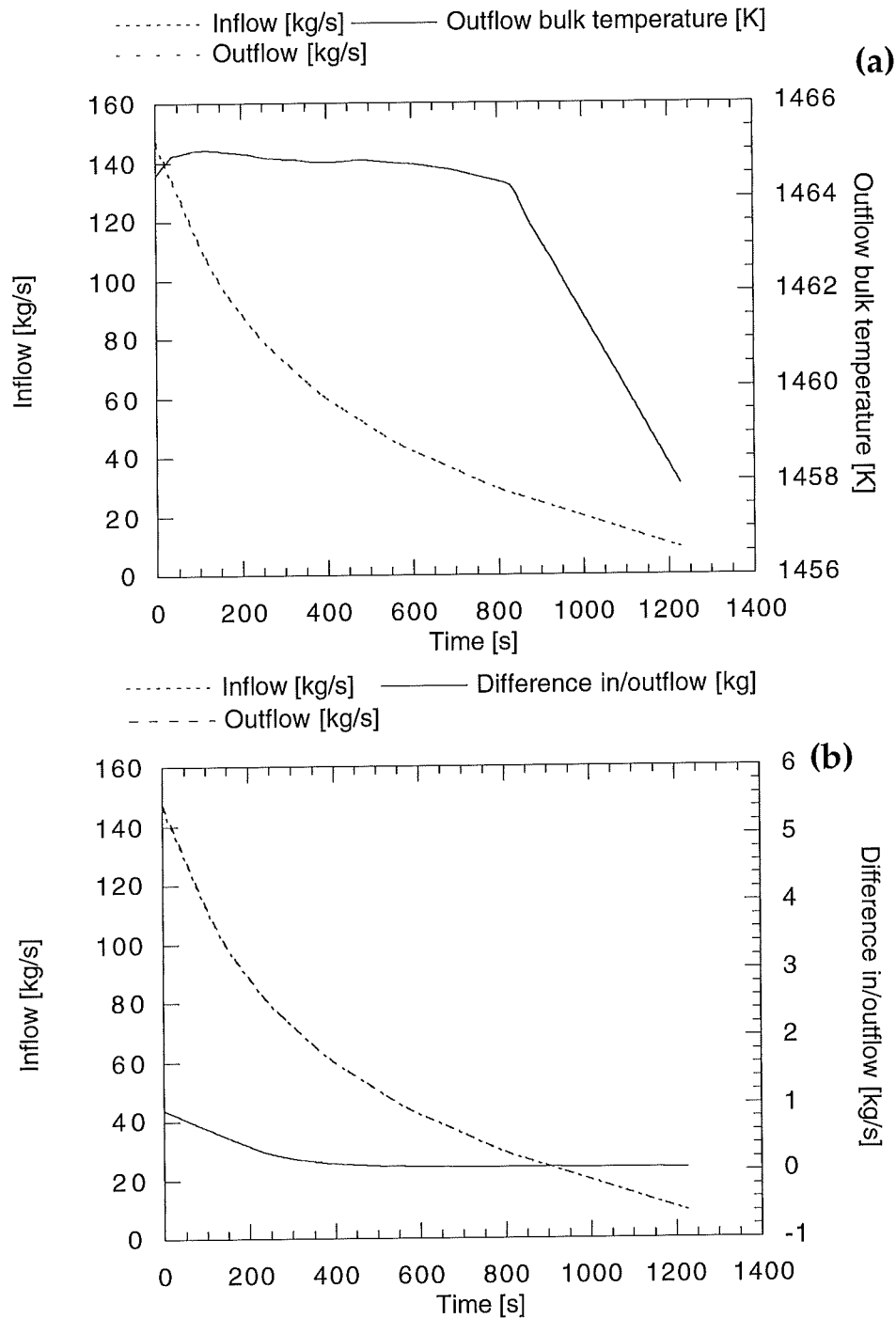


**Fig. 39** Flow rates and outflow bulk temperature of a simple model without the effect of latent heat.

(a) The flow rate drops as the inlet pressure of the model is reduced. The outflow bulk temperature also drops at lower flow rates, because the fluid remains longer in the tube and can be cooled more. After the last pressure drop, the temperature sinks rapidly, the tube solidifies and flow stops.

(b) The inflow and outflow rates are identical within  $>0.7\%$ . One reason is the low compressibility of the fluid, another the minute calculation errors.

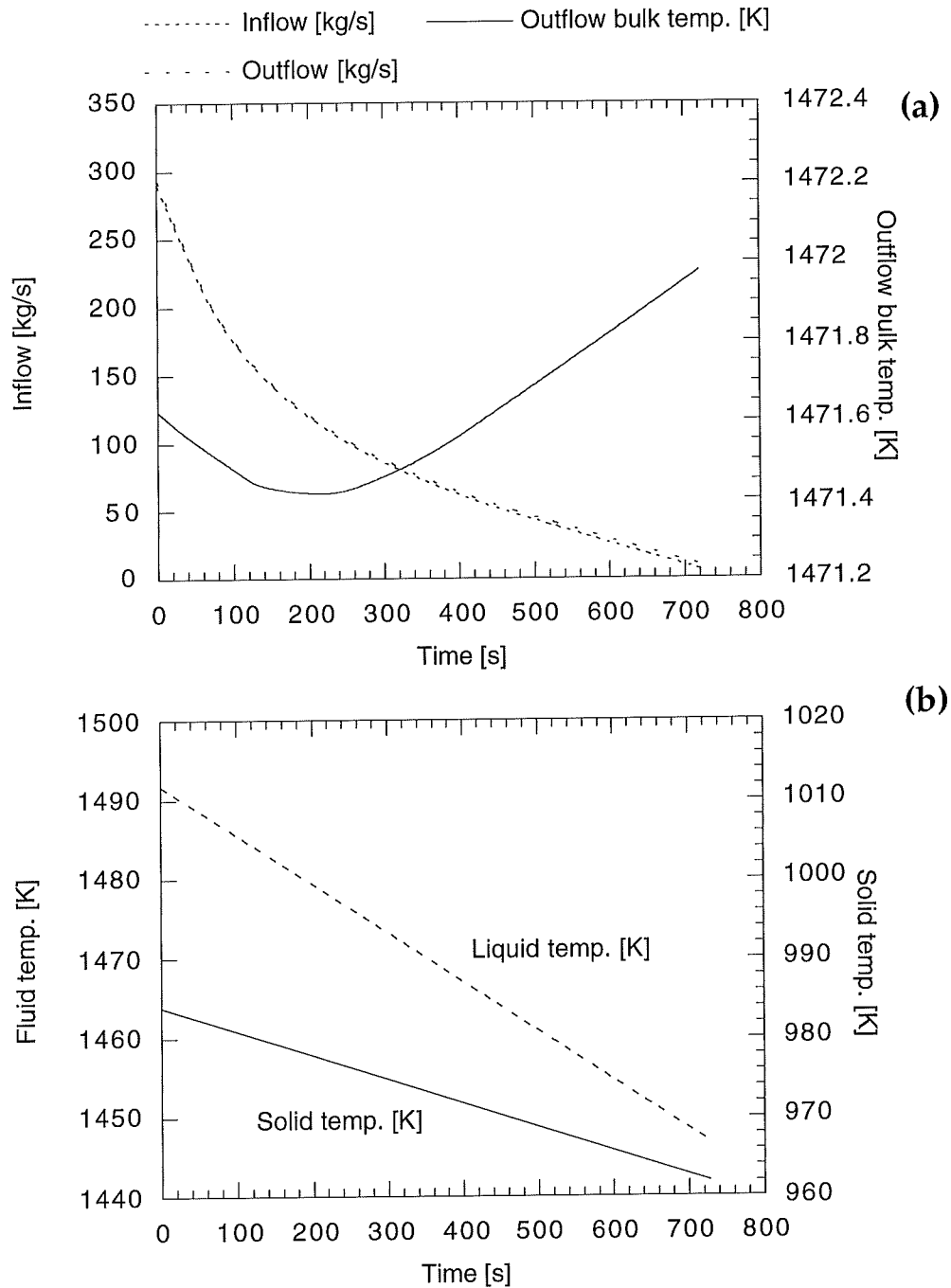


**Fig. 40** In- and outflow rates, bulk outflow temperature and the average solid and liquid temperatures of the model run.

(a) In- and outflow rates are nearly identical. The bulk outflow temperature does not decrease as rapidly as in calculations without latent heat due to the larger heat capacity

(b) The average temperature of the solid elements drops from 1015 K to 960 K during this run and that of the liquid elements from 1460 K to 1435 K.

**TABLE 5.** Number of selected elements during one model run.

Pressure step	No. of selected solid elements	Pressure step	No. of selected solid elements
1	0	10	310
2	279	11	329
3	279	12	354
4	283	13	427
5	285	14	456
6	287	15	478
7	389	16	480
8	297	17	484
9	304	18	484

To examine the cooling history of the different regions during a time dependent model run, the nodal temperatures of the three different zones of the model were plotted, instead of a mean or bulk temperature. The outermost rind (black ring) is cooled nearly to seawater temperature, while the inner part of the tube only cools very slightly, as already observed in the steady state modeling. In between those two parts is a zone (gray ring) which is rather hot at the beginning, but cools much faster than the rest of the fluid. Here solidification takes place, and the solid elements, with a lower heat capacity than the liquid ones, are cooled more rapidly than the fluid. The three regions found in the modeled temperatures can be correlated to three different textures found in pillows: the glassy rind, the intermediate zone of increasing degree of crystallization, and the microcrystalline core (see Figure 8).

The outer sheath insulates the inner fluid against seawater so that the fluid loses heat mainly through conduction. This is one reason why hot lava is able to flow in water over rather great distances, as observed by diving expeditions and with submersibles [Ballard et al, 1979; Moore, 1975].

Figure 42 displays the solid and liquid regions of the model tube at three different times during one run. (a) At 50 s when just the outermost crust has solidified, (b) at 500 s in the middle of the run when solidification advances and (c) at 1500 s or at the end of the run. At even lower input pressures, the whole tube will eventually close.

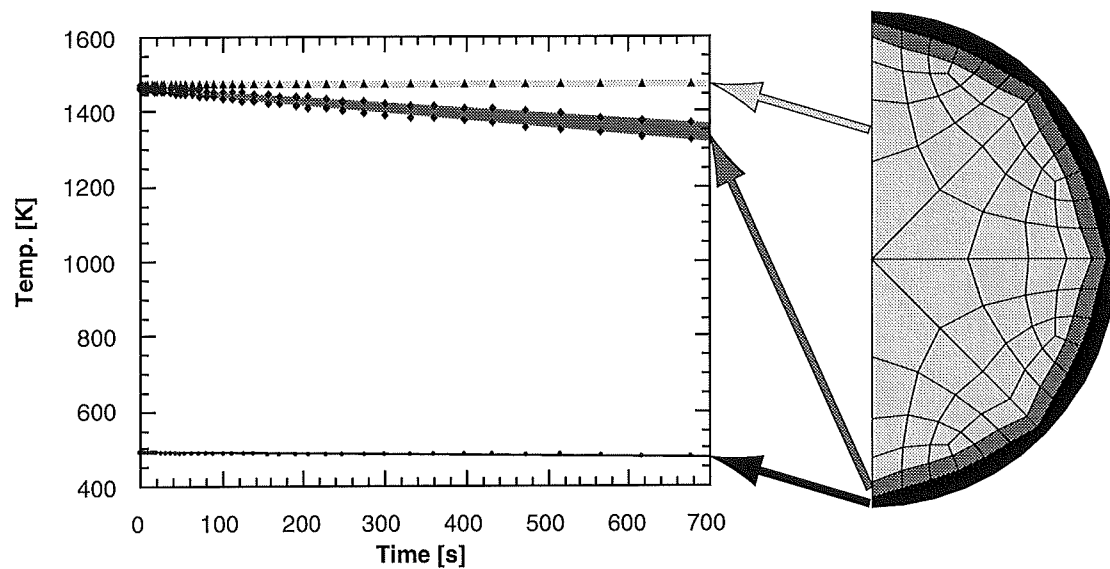


**Fig. 41** Nodal temperatures in the three different zones of the model. The outermost rind is cooled to seawater temperature, while the inner part of the tube only cools slightly. In between those two parts is a zone which is rather hot at the beginning, but cools much faster than the rest of the fluid. Here solidification takes place, and the solid elements, with a lower heat capacity are cooled much more rapidly than the fluid. These regions can be correlated to textures found in pillow outcrops: a glassy rind, an intermediate zone of increasing degree of crystallization, and a microcrystalline core (see Figure 8).

In conclusion, three different stages can be distinguished in the time dependent model runs, which can also be found in the active life span of a pillow lava. The first one is the rapid chilling of a glassy crust as simulated by the selection of the outer elements in the beginning of a run. The following stage is characterized by stable flow rates and a balance of inflow of thermal energy and thermal energy loss at the outer boundary. In the model, a steady state situation is reached at a constant entrance pressure. Cooling progresses only slowly, since the flow is insulated from the water. In the last stage, the driving pressure drops below a critical value, the flow loses more heat through conduction than is supplied by the inflow of hot magma into the tube, and flow ceases.

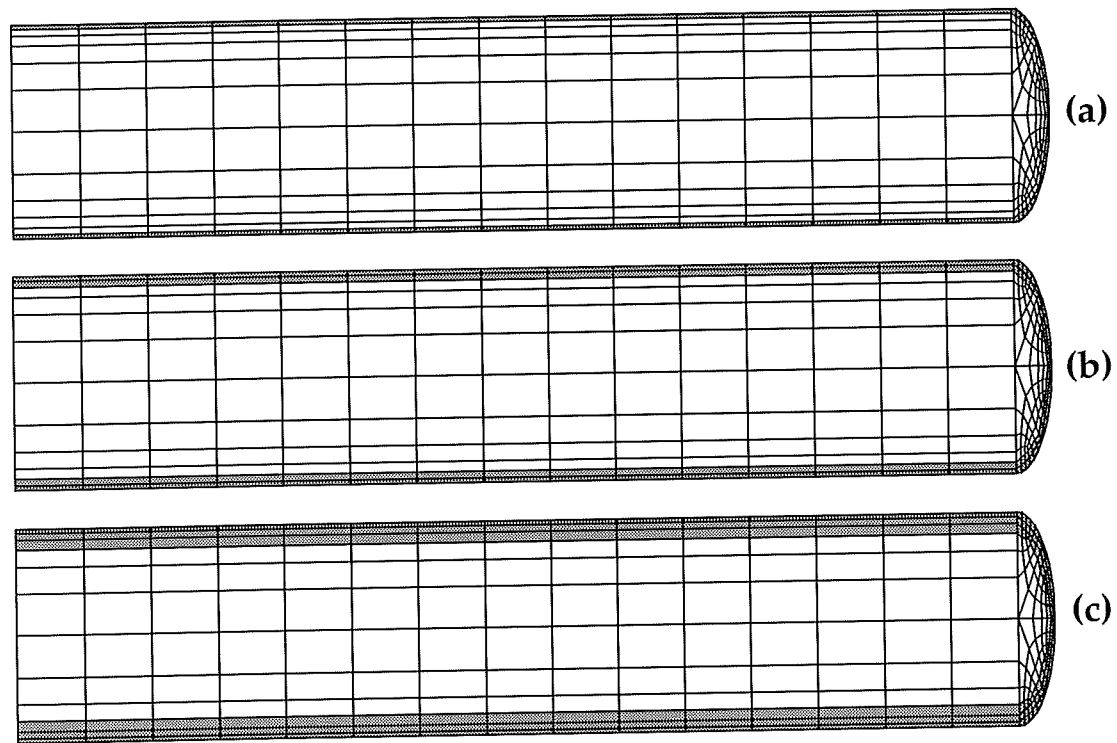


Fig. 42 Solid and fluid regions in the model tube during three different times ( $a = 30$ ,  $b = 500$ ,  $c = 1500$  s) of a time dependent model run.

### 12.3 Different input pressure functions

Since the variation of input pressure over time is an important parameter to represent the pressure reduction, which is difficult to measure in situ, three different functions were used: exponentially decaying, linearly decaying and a step function (Figure 43). The only indications in nature are observations from divers regarding the active life time of a pillow at the front of a flow [Moore, 1975; Tribble, 1991]. No measurements of flow rates have been undertaken, because of the difficult working circumstances: pillows observed at Kilauea, Hawaii, were often buried rapidly beneath rubble falling down the steep slope, divers can only remain under water for a limited period of time and instruments are difficult to transport and utilize. Normally, the pressure in the tube will drop because of different reasons: the eruption rate might cease, the lava might choose a different path through new feeder tubes or the supply might decrease because the lava is distributed to a larger network of pillows. Such a decrease of input pressure will normally occur gradually (exponential or linear function). Only if part of the flow breaks apart, as has been observed on steep slopes, might the supply be cut off suddenly (step function) [Tribble, 1991].

Since direct observational data are scarce, the function of the input pressure has also been chosen for modeling reasons. High flow rates lead to an increased demand for calculation time, since the time step is computed from the flow velocity. An incrementally small quantity of fluid cannot travel more than one element length in one time step in order to minimize the calculation error [Anonymous, 1992]. At high input pressures, the flow soon reaches a steady state. Only at low flow rates do temporal variations in flow occur, such as reduction and eventual ceasing of the flow. This is why the decaying exponential function has been chosen, leaving more time at lower flow rates than the linear function. Using a decaying function for the input pressure, the flow behavior can be observed over a spectrum of different flow rates, while using a step like function, it can only be observed at two different pressures.

However, as shown in Figure 43, the number of solidified elements does not depend strongly on the chosen input pressure function at higher pressures, as long as the energy inflow is sufficient to keep the tube open. Solidification is determined by the cooling from the outside. Only when the pressure supplies insufficient thermal energy and the tube closes, is the input pressure function relevant for the solidification. The flow rates of course depend strongly on the function selected.

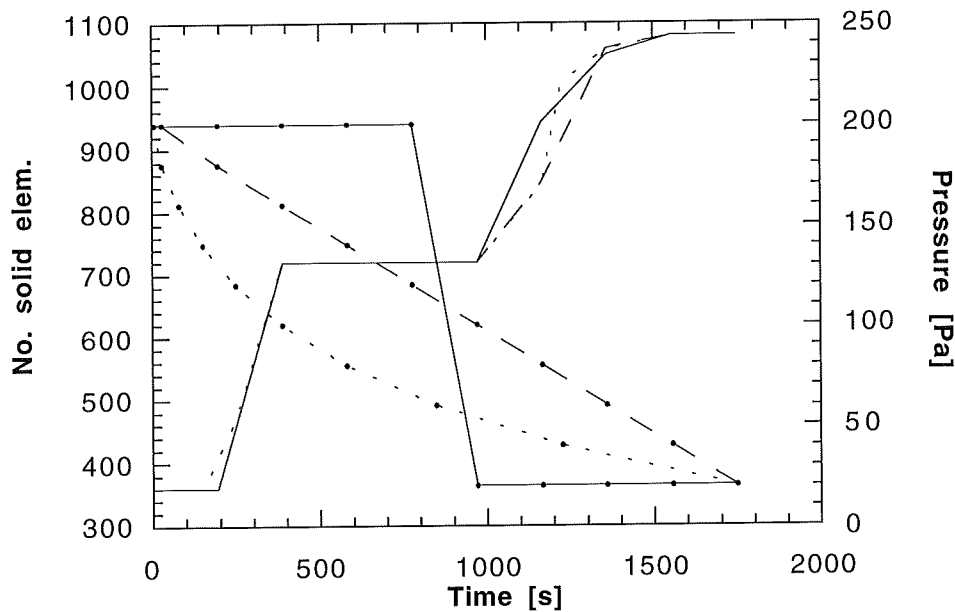


**Fig. 43** Different inflow functions (lines with markers at pressure steps) and the resulting number of solidified elements (lines without markers) in three different runs over 1800 s. The large step in the number of solid elements at 300 s is due to the selection of a whole layer of elements.

## 12.4 The influence of the inflow temperature on time-dependent runs

The inflow temperature determines the viscosity of a given lava and therefore the flow rates in the tube. Figure 44 shows the flow rates at inflow temperatures between 1333 and 1373 K in a series of time dependent model runs. The input pressure decayed exponentially from 200 Pa to 20 Pa. In these runs the function of Marsh [1981] accounting for the effect of the growing amount of crystals in the tholeiitic lava was used. The existence of superheated lava with temperatures higher than the liquidus is uncertain, and the existence of phenocrysts of early-crystallizing minerals in many chilled margins suggests that the magma was on the point of crystallization upon intrusion [Jaeger, 1968]. Therefore, no allowance for superheated lava is made in the models. As could be expected, the flow rates decrease with decreasing temperature, the difference being greater at higher pressures.

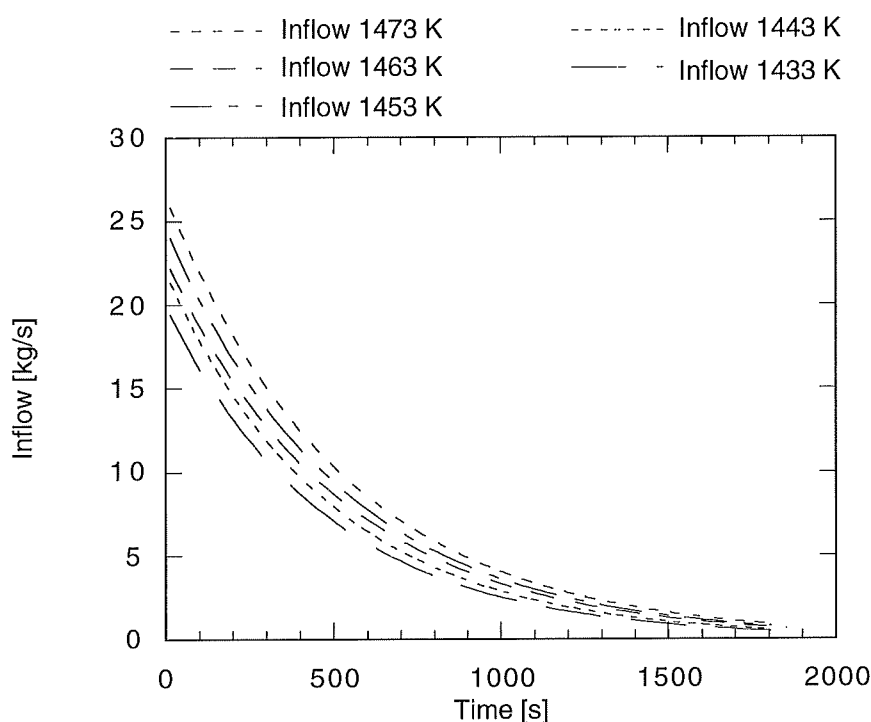


**Fig. 44** Dependency of the flow rate on the inflow temperature in a series of time-dependent model runs. Input pressure varied from 200 Pa to 20 Pa.



## 12.5 The critical pressure

The longevity of tube flow is found to be constrained by the competition of advective heat flow along the flow axis and the conduction of heat towards the margins of the flow [see chapter (12.2)]. Once the pressure driving the flow drops below a critical value, the flow loses more heat through conduction than is supplied by the influx of hot magma into the tube. In this case flow stops. This critical pressure depends on the viscosity of the fluid, the rate of cooling, the diameter and the length of the tube.

Several model runs with different tube geometries were made and the critical pressure for each run was determined with a precision of 2.5 Pa. The resulting minimum pressure and pressure drop for different tube lengths and diameters are shown in Figure 45. The critical entrance pressure depends linearly on the length of the tube. Whereas the critical pressure gradient rises more rapidly for smaller tubes; it is nearly constant for larger tubes. This is due to the influence of the cooling, which is much more effective in the entrance part of the tube where the insulating sheath is not developed.

For smaller diameters and longer tubes, the critical pressure rises above realistic values, tubes of such dimensions will not form in nature. At large diameters, the critical pressure is low, but the flow rates would be too high for a stable tube to develop. Instead, shearing of single sacks would occur.

Thus, pillows will not only exhibit a narrow range of tube diameters, as can be seen in many outcrops, but will also have a characteristic length to diameter (elongation) ratio for similar conditions. For example, tholeiitic lava used in these model calculations at an pressure gradient between 10 and 30 Pa m<sup>-1</sup> would probably form tubes with a 0.8-1.0 m diameter and a length around 5-10 m.

The exact length also depends strongly on the temperature of the inflowing lava, the amount of cooling and other factors as discussed in previous chapters. The critical pressure increases substantially for increases in viscosity, e.g. for lava of Hawaiitic composition, a constant phenocryst content of 5% at an inflow temperature of 1400 K in a 5 m long tube the critical pressure is 2150 Pa (Figure 46), around 25 times higher than for tholeiitic lava without phenocrysts. Although the critical pressure can vary greatly as described above, the mechanism of flow stoppage is the same in all cases.

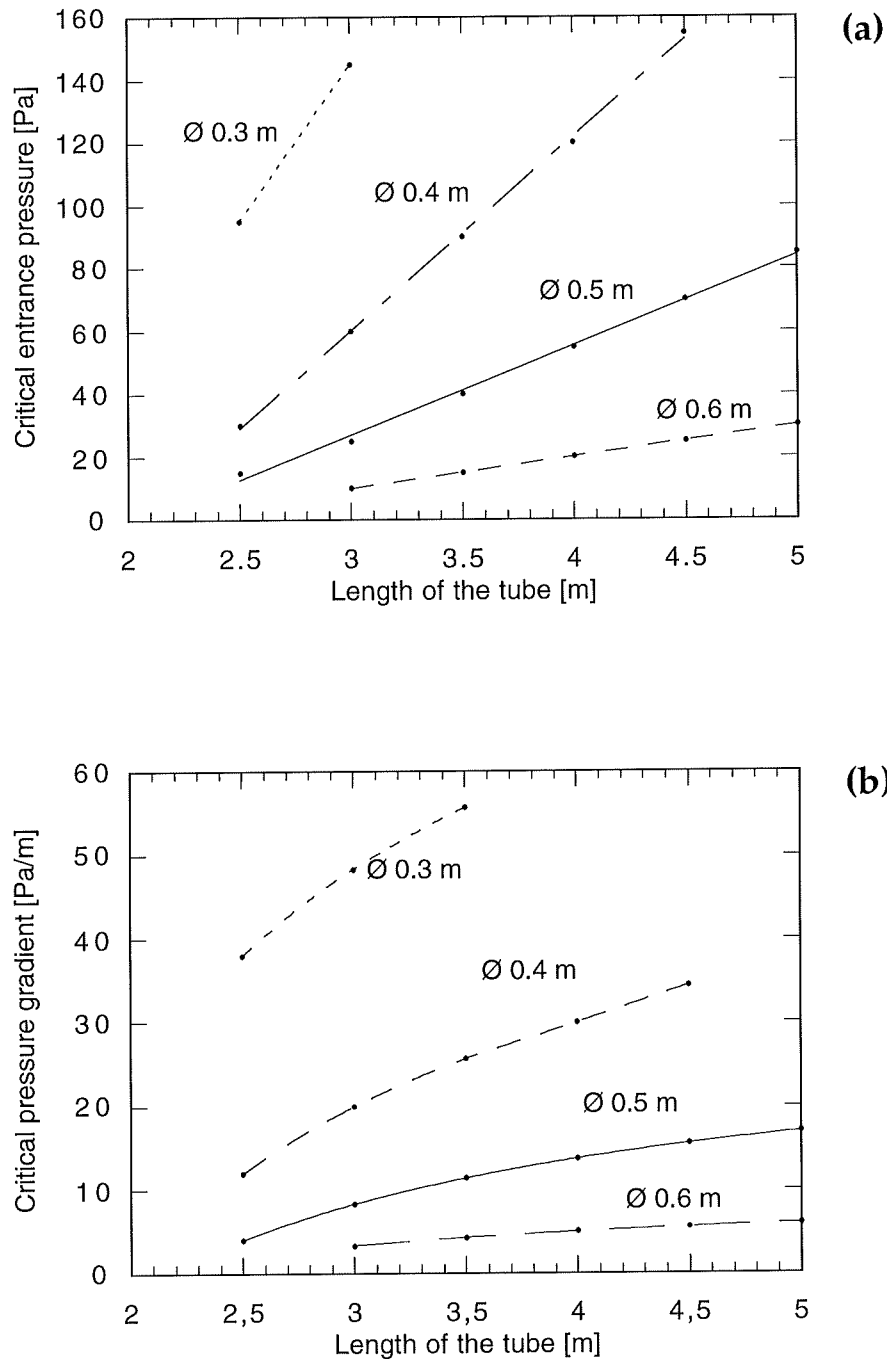


**Fig. 45** (a) Critical entrance pressure for different tube lengths and diameters. For small diameters of longer tubes, the critical pressure rises above realistic values. At larger diameters the critical pressure is low, but the flow rates would be too high for a stable tube to develop. Shearing of single sacks would occur. (b) Critical pressure gradient along the tube for different tube lengths and diameters.

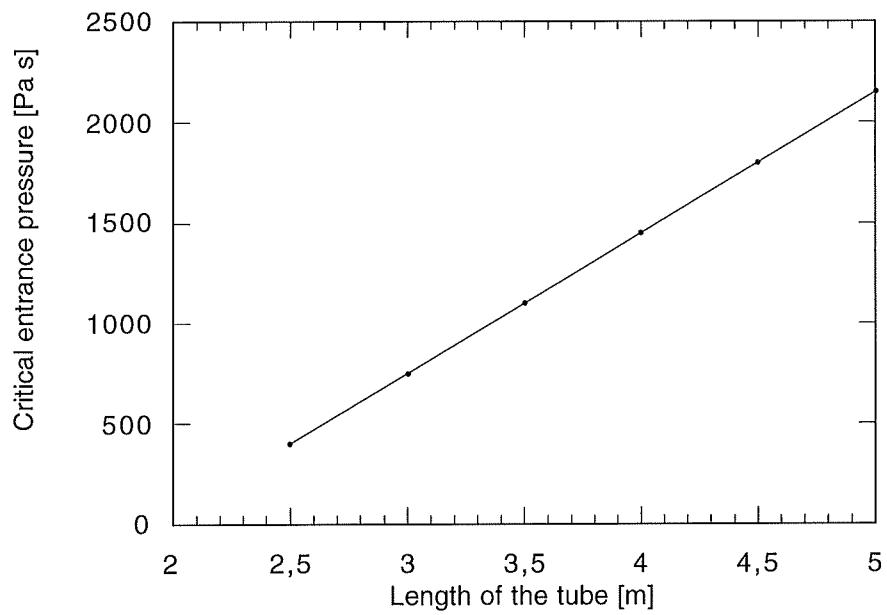


**Fig. 46** Critical pressure for hawaiitic lava at an inflow temperature of 1400 K containing 5 % phenocrysts for a tube of 5 m length and 0.5 m diameter.

### 13 Conclusions and outlook

The model calculations presented simulate characteristic types of behavior of submarine lava flow, and allow conclusions to be drawn concerning the mechanisms of formation of tube-style flow. It was not possible however to simulate all aspects of pillow growth.

Test runs were performed prior to the complex flow simulations in order to determine the relative importance of the relevant physical properties. It was demonstrated that the formation of pillow lavas is not controlled by any one single factor but by the interplay of different factors of varying importance. These include:

- (a) The supply rate strongly influences the formation and the life span of a pillow. The upper boundary is constrained through observed maximum velocities. Flow rates of tholeiitic lava in a pillow might reach up to  $250 \text{ kg s}^{-1}$
- (b) Viscosity is one of the fundamental factors controlling flow rates in pillow lavas. Therefore, parameters influencing the viscosity (crystal content, temperature and composition of the lava) were considered. For the range of basaltic compositions treated in this study, the maximum flow rates exceeded the minimum rates by a factor of 50. In contrast, the application of different crystal content-viscosity relations yielded a factor of 10 difference.
- (c) The effect of latent heat of crystallization is moderately significant despite growth of a glassy crust, after the flow has ceased and the pillow solidifies. The cooling of a stationary pillow to seawater temperature requires ca. 11 days including the latent heat and 9 days without. However it does not influence the flow behavior as long as no crystallization occurs.
- (d) The convective cooling function describes the primary energy loss from the lava tube. However, this function is difficult to quantify in submarine environments, and literature values on film coefficients differ by two orders of magnitude.
- (e) Parameters that were found to play only a minor role include: Density variation of the lava, viscous heating, and water content of the lava.

The input parameters were constrained to realistic values with varying degrees of success, because direct submarine measurements are scarce (e.g. "Leidenfrost-effect"). Other parameters were obtained from published experimental studies and reported in-situ measurements. The precision of the final results is limited by the uncertainty of

these input parameters. In contrast, the calculation error established by comparing a simple model with an analytical solution was a negligible 0.3%. The absolute temperatures and flow rates may differ from actual values due to the aforementioned factors, but several mechanisms were demonstrated, which are independent of these absolute values:

- (a) Complex model runs were conducted to constrain the boundaries of the pillow flow regime. The formation of pillows or sheet flows depends on the viscosity of the lava and the flow rate per unit area. High viscosity lavas cannot develop a tube-style flow due to the high frictional drag within the cylinder and the lava therefore propagates as a sheet flow or in irregular lobes. For moderate to low viscosity magmas, the tube flow regime is only stable for a limited range of flow rates. At higher flow rates, sheet flows develop, since they are more efficient in rapidly transporting large quantities of magma. For example, the flow rate per unit cross-sectional area of a larger sheet flow can be up to 250 times higher than that of a pillow.
- (b) To answer the question why subaqueously extruded lava builds tube-style flows, model calculations with different aspect ratios were made. It was shown that a cylindrical cross-section is the most efficient way to transport lava, because it minimizes thermal energy loss. An aspect ratio of 0.4 rather than 1.0 leads to a decrease in the flow rate of 30% for the same cross-sectional area. The buoyancy of the lava under water helps to stabilize the tube better than in pahoehoe tubes, which tend to have larger aspect ratios.
- (c) In the model tube, three different zones were distinguished: an outer layer of rapidly solidified elements, a slowly cooling inner layer, and a hot inner core, which is insulated by surrounding elements. These zones can be correlated to textures found in pillows: a glassy rind, an intermediate zone of increasing degree of crystallization, and a microcrystalline core.
- (d) Flow rates and temperature distributions in a lava tube were calculated with up to 2500 time steps with varying input pressures and temperatures. Three different phases during the active life span of a pillow lava can be distinguished. First, the hot lava is chilled by seawater and forms a glassy crust. At flow rates between 30 and 2 kg s<sup>-1</sup> a steady state phase is reached in which the heat energy influx in the tube is

sufficiently large to prevent the tube from freezing shut. In the last phase, the driving pressure, controlling the flow rates, drops below a critical value, the flow loses more heat through conduction than is supplied by the inflow of hot magma into the tube, and flow ceases.

- (e) This critical input pressure value was determined for different tube lengths. The calculations demonstrate that pillows not only exhibit a narrow range of tube diameters, but have a characteristic length to diameter ratio when extruded under similar conditions. Tholeiitic lava at a pressure gradient between 10 and 30 Pa m<sup>-1</sup> would probably form tubes with ca. 0.8 m diameter and a length around 5-10 m.

These results can be applied to estimate eruption rates and cooling times based on outcrop studies, whereby a detailed determination of several properties would be necessary (composition of the lava, phenocryst content etc). The model calculations could also be extended to different settings (e.g. subaerial lava flow, magma chamber cooling) with some modifications (e.g. geometry, cooling functions). There are also engineering applications concerning flow and solidification of liquids in tubes (e.g. water pipes freezing, oil and gas pipelines).

The mechanical behavior of the solidifying crust (e.g. fracturing, rupturing and stretching) has not been incorporated into the model. New model calculations using the moving boundary technique and adaptive meshing can be useful to determine the mechanical stability of already solidified parts, such as budding and cracking of a pillow. Calibration of the calculations on different sets of pillows extruded under different genetic conditions can help constrain the wide ranges of some parameters. Additionally, analog experiments, for example with wax in water, might be helpful to understand complex interactions, which are difficult to model, such as the interplay between the fluid and the partially solidified parts of the flow.

## **14 Acknowledgments**

My best thanks to Prof. H.-J. Kumpel for his guidance and assistance during the many phases of the modeling. Many thanks as well to Prof. H.-U. Schmincke for first suggesting the topic of this dissertation and for invaluable assistance with the field geological aspects of lava flows. Warmest thanks to Mathias Hort for help with the mathematical aspects of magma physics and thermodynamic transport and for moral support when the going got tough.

This graduate study and dissertation was financed by a Deutsche Forschungsgemeinschaft doctoral fellowship within the Graduiertenkolleg "Dynamik Globaler Kreisläufe" of the Christian-Albrechts University, Kiel. Computer hardware and software facilities were provided by the Graduiertenkolleg. Helpful administrative and infrastructure support was provided by GEOMAR.

I thank Klaus Regenauer-Lieb for support and guidance in all aspects of the GK experience. A great many thanks to Rüdiger Kunze for keeping the computer system alive (and congratulations on your baby daughter, Nadine!). Thanks to Dr. U. Göhner in Stuttgart from the Flotran software support department for helping fight our way through little bugs in the system (and I still owe you a beer). Special thanks to the "aunts" Antje, Sabine, and Susanne, and the rest of the "Coffee crew" for the pleasant working environment, interdisciplinary discussions and the munchies.

Thanks to my hubby for help with the English and the cooking. I am grateful to my parents for helping support me during my diploma studies, for the use of their Power Mac and for always being there.

## 15 List of commonly used symbols

Symbol	Description	Units and standard values	Reference
$A_\eta$	Empirical constant for lava viscosity	[Pa]	
Br	Brinkman or Gruntfest number	dimensionless	
$c_p$	Heat capacity at constant pressure, per unit mass	$730 \text{ J kg}^{-1} \text{ K}^{-1}$	Bruce and Huppert, 1990
$c_v$	Heat capacity at constant volume, per unit mass	$[\text{J kg}^{-1} \text{ K}^{-1}]$	
$c_a$	Specific heat of water	$4 \cdot 10^3 \text{ J kg}^{-1} \text{ K}^{-1}$	Gerthsen et al, 1974
D	Mean diameter of crystals	[m]	
$D_i$	Empirical constant associated with component i	dimensionless	
$E_\eta$	Activation energy of the viscous flow	$[\text{J mol}^{-1}]$	
g	Gravitational acceleration	$9.81 \text{ ms}^{-2}$	Gerthsen et al, 1974
$g_x, g_y, g_z$	Body force in x,y,z-direction	[N]	
$h_a$	Film coefficient	$\text{W m}^{-2} \text{ K}^{-1}$	Anonymous, 1992
L	Latent heat of solidification or melting	$8 \cdot 10^5 \text{ J kg}^{-1}$	Bruce and Huppert, 1990
$L_T$	Length of the tube	[m]	
P	Pressure gradient	$[\text{Pa m}^{-1}]$	
p	Pressure	[Pa]	
$Q_v$	Volumetric heat source	$[\text{W m}^{-3}]$	
q	Energy flux relative to mass average velocity	$[\text{kg s}^{-3}]$	
$R_G$	Gas constant	$8.31 \text{ J mol}^{-1} \text{ K}^{-1}$	Gerthsen et al, 1974
R	Radius of the tube	[m]	
Re	Reynolds number	dimensionless	
r	Radial distance	[m]	
$S_L$	Thermal entry length of the tube	[m]	
T	Temperature	[K]	



List of commonly used symbols

Symbol	Description	Units and standard values	Reference
$T_c$	Lava temperature at contact surface	[K]	
$T_l$	Temperature of basaltic lava at the liquidus	1473 K	Hargraves, 1980
$T_r$	Reference temperature	[K]	
$T_s$	Temperature of basaltic lava at the solidus	1333 K	Hargraves, 1980
$T_a$	Adopted temperature of seawater	280 K	
$t$	Time	[s]	
$U$	Internal energy	[J]	
$v_x, v_y, v_z$	Velocity of the lava flow in x,y,z-direction	[ms <sup>-1</sup> ]	
$\bar{V}_i^0$	Constants derived from analysis of volume-composition relation in alumina free silicate liquids	dimensionless	
$\bar{V}_A^0$	Composition-dependent apparent partial molar volume of Al <sub>2</sub> O <sub>3</sub>	dimensionless	
$V$	Temperature-dependent volume	[m <sup>3</sup> ]	
$V_r$	Reference volume	[m <sup>3</sup> ]	
$V_t$	Terminal velocity	[ms <sup>-1</sup> ]	
$X_A$	Mole fraction of Al <sub>2</sub> O <sub>3</sub>	dimensionless	
$X_i$	Mole fraction of oxide component i	dimensionless	
$\alpha$	Thermal expansion coefficient	[K <sup>-1</sup> ]	
$\alpha_a$	Thermal expansion coefficient of water	1*10 <sup>-2</sup> K <sup>-1</sup>	Griffiths and Fink, 1992a
$\bar{\alpha}_i^0$	Constants independent of temperature and composition	dimensionless	
$\bar{\alpha}_A^0$	Composition-dependent term representing the effect of Al <sub>2</sub> O <sub>3</sub> on the thermal expansion	dimensionless	
$\beta$	Constant, that varies with mean diameter	dimensionless	
$\Phi$	Viscous dissipation function	[s <sup>-2</sup> ]	
$\phi$	Volume fraction of crystals	dimensionless	

**List of commonly used symbols**

Symbol	Description	Units and standard values	Reference
$\phi_{\max}$	Concentration of solids at closest packing	dimensionless	
$\phi_{\text{sol}}$	Crystallization degree reached at the solidus	dimensionless	
$\gamma$	Constant value for convective cooling through seawater	$\approx 0.1$	Griffiths and Fink, 1992a
$\lambda$	Thermal conductivity of basaltic lava	$2.5 \text{ Js}^{-1}\text{m}^{-1}\text{K}^{-1}$	Bruce and Huppert, 1990
$\eta$	Viscosity of basaltic lava	100 Pa s	Moore, 1975
$\eta_0$	Viscosity of the crystal-free liquid [Pa s]	[Pa s]	
$\eta_R$	Relative viscosity	dimensionless	
$\rho$	Density of basaltic lava	$2800 \text{ kg m}^{-3}$	Hargraves, 1980
$\rho_a$	Density of the water	$1 \cdot 10^3 \text{ kg m}^{-3}$	Griffiths and Fink, 1992a
$\tau$	Viscous stress tensor	[Pa]	
$\kappa_a$	Thermal diffusivity of water	$1 \cdot 10^{-7} \text{ m}^2 \text{ s}^{-1}$	Griffiths and Fink, 1992a
$\nu_a$	Kinematic viscosity of seawater	$[\text{m}^2 \text{ s}^{-1}]$	

---

## 16 References

- Anderson DA, Tannehill JC, Pletcher RH (1984) Computational fluid mechanics and heat transfer. Hemisphere Publishing Corporation, New York, 599 pp
- Anonymous (1986) PDE/PROTRAN manual IMSL Inc., Houston, Texas
- Anonymous (1992) FLOTRAN 2.1 manual Compuflo Inc., Houston, Pennsylvania
- Appelgate B, Embley RW (1991) Submarine tumuli and inflated tube-fed lava flows on Axial Volcano, Juan de Fuca Ridge. *Bull. Volcanol.* 54: 447-458
- Ballard RD, Holcomb TH, van Andel TH (1979) The Galapagos Rift at 86°W: 3. Sheet flows, collapse pits, and lava lakes of the rift valley. *J. Geophys. Res.* 84: 5407-22
- Ballard RD, Moore JG (1977) Photographic atlas of the Mid-Atlantic Ridge Rift Valley. Springer-Verlag, New York, 114 pp
- Baloga S, Pieri D (1986) Time-dependent profiles of lava flows. *J. Geophys. Res.* 91: 9543-9552
- Baragar WRA (1984) Pillow formation and layered flows in the Circum-Superior Belt of eastern Hudson Bay. *Can. J. Earth Sci.* 21: 781-792
- Batiza R, Fornari DJ, Vanko DA, Lonsdale P (1984) Craters, calderas and hyaloclastites on young Pacific seamounts. *J. Geophys. Res.* 89: 8371-8390
- Batiza R, Vanko D (1983) Volcanic development of small oceanic central volcanoes on the flanks of the East Pacific Rise inferred from narrow beam echo sounder surveys. *Mar. Geol.* 54: 53-90
- Bednarz U (1988) Volcanological, geochemical and petrological evolution, and sub-seafloor alteration in the northeastern Troodos ophiolite (Cyprus). Doctoral Dissertation Ruhr-Universität Bochum
- Bird RB, Steward WE, Lightfoot EN (1960) Transport phenomena. Wiley & Sons, New York, 780 pp
- Borgia A, Linneman SR (1990) On the mechanisms of lava flow emplacement and volcano growth: Arenal, Costa Rica. In: Fink JH (ed) *Lava flows and domes*. Springer-Verlag, 208-243
- Bottinga Y. (1994). Rheology and rupture of homogeneous silicate liquids at magmatic temperatures. *J. Geophys. Res.*, 99, 9415-9422.
- Bottinga Y, Weill D, Richet P (1982) Density calculations for silicate liquids, 1. revised method for aluminosilicate compositions. *Geochimica et Cosmochimica Acta* 46: 909-919
- Bottinga Y, Weill DF (1972) The viscosity of magmatic silicate liquids: a model for calculation. *Am. J. Sci.* 272: 438-475
- Bruce PM, Huppert HE (1990) Solidification and melting along dykes by the laminar flow of basaltic magma. In: Ryan MP (ed) *Magma transport and storage*. 87-101
- Bryan WB (1972) Morphology of quench crystals in submarine basalts. *J. Geophys. Res.* 77: 5812-5819
- Bryan WB (1991) From pillow lava to sheet flow - evolution of deep-sea volcanology. *Oceanus* 34 (Winter): 42-50
- Cashman KV, Mangan MT, Newman S (1994) Surface degassing and modification to vesicle size distributions in active basalt flows. *J. Volcanol. Geotherm. Res.* 61: 45-68

- Coleman RG (1977) Ophiolites. Ancient oceanic lithosphere? Minerals and rocks. Springer-Verlag, Berlin-Heidelberg-New York, 229 pp
- Cousineau P, Dimroth E (1982) Interpretation of the relations between massive, pillowed and brecciated facies in an Archean submarine andesite volcano - Amulet Andesite, Rouyn-Noranda, Canada. *J. Volcanol. Geotherm. Res.* 13: 83-102
- Cox KG, Bell JD, Pankhurst RJ (1979) The interpretation of igneous rocks. Unwin Hyman Ltd, Boston, 450 pp
- Crisp J, Baloga SM (1990) A model for lava flows with two thermal components. *J. Geophys. Res.* 95: 1255-70
- Danes ZF (1972) Dynamics of lava flows. *J. Geophys. Res.* 77: 1430-1432
- Des Marais DJ, Moore JG (1984) Carbon and its isotopes in mid-oceanic glasses. *Earth Planet. Sci. Lett.* 69: 43-57
- deWit MJ, Stern C (1978) Pillow talk. *J. Volcanol. Geotherm. Res.* 4: 55-80
- Dimroth E, Cousineau P, Leduc M, Sanschagrin Y (1978) Structure and organization of Archean subaqueous basalt flows, Rouyn-Noranda area, Quebec, Canada. *Can. J. Earth Sci.* 15: 902-918
- Dimroth E, Lichtblau A P. (1979) Metamorphic evolution of Archean hyaloclastite, Noranda area, Québec, Canada. Part 1: Comparison of Archean and Cenozoic sea-floor metamorphism. *Can. J. Earth Sci.* 16: 1315-1340
- Dingwell DB, Bagdassarov NS, Bussod GY, Webb SL (1993) Magma rheology. Mineral. Assoc. Canada Short Course Handbook on Experiments at High Pressure and Applications to the Earth's Mantle 21: 131-196
- Dragoni M (1989) A dynamical model of lava flows cooling by radiation. *Bull. Volcanol.* 51: 88-95
- Dragoni M, Bonafede M, Boshi E (1986) Downslope flow models of a Bingham liquid: Implications for lava flows. *J. Volcanol. Geotherm. Res.* 30: 305-325
- Dragoni M, Tallarico A (1994) The effect of crystallization on the rheology and dynamics of lava flows. *J. Volcanol. Geotherm. Res.* 59: 241-252
- Dudas FÖ (1983) The effect of volatile content on the vesiculation of submarine basalts. *Economic Geology* 3: 134-141
- Duffield WA (1978) Vesicularity of basalt erupted at Reykjanes Ridge crest. *Nature* 274: 217-220
- Einstein A (1906) Eine neue Bestimmung der Molekül-Dimensionen. *Ann. Phys.* 19: 289-306
- Einstein A (1911) Berichtigung zu meiner Arbeit: Eine neue Bestimmung der Molekül-Dimensionen. *Ann. Phys.* 34: 591-592
- Fink JH, Griffith RW (1990) Radial spreading of viscous-gravity currents with solidifying crust. *J. Fluid. Mech.* 221: 485-509
- Fisher RV, Schmincke H-U (1984) Pyroclastic rocks. Springer Verlag, New York, 472
- Fornari DJ (1986) Submarine lava tubes and channels. *Bull. Volcanol.* 48: 291-298
- Fornari DJ, Lockwood JP, Lipman PW, Rawson M, Malahoff A (1980) Submarine volcanic features west of Kealahue Bay, Hawaii. *J. Volcanol. Geotherm. Res.* 7: 323-337
- Fornari DJ, Ryan WBF (1984) The evolution of craters and calderas on young seamounts: insights from SeaMARC I and Sea Beam sonar surveys of a small seamount group near the axes of the East Pacific Rise at 10°N. *J. Geophys. Res.* 89: 11069-11083

- Fornari DJ, Ryan WBF, Fow PJ (1985) Sea-floor lava fields on the East Pacific Rise. *Geology* 13: 413-416
- Fridleifson IB, Furnes H, Atkins FB (1982) Subglacial volcanics - on the control of magma chemistry on pillow dimensions. *J. Volcanol. Geotherm. Res.* 13: 84-117
- Fuji N, Uyeda S (1974) Thermal instabilities during flow of magma in volcanic conduits. *J. Geophys. Res.* 79: 3367-3369
- Furnes H, Fridleifsson IB (1978) Relationship between the chemistry and axial dimensions of alkali olivine basaltic and olivine tholeiitic pillow lava. *Bull. Volcanol.* 41: 136-146
- Gerthsen C, Kneser HO, Vogel H (1974) *Physik*. Springer-Verlag, Berlin, 873 pp
- Ghiorso MS (1985) Chemical mass transfer in magmatic systems. I. Thermodynamic relations and numerical algorithms. *Contrib. Mineral. Petrol.* 90: 107-120
- Griffiths RW, Fink JH (1992a) Solidification and morphology of submarine lavas: a dependence on extrusion rate. *J. Geophys. Res.* 97: 19,729-19,737
- Griffiths RW, Fink JH (1992b) The morphology of lava flows in planetary environments: prediction from analog experiments. *J. Geophys. Res.* 97: 19,739-19,748
- Griffiths RW, Fink JH (1993) Effects of surface cooling on the spreading of lava flows and domes. *J. Fluid. Mech.* 252: 667-702
- Gruntfest IJ (1963) Thermal feedback in liquid flow: plane shear at constant stress. *Trans. Soc. Rheol.* 7: 195-207
- Gruntfest IJ, Young JP, Johnson NL (1964) Temperatures generated by the flow of liquids in pipes. *J. Appl. Phys.* 35: 18-22
- Hardee HC (1993) Thermal feedback mechanisms and their potential influence on the emplacement of lavas. In: Kilburn CJ & Luongo G (ed) *Active lavas: monitoring and modelling*. UCL Press, London, 281-289
- Hardee HC, Larson DW (1977) Viscous dissipation effects in magma conduits. *Bull. Volcanol. Geotherm. Res.* 2: 299-308
- Hargraves RB (1980) *Physics of magmatic processes*. Princeton University Press, Princeton, 585 pp
- Hargreaves R, Ayres LD (1979) Morphology of Archean metabasalt flows, Utik Lake, Manitoba. *Can. J. Earth Sci.* 16: 1452-1466
- Holcomb RT (1988) Voluminous submarine lava flows from Hawaiian volcanoes. *Geology* 16: 400-404
- Hulme G (1974) The interpretation of lava flow morphology. *Geophys. J. Roy. Astron. Soc.* 39: 361-83
- Jaeger JC (1968) *Cooling and solidification of igneous rocks*. Wiley & Sons, New York, 503-536
- Jones JG (1968) Pillow lava and pahoehoe. *J. Geol.* 76: 485-488
- Jones JG (1969) Pillow lavas as depth indicators. *Am. J. Sci.* 267: 181-195
- Jones JG, Nelson PHH (1970) The flow of basalt lava from air into water - its structural expression and stratigraphic significance. *Geol. Mag.* 107(1): 13-19
- Kano K, Takeuchi K, Yamamoto T, Hoshizumi H (1991) Subaqueous rhyolite block lavas in the Miocene Ushikiri formation, Shimane Peninsula, SW Japan. *J. Volcanol. Geotherm. Res.* 46: 241-253

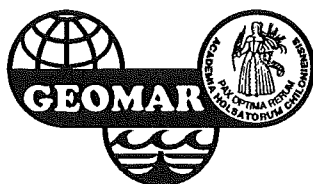
- Kawachi Y, Pringle IJ (1988) Multiple-rind structure in pillow lava as an indicator of shallow water. *Bull. Volcanol.* 50: 161-168
- Kearsley EA (1962) The viscous heating correction for viscometer flows. *Trans. Soc. Rheol.* 6: 253-261
- Kerr RC, Lister JR (1991) The effects of shape on crystal settling and on the rheology of magmas. *J. Geol.* 99: 457-467
- Kirkpatrick, R. J., 1976. Towards a kinetic model for the crystallization of magma bodies. *J. Geophys. Res.* 81: 2565-2571.
- Kokelaar P (1986) Magma-water interactions in subaqueous and emergent basaltic volcanism. *Bull. Volcanol.* 48: 275-289
- Kushiro I (1980) Viscosity, density, and structure of silicate melts at high pressures, and their petrological applications. In: Hargraves RB (ed) *Physics of magmatic processes*. Princeton University Press, Princeton, 93-120
- Lejeune A-M, Richet P (1995) Rheology of crystal-bearing silicate melts: An experimental study at high viscosities. *J. Geophys. Res.* 100: 4215-4229
- Lewis JV (1914) Origin of pillow lavas. *Geol. Soc. Am. Bull.* 25: 591-654
- Lipman PW, Banks NG, Rhodes JM (1985) Degassing-induced crystallization of basaltic magma and effects on lava rheology. *Nature* 317: 604-607
- Lonsdale P (1977) Abyssal pahoehoe with lava coils at the Galapagos rift. *Geology* 5: 147-152
- Lonsdale P, Batiza R (1980) Hyaloclastite and lava flows on young seamounts examined with a submersible. *Geol. Soc. Am. Bull.* 91: 545-54
- Lydersen AL (1979) *Fluid flow and heat transfer*. Wiley & Sons, New York, 537 pp
- Macpherson GJ (1984) A model for predicting the volumes of vesicles in submarine basalts. *J. Geol.* 92: 73-82
- Malin MC (1980) Length of Hawaiian lava flows. *Geology* 8: 306-308
- Marsh BD (1981) On the crystallinity, probability of occurrence, and rheology of lava and magma. *Contrib. Mineral. Petrol.* 78: 85-98
- McBirney AR (1963) Factors governing the nature of submarine volcanism. *Bulletin Volcanologique* 26: 455-69
- McBirney AR (1994) *Igneous petrology*. Jones & Bartlett, London, 508 pp
- McBirney AR, Murase T (1984) Rheological properties of magmas. *Ann. Rev. Earth Planet. Sci.* 12: 337-57
- McPie J, Doyle M, Allen R (1993) *Volcanic textures: a guide to the interpretation of textures in volcanic rocks*. University of Tasmania, 198 pp
- Mills AA (1984) Pillow lavas and the Leidenfrost effect. *J. Geol. Soc. London* 141: 183-186
- Moore, H J (1987). Preliminary estimates of the rheological properties of 1984 Mauna Loa lava. *US GS Prof. Paper*, 1350, 1569-1588.
- Moore JG (1965) Petrology of deep-sea basalt near Hawaii. *Am. J. Sci.* 263: 40-52
- Moore JG (1970) Water content of basalt erupted on the ocean floor. *Contr. Miner. Petrol.* 28: 272-279
- Moore JG (1975) Mechanism of formation of pillow lava. *Am. Sci.* 63: 269-277
- Moore JG (1979) Vesicularity and CO<sub>2</sub> in mid-ocean ridge basalt. *Nature* 282: 250-253

- Moore JG, Charlton DW (1984) Ultrathin lava layers exposed near San Luis Obispo Bay, California. *Geology* 12: 542-545
- Moore JG, Cristofolini R, Lo Giudice A (1971) Developement of pillows on the submarine extension of recent lava flows, Mount Etna, Sicily. U.S.G.S. Prof. Paper 750-C: C89-C97
- Moore JG, Batchelder JN, Cunningham CG (1977) CO<sub>2</sub>-filled vesicles in mid-ocean basalt. *J. Volcanol. Geotherm. Res.* 2: 309-327
- Moore JG, Lockwood JP (1978) Spreading cracks on pillow lava. *J. Geol.* 86: 661-671
- Moore JG, Phillips RL, Grigg RW, Peterson DW, Swanson DA (1973) Flow of lava into the sea, 1969-1971, Kilauea Volcano, Hawaii. *Geol. Soc. Am. Bull.* 84: 537-46
- Moore JG, Schilling J-G (1973) Vesicles, water and sulfur in Reykjanes Ridge basalts. *Contr. Mineral. Petrol.* 41: 105-118
- Murase T, McBirney AR (1973) Properties of some common igneous rocks and their melts at high temperatures. *Geol. Soc. Am. Bull.* 84: 3563-3592
- Natland JH (1978) Crystal morphologies in basalts from DSDP site 395, 23°N, 46°W, Mid Atlantik Ridge. In: Initial Reports of the Deep Sea Drilling Project. US Goverment Printing Office, Washington, 45, 423-446
- Nichols RL (1939) Viscosity of lava. *J. Geology* 47: 290-302
- Nicolas A (1995) Die ozeanischen Rücken: Gebirge unter dem Meer. Springer Verlag, Berlin, 200 pp
- Park SO, Iverson JD (1984) Dynamics of flowing lava: thickness, growth characteristics of two dimensional flow. *Geophys. Res. Lett.* 11: 641-644
- Peterson DW (1976) Processes of volcanic island growth, Kilauea Volcano, Hawaii, 1969-1973. Proceedings of the Symposium on Andean and Antarctic Volcanology Problems. Santiago, Chile, 1-18
- Peterson DW, Swanson DA (1974) Observed formation of lava tubes during 1970-71 at Kilauea Volcano, Hawaii. *Studies in Speleology* 2(no. 6): 209-222
- Philpotts AR (1990) Principles of igneous and metamorphic petrology. Prentice Hall, Englewood Cliffs, New Jersey, 479
- Pieri DC, Baloga SM (1986) Eruption rate, area, and length relationships for some Hawaiian flows. *J. Volcanol. Geotherm. Res.* 30: 29-45
- Pinkerton H, Sparks RSJ (1978) Field measurements of the rheology of flowing lava. *Nature* 276: 383-5
- Pinkerton H, Stevenson RJ (1992) Methods of determining the rheological properties of magmas at sub-liquidus temperatures. *J. Volcanol. Geotherm. Res.* 53: 47-66
- Pinkerton H, Wilson L (1994) Factors controlling the length of channel-fed lava flows. *Bull. Volcanol.* 56: 108-120
- Robertson EC (1988) Thermal properties of rocks. USGS open file report 88-441: 1-106
- Roscoe R (1952) The viscosity of suspensions of rigid spheres. *British J. Appl. Physics* 3: 267-269
- Ryerson FJ, Weed HC, Piwinskii AJ (1988) Rheology of subliquidus magmas, 1. Picritic composition. *J. Geophys. Res.* 93: 3421-3436
- Schmincke H-U (1988) Devonischer und karbonischer Vulkanismus bei Dillenburg und Herbornseelbach (Exkursion F am 8. April 1988). *Jber. Mitt. oberrhein. geol. Ver.* 70: 99-140

- Schmincke H-U, Bednarz U (1990) Pillow, sheet flow and breccia flow volcanoes and volcano-tectonic hydrothermal cycles in the extrusive series of the Troodos ophiolite (Cyprus). In: Malpas J (ed) Oceanic crustal analogues; Proceedings of the symposium "Troodos 1987. Geological Survey Department, Republic of Cyprus, 185 - 207
- Schmincke H-U, Rautenschlein M (1987) Volcanology along the Akaki River Canyon. In: Xenophontos C & Malpas JG (ed) Field Excursion Guidebook -Troodos- Ophiolites and Oceanic Lithosphere. Geological Survey Department, Nicosia, Cyprus, 36-91
- Schmincke H-U, Rautenschlein M, Robinson PT, Mehegan JM (1983) Troodos extrusive series of Cyprus: A comparison with oceanic crust. *Geology* 11: 405-409
- Schmincke H-U, Sunkel G (1987) Carboniferous submarine volcanism at Herbornseelbach (Lahn-Dill area, Germany). *Geol. Rundschau* 76/3: 709-734
- Schmincke H-U, Staudigel H (1976) Pillow lavas on central and eastern Atlantic Islands. *Bull. Soc. Géol. France* 4: 871-883
- Sewell G (1985) Analysis of a Finite Element Method, PDE/PROTRAN. Springer-Verlag, New York, 359 pp
- Shaw HR (1969) Rheology of basalt in the melting range. *J. Petrol.* 10: 510-535
- Shaw HR (1972) Viscosities of magmatic silicate liquids: an empirical method of prediction. *Am. J. Sci.* 272: 870-893
- Shaw HR, Wright TL, Peck DL, Okamura R (1968) The viscosity of basaltic magma: an analysis of field measurements in Makaopuhi Lava Lake, Hawaii. *Am. J. Sci.* 266: 225-261
- Sherman P (1968) Emulsion science. Academic, New York, 351
- Smith DK, Cann JR (1992) The role of seamount volcanism in crustal construction at the mid-atlantic ridge (24°-30°N). *J. Geophys. Res.* 97: 1645-1658
- Smith TL, Batiza R (1989) New field and laboratory evidence for the origin of hyaloclastite flows on seamount summits. *Bull. Volcanol.* 51: 96-114
- Snyder GL, Fraser GD (1963) Pillowed lavas 2: A review of selected recent literature. USGS Prof. Pap. 454-C: C1-C7
- Sparks RSJ (1978) The dynamics of bubble formation and growth in magmas: A review and analysis. *J. Volcanol. Geotherm. Res.* 3: 1-37
- Sparks RSJ, Pinkerton H (1978) Effect of degassing on the rheology of basaltic lava. *Nature* 276: 385-386
- Staudigel H, Schmincke H-U (1984) The Pliocene seamount series of La Palma/Canary Islands. *J. Geophys. Res.* 89: 11195-11215
- Tribble GT (1991) Underwater observations of active lava flows from Kilauea volcano, Hawaii. *Geology* 19: 633-636
- Turcotte DL, Schubert G (1982) Geodynamics. Wiley & Sons, New York, 450 pp
- Viereck LG, Flower MFJ, Hertogen J, Schmincke H-U, Jenner GA (1989) The genesis and significance of N-MORB sub-types. *Contrib. Mineral. Petrol.* 102: 112-126
- Walker GPL (1973) Length of lava flows. *Philos. Trans. R. Soc. London Ser. A.* 274: 107-118
- Walker GPL (1987) Pipe vesicles in Hawaiian basaltic lavas: their origin and potential as paleoslope indicators. *Geology* 15: 84-87
- Walker GPL (1992) Morphometric study of pillow-size spectrum among pillow lavas. *Bull. Volcanol.* 54: 459-474



- Waters AC (1960) Determining direction of flow in basalts. *Am. J. Sci.* 258-A: 350-366
- Wells G, Bryan W B., Pearce T H. (1979) Comparative morphology of ancient and modern pillow lavas. *J. Geol.* 87: 427-440
- Wilmoth RA, Walker GPL (1993) P-type and s-type pahoehoe: a study of vesicle distribution patterns in Hawaiian lava flows. *J. Volcanol. Geotherm. Res.* 55: 129-142
- Wilson M (1989) *Igneous petrogenesis*. Unwin Hyman, London, 466 pp
- Wohletz KH (1986) Explosive magma-water interactions: Thermodynamics, explosive mechanisms, and field studies. *Bull. Volcanol.* 48: 245-264
- Yamagishi H (1985) Growth of pillow lobes - Evidence from pillow lavas of Hokkaido, Japan, and North Island, New Zealand. *Geology* 13: 499-502
- Yamagishi H (1987) Studies on the Neogene subaqueous lavas and hyaloclastites in southwest Hokkaido. *Rep. Geol. Survey Hokkaido* 59: 173-181
- Yamagishi H, Sakamoto I, Ishii J (1989) Internal structures of pillow lobes of Cenozoic and Mesozoic pillow lavas in and around Hokkaido. *Proceedings of Hokkaido Tokai University Science and Engineering* 2: 107-118



## GEOMAR REPORTS

- 1 GEOMAR FORSCHUNGSZENTRUM FÜR MARINE GEOWISSENSCHAFTEN DER CHRISTIAN-ALBRECHTS-UNIVERSITÄT ZU KIEL  
BERICHT FÜR DIE JAHRE 1987 UND 1988. 1989. 71 + 6 pp.  
In German
- 2 GEOMAR FORSCHUNGSZENTRUM FÜR MARINE GEOWISSENSCHAFTEN DER CHRISTIAN-ALBRECHTS-UNIVERSITÄT ZU KIEL  
JAHRESBERICHT / ANNUAL REPORT 1989. 1990. 96 pp.  
In German and English
- 3 GEOMAR FORSCHUNGSZENTRUM FÜR MARINE GEOWISSENSCHAFTEN DER CHRISTIAN-ALBRECHTS-UNIVERSITÄT ZU KIEL  
JAHRESBERICHT / ANNUAL REPORT 1990. 1991. 212 pp.  
In German and English
- 4 ROBERT F. SPIELHAGEN  
DIE EISDRIFT IN DER FRAMSTRASSE WÄHREND DER LETZTEN 200.000 JAHRE. 1991. 133 pp.  
In German with English summary
- 5 THOMAS C. W. WOLF  
PALÄO-OZEANOGRAPHISCH-KLIMATISCHE ENTWICKLUNG DES NÖRDLICHEN NORDATLANTIKS SEIT DEM SPÄTEN NEOGEN  
(ODP LEGS 105 UND 104, DSDP LEG 81). 1991. 92 pp.  
In German with English summary
- 6 SEISMIC STUDIES OF LATERALLY HETEROGENOUS STRUCTURES - INTERPRETATION AND MODELLING OF SEISMIC DATA.  
Edited by ERNST R. FLUEH  
Commission on Controlled Source Seismology (CCSS), Proceedings of the 8th Workshop Meeting, held at  
Kiel - Fellhorst (Germany), August 27-31, 1990. 1991. 359 pp.  
In English
- 7 JENS MATTHIESSEN  
DINOFLAGELLATEN-ZYSTEN IM SPÄTQUARTÄR DES EUROPÄISCHEN NORDMEERES: PALÖKOLOGIE UND PALÄO-OZEANOGRAPHIE. 1991. 104 pp.  
In German with English summary
- 8 DIRK NÜRNBERG  
HAUPT- UND SPURENELEMENTE IN FORAMINIFERENGEHÄUSEN - HINWEISE AUF KLIMATISCHE UND OZEANOGRAPHISCHE ÄNDERUNGEN  
IM NÖRDLICHEN NORDATLANTIK WÄHREND DES SPÄTQUARTÄRS. 1991. 117 pp.  
In German with English summary
- 9 KLAS S. LACKSCHEWITZ  
SEDIMENTATIONSPROZESSE AM AKTIVEN MITTELOZEANISCHEN KOLBEINSEY RÜCKEN (NÖRDLICH VON ISLAND). 1991. 133 pp.  
In German with English summary
- 10 UWE PAGELS  
SEDIMENTOLOGISCHE UNTERSUCHUNGEN UND BESTIMMUNG DER KARBONATLÖSUNG IN SPÄTQUARTÄREN SEDIMENTEN DES ÖSTLICHEN  
ARKTISCHEN OZEANS. 1991. 106 pp.  
In German with English summary
- 11 FS POSEIDON - EXPEDITION 175 (9.10.-1.11.1990)  
175/1: OSTGRÖNLÄNDISCHER KONTINENTALRAND (65° N)  
175/2: SEDIMENTATION AM KOLBEINSEYRÜCKEN (NÖRDLICH VON ISLAND)  
Hrsg. von J. MIENERT und H.-J. WALLRABE-ADAMS. 1992. 56 pp. + app.  
In German with some English chapters
- 12 GEOMAR FORSCHUNGSZENTRUM FÜR MARINE GEOWISSENSCHAFTEN DER CHRISTIAN-ALBRECHTS-UNIVERSITÄT ZU KIEL  
JAHRESBERICHT / ANNUAL REPORT 1991. 1992. 152 pp.  
In German and English
- 13 SABINE E. I. KÖHLER  
SPÄTQUARTÄRE PALÄO-OZEANOGRAPHISCHE ENTWICKLUNG DES NORDPOLARMEERES UND EUROPÄISCHEN NORDMEERES ANHAND VON  
SAUERSTOFF- UND KOHLENSTOFF- ISOTOPENVERHÄLTNISSEN DER PLANKTISCHEN FORAMINIFERE  
*Neogloboquadrina pachyderma* (sin.). 1992. 104 pp.  
In German with English summary
- 14 FS SONNE - FAHRTBERICHT SO 78 PERUVENT: BALBOA, PANAMA - BALBOA, PANAMA, 28.2.1992-16.4.1992  
Hrsg. von ERWIN SUESS. 1992. 120 pp.  
In German with some English chapters
- 15 FOURTH INTERNATIONAL CONFERENCE ON PALEOCEANOGRAPHY (ICP IV): SHORT- AND LONG-TERM GLOBAL CHANGE:  
RECORDS AND MODELLING 21-25 SEPTEMBER 1992, KIEL/GERMANY  
PROGRAM & ABSTRACTS. 1992. 351 pp.  
In English
- 16 MICHAELA KUBISCH  
DIE EISDRIFT IM ARKTISCHEN OZEAN WÄHREND DER LETZTEN 250.000 JAHRE. 1992. 100 pp.  
In German with English summary
- 17 PERSISCHER GOLF: UMWELTGEFÄHRDUNG, SCHADENSERKENNUNG, SCHADENSBEWERTUNG AM BEISPIEL DES MEERESBODENS; ERKENNEN  
EINER ÖKOSYSTEMVERÄNDERUNG NACH ÖLEINTRÄGEN. Schlußbericht zu den beiden BMFT-Forschungsvorhaben 03F0055 A+B. 1993. 108 pp.  
In German with English summary
- 18 TEKTONISCHE ENTWÄSSERUNG AN KONVERGENTEN PLATTENRÄNDERN / DEWATERING AT CONTINENTAL MARGINS.  
Hrsg. von / ed. by ERWIN SUESS. 1993. 106 + 32 + 68 + 16 + 22 + 38 + 4 + 19 pp.  
Some chapters in English, some in German

- 19 THOMAS DICKMANN  
DAS KONZEPT DER POLARISATIONSMETHODE UND SEINE ANWENDUNGEN AUF DAS SEISMISCHE VEKTORWELLENFELD  
IM WEITWINKELBEREICH. 1993. 121 pp.  
In German with English summary
- 20 GEOMAR FORSCHUNGSZENTRUM FÜR MARINE GEOWISSENSCHAFTEN DER CHRISTIAN-ALBRECHTS-UNIVERSITÄT ZU KIEL  
JAHRESBERICHT / ANNUAL REPORT 1992. 1993. 139 pp.  
In German and English
- 21 KAI UWE SCHMIDT  
PALYNOMORPHE IM NEOGENEN NORDATLANTIK - HINWEISE ZUR PALÄO-OZEANOGRAPHIE UND PALÄOKLIMATOLOGIE. 1993. 104 + 7 + 41 pp.  
In German with English summary
- 22 UWE JÜRGEN GRÜTZMACHER  
DIE VERÄNDERUNGEN DER PALÄOGEOGRAPHISCHEN VERBREITUNG VON *BOLBOFORMA* - EIN BEITRAG ZUR REKONSTRUKTION UND  
DEFINITION VON WASSERMASSEN IM TERTIÄR. 1993. 104 pp.  
In German with English summary
- 23 RV PROFESSOR LOGACHEV - Research Cruise 09 (August 30 - September 17, 1993): SEDIMENT DISTRIBUTION ON THE REYKJANES RIDGE NEAR 59°N  
Edited by H.-J. WALLRABE-ADAMS & K.S. LACKSCHEWITZ. 1993. 66 + 30 pp.  
In English
- 24 ANDREAS DETTMER  
DIATOMEEN-TAPHOZÖNOSEN ALS ANZEIGER PALÄO-OZEANOGRAPHISCHER ENTWICKLUNGEN IM PLIOZÄN UND QUARTÄR  
NORDATLANTIK. 1993. 113 + 10 + 25 pp.  
In German with English summary
- 25 GEOMAR FORSCHUNGSZENTRUM FÜR MARINE GEOWISSENSCHAFTEN DER CHRISTIAN-ALBRECHTS-UNIVERSITÄT ZU KIEL  
JAHRESBERICHT / ANNUAL REPORT 1993. 1994. 69 pp.  
In German and English
- 26 JÖRG BIALAS  
SEISMISCHE MESSUNGEN UND WEITERE GEOPHYSIKALISCHE UNTERSUCHUNGEN AM SÜD-SHETLAND TRENCH  
UND IN DER BRANSFIELD STRASSE - ANTARKTISCHE HALBINSEL. 1994. 113 pp.  
In German with English summary
- 27 JANET MARGARET SUMNER  
THE TRANSPORT AND DEPOSITIONAL MECHANISM OF HIGH GRADE MIXED-MAGMA IGNIMBRITE TL, GRAN CANARIA:  
THE MORPHOLOGY OF A LAVA-LIKE FLOW. 1994. 224 pp.  
In English with German summary
- 28 GEOMAR LITHOTHEK. Edited by JÜRGEN MIENERT. 1994. 12 pp + app.  
In English
- 29 FS SONNE - FAHRTBERICHT SO 97 KODIAK-VENT: KODIAK - DUTCH HARBOR - TOKYO - SINGAPUR, 27.7. - 19.9.1994  
Hrsg. von ERWIN SUESS. 1994.  
Some chapters in German, some in English
- 30 CRUISE REPORTS:  
RV LIVONIA CRUISE 92, KIEL-KIEL, 21.8.-17.9.1992: GLORIA STUDIES OF THE EAST GREENLAND CONTINENTAL MARGIN BETWEEN 70° AND 80°N  
RV POSEIDON PO200/10, LISBON-BREST-BREMERHAVEN, 7.-23.8.1993: EUROPEAN NORTH ATLANTIC MARGIN: SEDIMENT PATHWAYS,  
PROCESSES AND FLUXES  
RV AKADEMIK ALEKSANDR KARPINSKIY, KIEL-TROMSØ, 5.-25.7.1994: GAS HYDRATES ON THE NORTHERN EUROPEAN CONTINENTAL MARGIN  
Edited by JÜRGEN MIENERT. 1994.  
In English; report of RV AKADEMIK ALEKSANDR KARPINSKIY cruise in English and Russian
- 31 MARTIN WEINELT  
BECKENENTWICKLUNG DES NÖRDLICHEN WIKING-GRABENS IM KÄNOZOIKUM - VERSENKUNGSGESCHICHTE, SEQUENZSTRATIGRAPHIE,  
SEDIMENTZUSAMMENSETZUNG. 1994. 85 pp.  
In German with English summary
- 32 GEORG A. HEISS  
CORAL REEFS IN THE RED SEA: GROWTH, PRODUCTION AND STABLE ISOTOPES. 1994. 141 pp.  
In English with German summary
- 33 JENS A. HÖLEMANN  
AKKUMULATION VON AUTOCHTHONEM UND ALLOCHTHONEM ORGANISCHEM MATERIAL IN DEN KÄNOZOISCHEN SEDIMENTEN  
DER NORWEGISCHEN SEE (ODP LEG 104). 1994. 78 pp.  
In German with English summary
- 34 CHRISTIAN HASS  
SEDIMENTOLOGISCHE UND MIKROPALÄONTOLOGISCHE UNTERSUCHUNGEN ZUR ENTWICKLUNG DES SKAGERRAKS (NE NORDSEE)  
IM SPÄTHOLOZÄN. 1994.  
In German with English summary
- 35 BRITTA JÜNGER  
TIEFENWASSERERNEUERUNG IN DER GRÖNLANDSEE WÄHREND DER LETZTEN 340.000 JAHRE.  
DEEP WATER RENEWAL IN THE GREENLAND SEA DURING THE PAST 340,000 YEARS. 1994. 6 + 109 pp.  
In German with English summary
- 36 JÖRG KUNERT  
UNTERSUCHUNGEN ZU MASSEN- UND FLUIDTRANSPORT ANHAND DER BEARBEITUNG REFLEXIONSSEISMISCHER DATEN AUS DER  
KODIAK-SUBDUKTIONSZONE, ALASKA. 1995. 129 pp.  
In German with English summary
- 37 CHARLOTTE M. KRAWCZYK  
DETACHMENT TECTONICS DURING CONTINENTAL RIFTING OFF THE WEST IBERIA MARGIN: SEISMIC REFLECTION AND  
DRILLING CONSTRAINTS. 1995. 133 pp.  
In English with German summary
- 38 CHRISTINE CAROLINE NÜRNBERG  
BARIUMFLUSS UND SEDIMENTATION IM SÜDLICHEN SÜDATLANTIK - HINWEISE AUF PRODUKTIVITÄTSÄNDERUNGEN IM QUARTÄR. 1995. 6 + 108 pp.  
In German with English summary
- 39 JÜRGEN FRÜHN  
TEKTONIK UND ENTWÄSSERUNG DES AKTIVEN KONTINENTALRANDES SÜDÖSTLICH DER KENAI-HALBINSEL, ALASKA. 1995. 93 pp.  
In German with English summary

- 40 GEOMAR FORSCHUNGSZENTRUM FÜR MARINE GEOWISSENSCHAFTEN DER CHRISTIAN-ALBRECHTS-UNIVERSITÄT ZU KIEL  
JAHRESBERICHT / ANNUAL REPORT 1994. 1995.  
In German and English
- 41 FS SONNE - FAHRTBERICHT / CRUISE REPORT SO 103 CONDOR 1 B: VALPARAISO-VALPARAISO, 2.-21.7.1995.  
Hrsg. von ERNST R. FLUEH. 1995. 140 pp.  
Some chapters in German, some in English
- 42 R/V PROFESSOR BOGOROV CRUISE 37: CRUISE REPORT "POSETIV": Vladivostok - Vladivostok, September 23 - October 22, 1994.  
Edited by CHRISTOPH GAEDICKE, BORIS BARANOV and EVGENIY LELIKOV. 1995. 48 + 33 pp.  
In English
- 43 CHRISTOPH GAEDICKE  
DEFORMATION VON SEDIMENTEN IM NANKAI-AKKRETIONSKEIL, JAPAN. BILANZIERUNG TEKTONISCHER VORGÄNGE ANHAND VON SEISMISCHEN  
PROFILIEN UND ERGEBNISSEN DER ODP-BOHRUNG 808. II + 89 pp.  
In German with English summary
- 44 MARTIN ANTONOW  
SEDIMENTATIONSMUSTER UM DEN VESTERIS SEAMOUNT (ZENTRALE GRÖNLANDSEE) IN DEN LETZTEN 250.000 JAHREN. 1995.  
In German with English summary
- 45 INTERNATIONAL CONGRESS: CORING FOR GLOBAL CHANGE - ICGC '95. KIEL, 28 - 30 June, 1995.  
Edited by JÜRGEN MIENERT and GEROLD WEFER. 1996.  
In English
- 46 JENS GRÜTZNER  
ZUR PHYSIKALISCHEN ENTWICKLUNG VON DIAGENETISCHEN HORIZONTEN IN DEN SEDIMENTBECKEN DES ATLANTIKS. 1995. 96 pp.  
In German with English summary
- 47 INGO A. PECHER  
SEISMIC STUDIES OF BOTTOM SIMULATING REFLECTORS AT THE CONVERGENT MARGINS OFFSHORE PERU AND COSTA RICA. 1996. 159 pp.  
In English with German summary
- 48 XIN SU  
DEVELOPMENT OF LATE TERTIARY AND QUATERNARY COCCOLITH ASSEMBLAGES IN THE NORTHEAST ATLANTIC. 1996. 120 pp. + 7 pl.  
In English with German summary
- 49 FS SONNE - FAHRTBERICHT / CRUISE REPORT SO 108 ORWELL: SAN FRANCISCO - ASTORIA, 14.4. - 23.5.1996  
Edited by ERNST R. FLUEH and MICHAEL A. FISHER. 1996.
- 50 GEOMAR FORSCHUNGSZENTRUM FÜR MARINE GEOWISSENSCHAFTEN DER CHRISTIAN-ALBRECHTS-UNIVERSITÄT ZU KIEL  
JAHRESBERICHT / ANNUAL REPORT 1995. 1996. 93 pp.  
In German and English
- 51 THOMAS FUNCK  
STRUCTURE OF THE VOLCANIC APRON NORTH OF GRAN CANARIA DEDUCED FROM REFLECTION SEISMIC, BATHYMETRIC  
AND BOREHOLE DATA. 1996. VI, 144 pp.  
In English with German summary
- 52 PETER BRUNS  
GEOCHEMISCHE UND SEDIMENTOLOGISCHE UNTERSUCHUNGEN ÜBER DAS SEDIMENTATIONSVERHALTEN IM BEREICH  
BIOSTRATIGRAPHISCHER DISKONTINUITÄTEN IM NEOGEN DES NORDATLANTIK, ODP LEG 104, SITES 642B UND 643A. 1993. V, 73 pp.  
In German with English summary
- 53 CHRISTIANE C. WAGNER  
COLD SEEPS AN KONVERGENTEN PLATTENRÄNDERN VOR OREGON UND PERU: BIOGEOCHEMISCHE BESTANDSAUFNAHME. 1996. 108, XXXVI pp.  
In German with English summary
- 54 FRAUKE KLINGELHÖFER  
MODEL CALCULATIONS ON THE SPREADING OF SUBMARINE LAVA FLOWS. 1996. 98 pp.  
In English with German summary
- 55 HANS-JÜRGEN HOFFMANN  
OBJEKTORIENTIERTE ANALYSE UND MIGRATION DIFFRAKTIERTER WELLENFELDER UNTER VERWENDUNG DER STRAHLENMETHODE UND  
DER EDGE-WAVE-THEORIE. 1996. XXI, 153 pp.  
In German with English summary
- 56 DIRK KLÄSCHEN  
STRAHLENSEISMISCHE MODELLIERUNG UNTER BERÜCKSICHTIGUNG VON MEHRFACHDIFFRAKTIONEN MIT HILFE DER EDGE-WAVES:  
THEORIE UND ANWENDUNGSBEISPIELE. 1996. X, 159 pp.  
In German with English summary
- 57 NICOLE BIEBOW  
DINOFLLAGELLATENZYSTEN ALS INDIKATOREN DER SPÄT- UND POSTGLAZIALEN ENTWICKLUNG DES AUFTRIEBSGESCHEHENS VOR PERU.  
1996. IV, 100, 17, 14 (7 pl.) pp.  
In German with English summary